PHOTOCATALYTIC ACTIVITIES of ZnO-BASED MATERIALS: EFFECT OF RARE-EARTH METAL ION LOADING

by

Şerife AKALIN

B.S., Chemistry, Boğaziçi University, 2007

Submitted to the Institute for Graduate Studies in
Science and Engineering in partial fulfillment of
the requirements for the degree of
Master of Science

Graduate Program in Chemistry
Boğaziçi University
2009

PHOTOCATALYTIC ACTIVITIES of ZnO-BASED MATERIALS: EFFECT OF RARE-EARTH METAL ION LOADING

APPROVED BY :

Assist. Prof. A. Neren Ökte
(Thesis Supervisor)

Assoc. Prof. Neylan Dirilgen

Assist. Prof. Aslıhan Kerç

DATE OF APPROVAL: 08.06.2009

To my beloved

FAMILY

ACKNOWLEDGEMENTS

I owe my deepest gratitude to my supervisor Assist. Prof. A. Neren ÖKTE whose encouragement and guidance from the initial to the final level enabled me to develop an understanding of the subject.

I would like to thank Assoc. Prof. Neylan DİRİLGEN and Assist. Prof. Aslıhan KERÇ for being my committee members and spending their valuable time.

I would express my special thanks to Özge Yılmaz, Alper Kimsesiz, Burcu Ünal and Sok Udom Deth that they have made available their support in a number of ways. I wish to thank to many of my colleagues; Tuba Şahin, Jesmi Çavuşoğlu, Cem Öztürk, Burcu Çakır, İlke Uğur, Sezgin Bayrak, Melis Çağdaş for their support and friendship. I also thank to Oruç Köklükaya, Çağıl Batu, Banu Yazman and Alper Kimsesiz who helped me during this project. I would like to extend my thanks to all members of Chemistry Department and the secretary of the department, Hülya Metiner, for their help and kindness.

I also wish to thank Dr. Bilge Gedik Uluocak for SEM analysis, Aslı Çakır for XRD analysis and Dr. Sinan Şen for AFM analysis.

This thesis would not have been possible unless the support of my family. I dedicate this thesis in honor of my family; my father (Yakup Akalın) and my mother (Semiha Akalın) and my sister (Ebru Akalın). And thank God for care in fulfilling my goal.

This project has been supported by Bogazici University Research Fund (BAP 08B504) this financial help is highly appreciated.

ABSTRACT

PHOTOCATALYTIC ACTIVITIES of ZnO-BASED MATERIALS: EFFECT OF RARE-EARTH METAL ION LOADING

In this study, pure and rare earth metal loaded ZnO photocatalytic materials have been prepared by coprecipitation method using the precursors of zinc and metal ions. These materials have been characterized by using scanning electron microscopy in combination with energy dispersive X-ray (SEM-EDAX) spectroscopy, X-ray diffractometer (XRD), surface area analyzer (BET) and atomic force microscopy (AFM).

Photocatalytic activities of the synthesized catalysts has been evaluated for the decolorization of methyl orange (MO) dye under UV light. The effects of some parameters such as catalyst loading, initial MO concentration, pH value, and the amount of metal loading on the decolorization efficiency were discussed. The highest performances were obtained with the lowest metal content catalyst at pH 8. MO photodecolorization obeyed pseudo first order kinetics. Also, Langmuir-Hinshelwood model was applied. A mechanism was postulated for the decolorization process of MO.

ÖZET

ZnO BAZLI MATERYALLERİN FOTOKATALİTİK ÖZELLİKLERİ: NADİR TOPRAK METAL İYONLARI KATILIMININ ETKİLERİ

Bu çalışmada, çinko ve metal iyonlarının prekürsörleri kullanılarak çöktürme yöntemiyle saf ve metal eklenmiş ZnO fotokatalitik materyalleri hazırlanmıştır. Bu materyallerin karakterizasyonu taramalı elektron mikroskobu beraberinde enerji dağılım X-ışını spektroskopisi (SEM-EDAX), X-ışını kırınım ölçer (XRD), yüzey alanı analizi (BET) ve atomik güç mikroskobu (AFM) ile yapılmıştır.

Hazırlanan materyallerin fotokatalitik aktiviteleri UV ışığı altında metil oranj (MO) boyar maddesinin bozunması ile değerlendirilmiştir. Katalizör miktarı, başlangıç MO konsantrasyonu, pH değeri ve katalizöre eklenen metal miktarı gibi farklı parametreler tartışılmıştır. En yüksek performanslar pH 8'de metal içeriği en az olan katalistlerin varlığında elde edilmiştir. Metil oranj bozunması sözde birinci mertebe kinetiğine uymaktadır. Ayrıca, Langmuir-Hinshelwood modeli uygulanmıştır. Metil oranj bozunması için bir mekanizma varsayılmıştır.

TABLE OF CONTENTS

LIST OF FIGURES

LIST OF TABLES

LIST OF SYMBOLS / ABBREVIATIONS

D	Crystal Size
e^-	Electron
E_{bg}	Band Gap Energy
h^+	Hole
k_{app}	Appearent Rate Constant
k	Reaction Constant
K	Adsorption Constant
K_i	Intermediate Adsorption Constant
l	Path length of the Spectrophotometer

λ	Wavelength of X-ray radiation
θ	Angle between X-ray radiation

AFM	Atomic Force Microscopy
BET	Surface Area
CB	Conduction Band
DRS	Diffuse Reflectance Spectroscopy
EDAX	Energy Dispersive X-Ray
FESEM	Field Emission Scanning Electron Microscopy
FWHM	Full Width Half Maximum
FTIR	Infrared Spectroscopy
MO	Methyl Orange
XRD	X–Ray Diffraction
SEM	Scanning Electron Microscopy
TiO_2	Titaniumdioxide
UV-Vis	Ultra Violet-Visible
VB	Valence Band
Zpc	Zero-point charge
ZnO	Zinc oxide

1. INTRODUCTION

Treatment of industrial waste water has become one of the most important issues of the environmental protection. Especially, textile industry where large quantities of dyes are used in, create pollution problems via releasing potential carcinogenic and toxic compounds.

Azo dyes constitute the largest and most varied class of synthetic organic dyes which enter environment during the production and manufacturing process. Biological treatment methods for industrial waste water are ineffective due to the stability of the dyes. Moreover, azo dyes are readily reduced under anaerobic conditions to potentially hazardous aromatic amines.

Since the increased public concern with these pollutants, international environmental standards are becoming more stringent. Therefore, new treatment methods are required for the removal of persistent dye organic chemicals or converting them into harmless compounds in water [1]. One of the most effective new technologies being developed to protect environment is advanced oxidation processes (AOPs). AOPs generate highly reactive species such as hydroxyl radicals ($^{\bullet}OH$) which completely destroy the pollutants in wastewater quickly and non-selectively. Various processes differ to generate the hydroxyl radicals in the presence of chemicals or catalysts. Some use ultraviolet (UV) light energy as part of the process, such as UV/H_2O_2, some others use ozone (O_3), usually in combination with hydrogen peroxide (H_2O_2). The type or the extent of AOP treatment will determine the degree to which a contaminant will be mineralized. Among the AOPs, semiconductor mediated photocatalysis is more widely used, owing to the special properties of the semiconductors. These materials, in general, are known as non-toxic, easily available and cheap. Although TiO_2 is universally recognized as the most photoactive catalyst, many reports have highlighted the effectiveness of ZnO in removing organic compounds in water matrices [2].

In this study, our purpose is to use ZnO as an alternative catalyst to TiO_2 and enhance its the photocatalytic activity by loading with rare-earth metal ions. These ions are selected from the lanthanide (Ln) series as La^{3+}, Pr^{3+}, Nd^{3+}, Eu^{3+}, Gd^{3+}, Dy^{3+} and Ho^{3+}, known to resemble each other, have empty f-orbitals and also, have the ability to form complexes with various Lewis bases (e.g. amines, aldehydes etc.). Accordingly, such a new catalyst system may favour separating charge carriers efficiently, prolonging the life of carriers, inhibiting the recombination of electron-hole pairs and eventually causing improvement of the catalytic performance.

The first stage of our study includes characterization of the synthesized pure ZnO and metal-loaded ZnO photocatalysts by using X-ray diffraction technique (XRD), scanning electron microscopy with energy dispersive X-ray (SEM-EDAX), diffuse reflectance spectroscopy (DRS), atomic force microscopy (AFM) and surface area (BET) measurements. At the second stage of our study, efficiencies of all synthesized catalysts are collated for the decolorization process of an azo dye; methyl orange molecule (MO) under UV illumination. Effects of some parameters such as concentration of MO, content of metal ion, pH, amount of catalyst are evaluated in detail. A mechanism is postulated for the MO degradation process.

2. THEORY

2.1. Zinc Oxide

Zinc oxide (ZnO) is an oxidic compound naturally occurring as the rare mineral zincite, which crystallizes in the hexagonal wurtzite structure. The mineral zincite was discovered in 1810 by Dr. Archibald Bruce in Franklin [3].

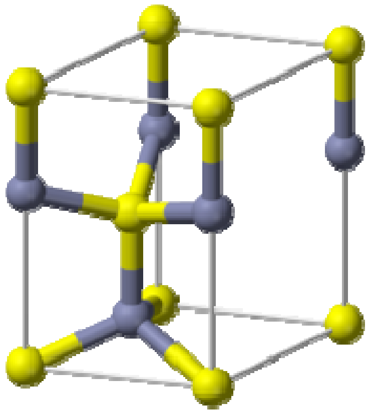

Figure 2.1. Structure of Wurtzite

For industrial use, ZnO is produced at levels of 10^5 tons per year by three main processes known as: French process, direct method and the American process [4]. Metallic zinc is melted in a graphite crucible and vaporized above 907°C. Zinc vapor instantaneously reacts with the oxygen in the air to give ZnO, accompanied by a drop in its temperature and bright luminescence. Zinc oxide particles are transported into a cooling duct and collected in a bag house. This indirect method is commonly known as the French process (FP) which was popularized by LeClaire (France) in 1844 [5]. Direct method is related to the French process, zinc ores or roasted sulfide concentrates are mixed with coal. In a reduction furnace, ore is reduced to metallic zinc and the vaporized zinc is allowed to react with oxygen to form zinc oxide. In American process, ore of zinc (zinc ash) is dissolved (as $ZnCl_2$) and precipitated with alkali. Zinc oxide made from this process is known as "Active Zinc Oxide" [6].

Some of the applications of zinc oxide are in the following industries: The rubber industry has utilized an increasing number of the many optical, physical and chemical properties of zinc oxide. Also, zinc oxide is mainly used in food powders, pharmaceuticals, cosmetics (in zinc soap, ointment, dental inlays, powders and in creams it protects the skin by absorbing the ultraviolet sunburn rays).

2.1.1. Zinc Oxide as a Semiconductor

Zinc oxide has been investigated already in 1912. With the beginning of the semiconductor age after the invention of the transistor [7], systematic investigations of ZnO as a compound semiconductor were performed. In 1960, the good piezoelectric properties of zinc oxide were discovered [8], which led to the first electronic application of zinc oxide as a thin layer for surface acoustic wave devices [9]

A semiconductor is a material which has a band structure, characterized as a series of energetically closed spaced energy levels (valence band) and a second series of energetically similar levels lying at a higher energy (conduction band). Its band gap energy (E_{bg}) for electronic excitation lies between zero and about 3 electron volts [10].

When a semiconductor is illuminated by light of suitable energy, namely higher than its band-gap energy, electrons are promoted from valence band to the conduction band and positive holes are created in the valence band. The occurrence of the above charge separation is one of the first essential steps of a photocatalytic reaction. Electrons formed in the conduction band and the holes formed in the valence band in this way work as powerful reductants and oxidants, respectively [11].

A semiconductor photocatalyst should be chemically and biologically inert, stable, easy to produce and to use, efficiently activated by sunlight, cheap, and without risks for the environment or humans [12].

Generally, photocatalytic reactions are promoted under UV illumination because most of semiconductor photocatalysts have band gap in the UV region. Among the photoactive oxides, titanium dioxide (TiO_2) is by far the most popular, which transforms organic pollutants to mineralization by an efficient electron transfer process [13,14]. Till now anatase form of TiO_2 has been extensively investigated in the field of photocatalysis owing to its complementary physiochemical properties [15]. In order to shift the optical absorption of TiO_2 to the visible region of solar spectrum and circumvent charge recombination on photocatalyst surface, various attempts have been made, such as coupling of TiO_2 with gold and SnO_2 with silver [16]. However, this scheme was unsuccessful to increase photocatalytic activities in the visible region. In a recent study by Klosek and Raftery [17] vanadium-doped TiO_2 has been employed for photo-oxidation of ethanol which showed higher photoactivity but obtained carbon monoxide and formic acid as by products that were also hazardous. Also, use of the expensive photoactive anatase form of TiO_2 catalyst is uneconomic for large scale water treatment operations [18].

Hence, ZnO has been investigated as an alternative photocatalysts to TiO_2. ZnO has emerged to be more efficient catalyst as far as water detoxification is concerned [19,20]. Also, it has more numbers of active sites with high surface reactivity and high band energy (3.37 eV) in comparison to TiO_2 (3.2 eV) [21]. The following figure simply presents the photacatalytic degradation mechanism in the presence of ZnO.

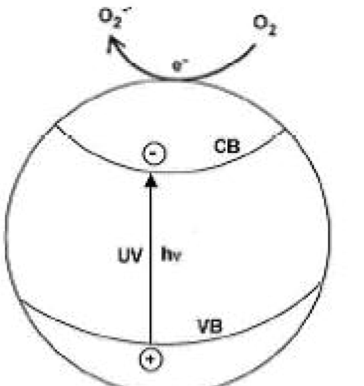

Figure 2.2. ZnO-mediated photacatalytic degradation mechanism

Irradiation of an aqueous ZnO dispersion leads to excitation of an electron from the valence band (VB) to the conduction band (CB), creating an electron-hole pair (Equation

2.1). The heterogeneous photocatalytic process takes place through a complex sequence of reactions (Equation 2.2-2.9).

$$\mathrm{ZnO} + h\nu\ (\mathrm{UV}) \rightarrow \mathrm{ZnO}\ (e^{-}{}_{\mathrm{CB}} + h^{+}{}_{\mathrm{VB}}) \qquad (2.1)$$

The formation of redox pair could either be followed by respective reaction resulting in the dissipation of the reactive species:

$$\mathrm{ZnO}\ (h^{+}{}_{\mathrm{VB}}) + \mathrm{HO}_{2\ \mathrm{ads}} \rightarrow \mathrm{ZnO} + \mathrm{HO}^{\bullet}{}_{\mathrm{ads}} + \mathrm{H}^{+} \qquad (2.2)$$

$$\mathrm{ZnO}\ (h^{+}{}_{\mathrm{VB}}) + \mathrm{HO}^{-}{}_{\mathrm{ads}} \rightarrow \mathrm{ZnO} + \mathrm{HO}^{\bullet}{}_{\mathrm{ads}} \qquad (2.3)$$

$$\mathrm{ZnO}\ (e^{-}{}_{\mathrm{CB}}) + \mathrm{O}_{2\ \mathrm{ads}} \rightarrow \mathrm{ZnO} + {}^{\bullet}\mathrm{O}^{-}{}_{2} \qquad (2.4)$$

$${}^{\bullet}\mathrm{O}^{-}{}_{2} + \mathrm{H}^{+} \rightarrow \mathrm{HO}_{2}^{\cdot} \qquad (2.5)$$

$$2\mathrm{HO}_{2}^{\cdot} \rightarrow \mathrm{H}_{2}\mathrm{O}_{2} + \mathrm{O}_{2} \qquad (2.6)$$

$$\mathrm{H}_{2}\mathrm{O}_{2} + e^{-} \rightarrow \mathrm{OH}^{-} + {}^{\cdot}\mathrm{OH} \qquad (2.7)$$

$$\mathrm{HO}^{\cdot\bullet}{}_{\mathrm{ads}} + \mathrm{D}_{\mathrm{ads}} \rightarrow \mathrm{D}_{\mathrm{ox}} \qquad (2.8)$$

$$\mathrm{HO}_{2}^{\cdot} + \mathrm{D}_{\mathrm{ads}} \rightarrow \mathrm{D}_{\mathrm{ox}} \qquad (2.9)$$

where D represents a dye molecule. Thus, $\mathrm{HO}^{\cdot}$ and $\mathrm{HO}_2^{\cdot}$ produced in the above reaction series are responsible from the oxidation of organic compounds (Equation 2.8 and 2.9).

2.1.2. Factors Affecting Surface and Morphological Aspects in ZnO Photocatalysis

2.1.2.1. Surface Area of ZnO. In photocatalysis, large surface area can be the determining factor of adsorbed organic molecules which promotes the reaction rate. However, powders with a large surface area are usually associated with large amounts of crystalline defects, which favour the recombination of electrons and holes leading to a poor photoactivity [22].

BET theory is a rule for the physical adsorption of gas molecules on a solid surface and serves as the basis for an important analysis technique for the measurement of the specific surface area of a material. BET stands for Brunauer, Emmett, and Teller, the three scientists who optimized the theory [23]. The concept of the theory is an extension of the

Langmuir theory, which is a theory for monolayer molecular adsorption, to multilayer adsorption with the following hypotheses:

- Gas molecules physically adsorb on a solid in layers infinitely
- There is no interaction between each adsorption layer; and
- The Langmuir theory can be applied to each layer [24].

BET isotherms rise indefinitely as the pressure is increased because there is no limit to the amount of material that may condense when multilayer coverage may occur. A BET isotherm is not accurate at all pressure values, but used in industry to determine the surface areas of solids [25].

2.1.2.2. Particle Size of ZnO. The size of photocatalysts is one of the most important factors that effect the photodegradation efficiency. It is well known that in the nanometer-size range, physical and chemical properties of semiconductors are modified (compared with bulk). Small variations in particle diameters lead to great modifications in the surface/bulk ratio, thus modifying the significance of volume and surface electron–hole recombination. When the size of the photocatalyst particles decreases, photon absorbance increases due to the increase in the amount of the dispersion particles per volume in the solution. Also, the surface area of the photocatalyst increases which promotes the adsorption of more dye molecules on the surface. Additionally, electron–hole recombination will be suppressed.

The average particle sizes are determined by applying the Scherrer's equation (Equation 2.10) to the (101) diffraction of ZnO.

$$D = \frac{A\lambda}{FWHM.Cos\theta} \tag{2.10}$$

where D is the average crystal size, A is 0.94 which is Scherrer's Constant, λ is the wavelength which equals to 0.54 nm, FWHM is full width half maximum value of the corresponding diffraction peak and θ is the position of the selected diffraction peak.

2.1.2.3. Zeta Potential of the Catalysts. Most particles in an aqueous colloidal dispersion carry an electric charge due to either ionization of surface groups or adsorption of charged species. The zeta potential of a photocatalyst is the overall charge that acquires in an aqueous medium. The adsorption of a pollutant molecule is required for efficient photodegradation in heterogeneous photocatalysis. Consequently the surface properties of the catalysts can be changed to bring about different photoactivity. A change in pH can lead to a change of the degradation rate. Zeta-potential of the catalysts changes with changing pH of solution. The zero point of charge is defined as the pH at which the surface charge is zero. The zero-point charge (zpc) for ZnO is 9.0. Fouad et al [26] reported that based on the zpc value, ZnO surface is positively charged below pH 9.0. At low pH value, electrostatic interactions between the positive photocatalyst surface and dye anions (which generated from the dissociation of sodium salt of the dye molecule, [dye–Na] → $[\text{dye}^{-}] + \text{Na}^{+}$) in aqueous solution may be lead to strong adsorption of the dye on the catalyst surface.

2.1.2.4. Sol-gel Method: Preparation of Nano-sized ZnO Particles. The method is based on the phase transformation of a sol obtained from metallic alkoxides or organometallic precursors. The sol–gel method has many advantages over other fabrication techniques such as purity, homogeneity, felicity, and flexibility in introducing dopants in large concentrations, stochiometry control, ease of processing, control over the composition, and the ability to coat large and complex areas. The non-alkoxide route uses inorganic salts (such as nitrates, chlorides, acetates, carbonates, acetylacetonates, etc.), which requires an additional removal of the inorganic anion; while the alkoxide route (the most employed) uses metal alkoxides as starting material [22,27]. ZnO nanoparticles and metal loaded ZnO were prepared by coprecipitation method using the precursors of zinc and metals.

2.1.2.5 Contact Angle of the Photocatalysts. When a photocatalyst zinc oxide (ZnO) captures ultraviolet light (UV), it forms activated oxygen from water or oxygen in the air. The activated oxygen is strong enough to decompose organic materials. Hydrophilicity of a photocatalyst can be represented with a contact angle of water with the photocatalyst. The contact angles of water with inorganic materials such as glass and hydrophobic resins such as silicone resin are 20-30 and 70-90 degrees, respectively.

Langmuir-Hinshelwood model can be applied to photocatalytic reactions. According to the model, the surface coverage (θ) of catalysts was given by the following equation (2.11):

$$\mathrm{\theta} = \frac{\mathrm{KC_t}}{1 + \mathrm{KC_t} + \sum_{\mathrm{i}} \mathrm{K_i C_i}} \tag{2.11}$$

where *i* refered to the each of various intermediates during degradation process, C_t was the remaining concentration of the probe molecule in solution by time, *t* was the time of reaction, *k* was the reaction constant, *K* and K_i were adsorption constants of probe molecules and intermediates, respectively. If it is assumed that the adsorption constants for all organic intermediate molecules present in the reacting mixture are equal, the following assumption can be made and given in equation (2.12):

$$KC_t + \sum_i K_i C_i = K\,C_t \tag{2.12}$$

Thus, rate expression becomes

$$\text{Rate= } k_r\theta = \frac{k_r K C_t}{1 + KC_t} = k_{app} C_t \tag{2.13}$$

From equation 2.13, the rate (R) can be written as

$$\frac{1}{Rate} = \frac{1 + \mathrm{KC_t}}{\mathrm{k_r KC_t}} \tag{2.14}$$

This equation can be rearranged as

$$\frac{1}{\mathrm{k_{app} C_t}} = \frac{\mathrm{KC_t}}{\mathrm{KC_t k_r}} + \frac{1}{\mathrm{k_r C_t K}} \tag{2.15}$$

And finally, equation 2.16 is obtained by substitution of C_o in place of C_t as the equilibrium concentration of the probe molecule after dark adsorption.

$$\frac{1}{Rate}=\frac{1}{k_{app}C_0}=\frac{1}{\mathrm{k_r K C_0}}+\frac{1}{\mathrm{k_r}} \tag{2.16}$$

2.1.3. Metal Ion Loading

The presence of metal ions lead to the formation of a permanent space charge region whose electric force improves the charge separation between photogenerated electrons and holes. Distribution of the loaded metal ion should be considered carefully, i.e. the lattice and the surface of photocatalyst. This depends on the amount of the metal ion and on the calcination temperature because some amorphous or microcrystalline species may segregate on the particle surface if the solubility limit of the used metal ion in photocatalyst is exceeded and the diffusion phenomena are related to the temperature. The degree of the dispersion of the metal on the particle surface and the homogeneity of the chemical composition of a single particle depends on the preparation methods and on the calcination temperature [28].

p-type doping, is obtained by dissolving heterocations of valencies lower than the semiconductor, creates deficiencies of valence electrons, called "holes". So, p-type dopants act as acceptor centers by trapping photoelectrons. After they are negatively charged, attract holes and lead to forming of recombination centers. On the other hand, in n-type materials there are electron energy levels near the top of the band gap so that they act as donor centers.

However, there are some metallic dopants such as Fe^{3+}, Ru^{3+}, Os^{3+}, and Gd^{3+} which have half-filled electronic configuration (d^5 and f^7) that is known to be more stable. When these ions trap electrons, the half-filled electronic configuration is destroyed and their stability decreases. The trapped electrons can easily be transferred to oxygen adsorbed on the surface of the catalyst and the ions return to the original stable half-filled electron structure. This promotes charge transfer and efficient separation of the electrons and holes by shallow trapped electrons.

Rare earth metal compounds especially their oxides have become of increasing interest in recent years because of their special photoluminescence and catalytic properties. It is expected that loading of rare earth metal ions into a ZnO matrix could provide a higher photocatalytic performance in the degradation of organic pollutants.

An optimum value of metal loading is necessary for enhancing the photocatalytic activity because as the content of doping ions increases, the surface barrier becomes higher, and the space charge region becomes narrower. So photoinduced electron-hole pairs are efficiently separated. On the other hand, the excess ion doping inhibit the direct exposure of UV light on the surface of the catalyst which decrease the excitation of electron from valence band to conduction band that promotes the recombination of photogenerated electron-hole pairs. Anandan et al [29], have confirmed that rate of degradation of monocrotophos over La-doped ZnO increases with increasing La loading up to 0.8 wt per cent and then decreases due to the coverage of the surface of ZnO inhibits the photoexcitation of the semiconductor and also lower metal amounts are not generally more beneficial as well.

2.2. Application of ZnO-Based Materials

In 2002, photocatalytic discolorization of Reactive blue 19 (RB-19) was investigated by Mansilla et al [30], in the presence of TiO_2 and ZnO catalysts. Effect of pH, amount of catalyst and dye concentration were examined. ZnO showed greater degradation activity than TiO_2 and its use is limited only by pH. Results showed that, although toxicity increases during the first stages of the reaction, it was completely removed on achievement of thorough discoloration.

Pal et al [1] investigated the porous ZnO thin films that were prepared on glass substrates by a sol-gel process using Zn-acetate after calcination at 400°C. Surface morphologies were studied by XRD and SEM analyses. Films were used to decompose phenol, chlorophenol and polyaromatic hydrocarbons to CO_2 quite efficiently with the limitations of its photodissolution. During the degradation of these organic compounds, formation of hydroquinone, benzoquinone and hyrdroxylated carbonyl compounds were detected as the major intermediate photoproducts. Concentrations decreased linearly with illumination time and higher rate constants were obtained which are comparable to the most widely used material TiO_2 for the for the degradation of these organics.

In 2002, Music and Dragcevic [32], studied the influence of chemical synthesis on the crystallization and properties of zinc oxide. They used two types of the chemical synthesis of ZnO: (a) the decomposing urea process and (b) crystallization from the suspensions obtained by abrupt mixing of $Zn(NO_3)_2$ and NH_4OH solutions. At the second method, a precipitation was obtained by abrupt adding of concentrated NH_4OH solution into $Zn(NO_3)_2$ solution and autoclaving of this compound yielded ZnO. It is showed that as the heating temperature increases, rate of conversion increases. On the other hand, at the ureas process specific surface areas of these ZnO samples decreases. Also zeta potentials measured for ZnO particles produced by the urea process were higher than the those measured for ZnO particles produced by autoclaving.

Davolos et al [33], have investigated the catalytic activity of europium(III)-containing zinc oxide. It is found that diffusion of europium ion into the zinc oxide lattice depends on several parameters such as preparation method, thermal treatment, doping ion content. It is found that europium(III) doping promoted the activity of ZnO catalyst.

In 2004, in the study of Daneshvar and Salari [34], photocatalytic degradation of acid red was examined in the presence of ZnO. The effects of pH, amount of photocatalyst, hydrogen peroxide and ethanol concentration were investigated. It is found that optimum amount of photocatalyst was 160 ppm, with dye concentration of 20 ppm. When the photolysis was carried out in the absence of ZnO, photodegradation efficiency was small and also negligible in the absence of UV light. The complete removal of color, after selection of optimal operational parameters, could be achieved in 1 h irradiation.

Lü et al [35], carried out a study of structure evaluation and highly enhanced luminescence of Dy^{3+} doped ZnO nanocrystals by Li^+ doping via combustion method. Characterization of samples are done using microstructural and optical measurements. Synthesized nanoparticles showed hexagonal crystalline phase with an aveage diameter of 20 nm. Moreover, it is showed that emission of doped Dy^{3+} ions into ZnO, and Li^+ doping has increased the enhancement of photoluminescence of Dy^{3+} ions.

In 2004, Yodogava and Yamamoto [36], studied grain boundary dependency of nonlinear current-voltage characteristics in Pr and Co doped ZnO bicrystals. Pr and Co doped bicrystals were synthesized to examine their current-voltage characteristics. By using high-resolution transmission microscopy and energy-dispersive x-ray spectroscopy, grain boundary structures and chemical compositions of bicrystals were investigated. It is found that all boundaries are joined except for some precipitates of Pr_6O_{11} and existence of showed that Pr is saturated at all boundaries.

Synthesized La-doped ZnO nanoparticles with different La contents and their characterization are done by XRD, UV-VIS, AFM [29]. The XRD. UV-vis results revelaed that the particle size of pure ZnO is higher than La-doped ZnO and decreases with increasing La loading. By AFM, rough and high porous surface of La-doped ZnO was observed, which is critical for enhancing the photocatalytic activiy. The photocatalytic activiy of La-doped ZnO for the degradation of MCP was studied and the results are compared with ZnO and TiO_2. It was observed that the rate of degradation of MCP over La-doped ZnO increases with increasing La doping up to 0.8 wt. per cent and then decreases. It was showed that small particle size, seperation of charge carriers (e^-/h^+), rough and high porous surface of La-doped ZnO are very important factors to increase photocatalytic activity.

Pratsinis et al [37] prepared the high surface Ag-ZnO catalyst by flame spray pyrolysis and characterizations of the catalysts are done by XRD, nitrogen adsorption, UV-vis spectroscopy and electron microscopy (SEM and transmission electron microscopy (TEM)) combined with energy dispersive X-ray spectroscopy (EDXS) for elemental mapping. Size of Ag clusters were from 5 to 25 nm which was controlled by Ag loading and did not effect the ZnO crystal size. Methylene blue solution was used as a model substance to evaluate the photodegradation performance of Ag-ZnO catalysts. Flame spray pyrolysis-made Ag-ZnO catalysts was compared to wet-made Ag-ZnO and reference titania. It is found that optimum value of Ag loading was 3 at.per cent. also, flame-made Ag-ZnO showed higher photocatalytic efficiency than wet-made and reference titania powders.

In 2005, effect of transition metal ions on photocatalytic activity of ZnO in bleaching of some dyes were investigated [38]. The effects of pH, concentration of dyes, amount of semiconductor and light intensity were also examined on the efficiency of the photodegradation. Fe^{2+}, Ni^{2+}, Ag^{+},Cu^{2+}, Co^{2+}, V^{2+} and Mn^{2+} have been studied and it is found that photocatalytic activiy of ZnO can be increased in the presence of 3d transition metals.

In 2007, in the study of Anandan, Vinu, Srinivasu and Ariga [39], La-doped ZnO particles with different La contents were prepared by co-precipitation method using the precursors of zinc and lanthanum. The XRD results indicated that the particle size of pure ZnO is higher as compared to that of La- doped ZnO and decreases with increasing La content which lead to enhancement of photocatalytic activity of La-doped ZnO samples. Moreover, the relative photonic efficiency value of La-doped ZnO is relatively higher as compared to undoped ZnO. It has been concluded that higher adsorption capacity, smaller particle size, and increase in the band gap value of ZnO upon La loading have a significant influence on the enhanced photocatalytic activity of La-doped ZnO catalysts.

Swaminathan et al [40], carried out a study of the photocatalytic degradation of an azo dye acid red 18(AR18) using ZnO as a photocatalyst in aqueous solution under UV irradiation. The effects of operational parameters such as the amount of photocatalyst, dye concentration and initial pH have been examined. It is showed that both illumination and the catalyst were necessary for the destruction of AR18 by doing blank experiments with both illuminated AR18 solution and the suspension containing ZnO.

Ge, Xie and Bai [41] investigated the structural characteristics and UV-light enhanced gas sensitivity of La-doped ZnO particles. Photocatalysts were synthesized by sol-gel method starting from zinc acetate dehydrate, lanthanum sesquioxide, alcohol and nitric acid. The crystal structures of the photocatalysts were characterized by XRD and morphology of the nanoparticles were characterized by FESEM. It is showed that prepared nanoparticles with the hexagonal wurtzite contained adsorbed water and some organic compounds below 300°C which was a key for the calcination temperature of the ZnO-based xerogel. Specific sensitivity to alcohol and benzene with (and without) UV-light excitation were tested by the pure ZnO and La-doped ZnO thick film sensors. It is found that UV-light excitation can not only enhance sensitivies by increasing electron-hole pairs and speding up the ionization of the adsorbed oxygen molecules.

In 2007, Che and Guo [42], studied oriented growth and luminescence of ZnO:Eu films prepared by sol-gel process. Prepared thin films were characterized by X-ray diffraction and photoluminecent spectra. Effect of annealing atmosphere was investigated. It is found that, the c-oriented growth of films strongly depends on the annealing atmosphere because the degree of c-oriented growth increases with the decrease of oxygen content in the annealing atmosphere.

In the study of Chen, Wang, Zhang, Wu and Yan et al [43], thin films of ZnO with different La doping concentration (0, 1, 3, 5, 10 at per cent) are fabricated by the sol-gel method using spin-coating technique and the effect of La doping concentration on the properties of ZnO films is investigated. The films are hexagonal wurtzite structures and have highly preferred growth along the c-axis direction. As La dopent content increases, the grain sizes of ZnO films decreases. In the visible region, undoped and doped ZnO films have highly transparent properties, and the optical band gap increases from 3.26 to 3.31 eV due to some incorporated La^{3+} ions in the ZnO lattice.

In the study of Ullah et al [44], undoped ZnO and Mn-doped ZnO nanocrystals using wet-chemical precipitation techniques were synthesized. Photocatalysts are characterized by transmission electron microscopy, infrared spectroscopy, photo-co-relation spectroscopy and UV-vis-spectroscopy. It is found that Mn-doped ZnO had higher optical absorption which promotes the using of photocatalysts under visible light irradiation. From the results, it is concluded that photocatalytic activities of Mn-doped ZnO are 50 times higher than the pure ZnO under visible light irradiation which suggested these nanoparticles can be used as immobilized photocatalysts for water and environmental detoxification from organic compounds, inorganic compounds like arsenic and bacteria.

In the study of Chao et al [45], annealing effects on the properties of Nd containing ZnO nanoparticles prepared by sol-gel process were investigated. Synthesized nanoparticles have a size of ~25 nm and show strong near-edge emission centered at 380 nm together with defect related deep level emission at ~620 nm. It is found that annealing caused re-crystallization and an additional luminescence band centered at 899 nm due to the inner shell transition of Nd^{3+}. After annealing at 600°C, intensity of Nd^{3+} emission at 899 nm reached a maximum. On the other hand, annealing at 1000°C caused decomposition of ZnO and formation of Nd_2O_3.

3. EXPERIMENTAL

3.1. Reagents

Zinc nitrate hexahydrate ($Zn(NO_3)_2.6H_2O$) (99.0 per cent Merck), lanthanum nitrate hexahydrate ($La(NO_3).6H_2O$) (99.0 per cent Merck), neodymium(III)-nitrate hexahydrate ($Nd(NO_3)_3.6H_2O$) (99.99 per cent Acros), praseodymium(III)-nitratepentahydrate ($Pr(NO_3)_3.5H_2O$) (99.9 per cent Acros), dysprosium chloride hexahydrate ($DyCl_3.6H_2O$) (99.9 per cent Acros), europium(III) oxide (Eu_2O_3) (99.99 per cent Acros), gadolinium(III) nitrate hexahydrate ($Gd(NO_3)_3.6H_2O$) (99.9 per cent Acros), holmium (III) nitrate pentahydrate ($Ho(NO_3)_3.5H_2O$) (99.9 per cent Acros), titanium (IV) oxide (TiO_2) (99.8 per cent Aldrich), titanium dioxide (TiO_2) (99.0 per cent Merck), nitric acid (HNO_3) (65 per cent Merck), ammonia (NH_3) (25 per cent Merck) and sodium carbonate (Na_2CO_3) (Merck) were used as provided by the suppliers without further purification. Water was purified with an Elga-Pure Water Purification (UHQ Ц) system.

3.1.1. Methyl Orange

Textile industries produce large quantities of highly coloured effluents, which are generally toxic and resistant to destruction by biological treatment methods [40]. Within the overall category of dyestuffs, the azo compound class accounts for 60-70 per cent of all dyes. They all contain one or more azo group, -N=N-, which links two sp^2 hybridised carbon atoms. Such colored dye effluents pose a major threat to the surrounding ecosystems since, apart from the environmental pollution; some of the dyes pose documented health hazards [46]. Various biological, physical and chemical processes are applied for color removal from textile effluents. Bio-treatment is ineffective for color removal due to the fact that azodyes are resistant to aerobic degradation. Moreover, the azodyes that undergo reductive cleavage by anaerobic biological treatment method, potentially generate carcinogenic aromatic amines during the process. Physical methods such as elimination by adsorption on activated carbon, coagulation, electrocoagulation, flocculation and reverse osmosis are not destructive but only transfer the contamination from one phase to another, thus causing secondary pollution. Chemical treatments such as using ozone, have yielded encouraging results of color and organics removal, but the required dosages are often too high to be economically feasible [47]. Methyl orange (MO) is a well known azodye (Figure 3.1 inset) that is highly soluble in water due to the having sulphonic groups on its structure. Furthermore, methyl orange is a pH indicator because of its clear colour change from red to orange and finally to yellow with increasing pH. Methyl orange has two absorption maxima when dissolved in water, the UV–Vis (Shimadzu UV-1600) spectrum of; first band at 274 nm and a more intense second band at 464 nm (Figure 3.1).

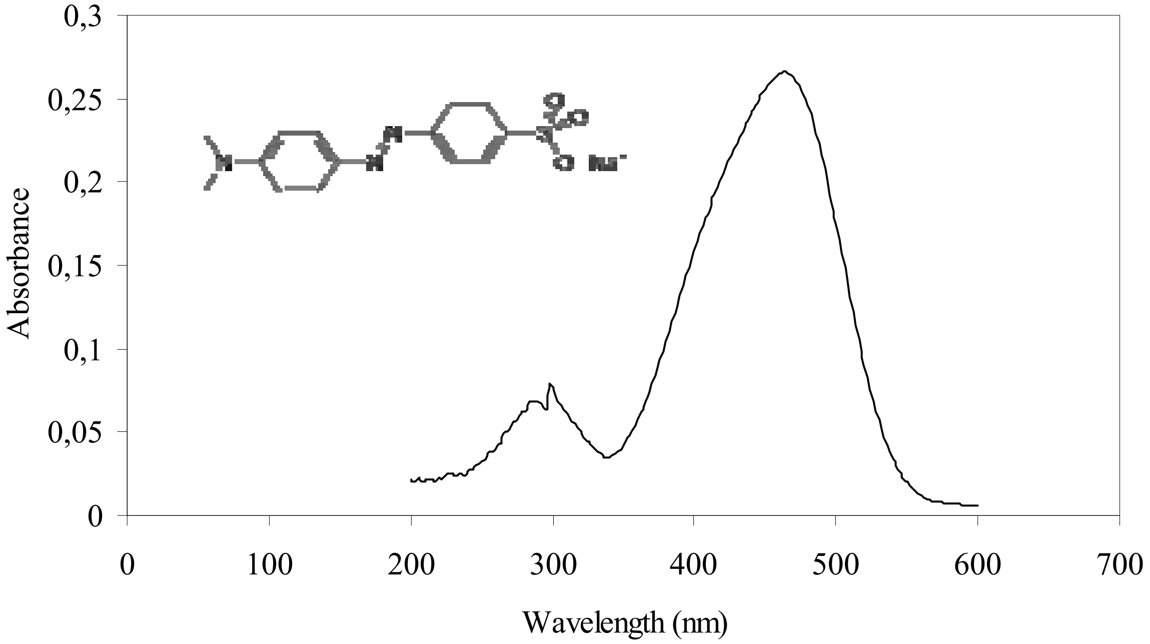

Figure 3.1. Electronic spectrum of methyl orange in aqueous solution. Inset: Chemical structure of methyl orange

3.1.2. Postulated Mechanism for MO Degradation

Oxidative degradation of azo dyes occurs generally by hydroxyl radicals, known as highly reactive electrophilic oxidants. Main reactions of hydroxyl radicals with these compounds can be addition to the chromophore, addition to the aryl rings, hydrogen abstraction or one electron oxidation [48]. Experimentally proposed degradation mechanisms focus on the cleavage of either the N-N bond resulting in nitrosoaryl intermediates or the C-N bond as shown in Figure 3.2 [49,50].

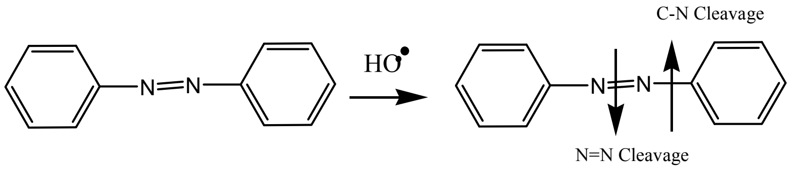

Figure 3.2. Proposed degradation mechanisms of azo dyes

So during the degradation process, the identified adducts are either aromatic amine or phenolic compounds. The following possible mechanism for the degradation of MO to form small molecules, such as CO_2, H_2O and the inorganic anions such as SO_4^{2-} and NH_4^+ is postulated and shown in Figure 4.75.

As an initial hydroxyl attack to the carbon atom bearing the azo bond, benzenesulfonic acid (I), dimethyl aniline (II) and N_2 gas may arise. The electron withdrawing sulphonate group inhibits reactivity towards •OH of the ring that carried it. Thus, the ring with the amino group is the first target for the hydroxyl radicals due to the electron withdrawing effect of sulphonate group and steric hindrance [51]. The reaction proceeds with subsequent attacks of hydroxyl radicals and formation of aniline molecule (IV). The ortho-para directing character of $^{-}NH_2$ produces 4-hydroxyaniline (V). Further hydroxyl radical attacks result in the formation of molecules VI and VII. MeO and most of the intermediates, benzene derivatives, disappeared during the discolouration stage [52]. Moreover, in the course of the degradation small molecules and inorganic anions are also progressively formed. Although bleaching reaction is very fast, complete mineralization of the dye to yield small molecules, such as CO_2, H_2O and the inorganic anions such as SO_4^{2-} and NH_4^+ takes much longer.

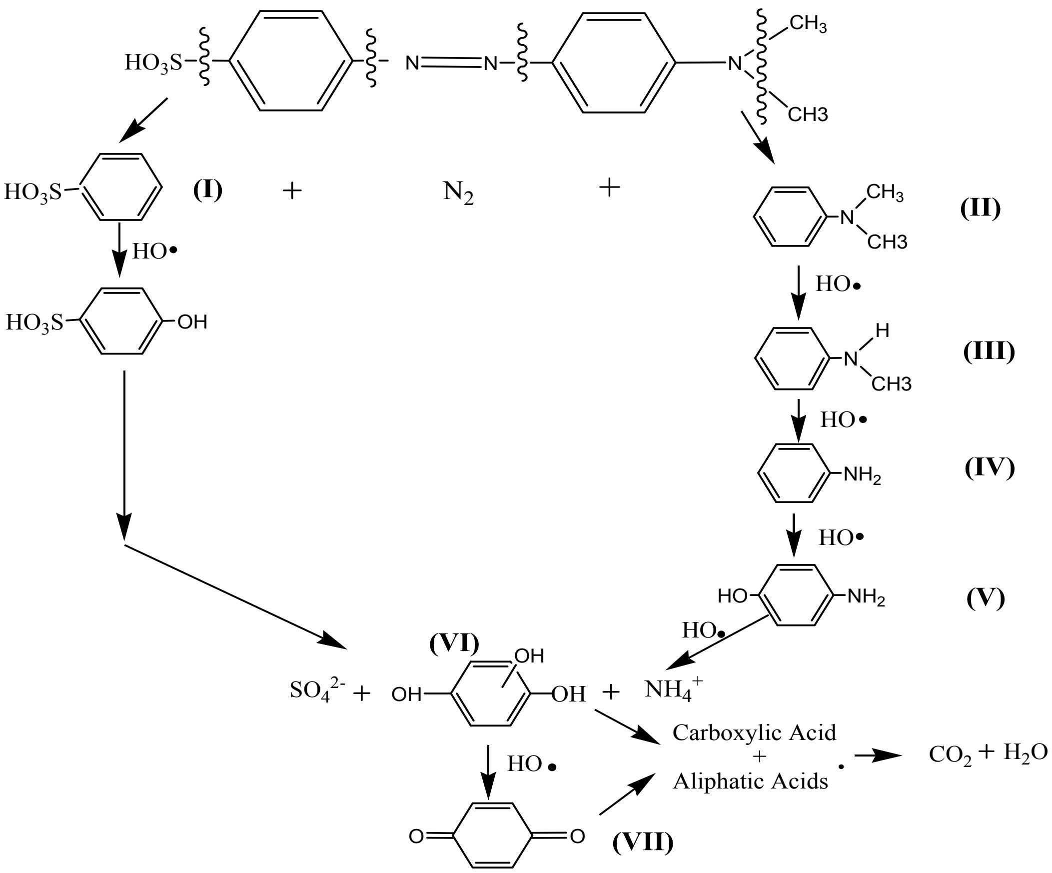

Figure 3.3. Postulated Degradation Mechanism of MO

3.2. Preparation of Catalysts

3.2.1. Sol-Gel Method: Preparation of Pure ZnO

As precursor of zinc, zinc nitrate hexahydrate ($Zn(NO_3)_2.6H_2O$) (0.5 mol/L) and sodium nitrate (Na_2CO_3) (0.5 mol/L) were dissolved separately in 100 ml of de-ionized water and 100 ml of 0.5 mol/l solutions were obtained. Then, zinc nitrate solution was slowly added into Na_2CO_3 solution which was vigorously stirred for half an hour. They mixed for an hour and then centrifuged, washed several times. The resultant white precipitate was dried at 100°C and calcinated at 400°C for 5 hours. So ZnO particles are obtained at the end.

3.2.2. Preparation of Metal Loaded ZnO

$La(NO_3).6H_2O$, $Nd(NO_3)_3.6H_2O$, $Pr(NO_3)_3.5H_2O$, $DyCl_3.6H_2O$, $Ho(NO_3)_3.5H_2O$, $Gd(NO_3)_3.6H_2O$ and Eu_2O_3 were used as metal-ion precursors. Using the precursors of zinc and metal ions, metal-loaded ZnO particles were prepared by coprecipitation method. Metal ion precursors in the required stoichiometry was dissolved in water and then slowly added into the $Zn(NO_3)_2.6H_2O$-Na_2CO_3 solution which were dissolved separately in de-ionized water and mixed for an hour.

Depending on the loading of ZnO, requisite amount of metal precursors as 1.0 per cent or 2.3 per cent or 4.5 per cent was added to the suspension. The resulting mixed suspension was centrifuged and washed several times with de-ionized water followed by drying at 100°C and subjected to calcination for 12 h at 400°C. Lastly the products were ground into fine powder and stored in dark. The catalysts were hereafter named as, 1.0 Metal-ZnO, 2.3 Metal-ZnO, 4.5 Metal-ZnO. The following is the list of all metal loaded catalysts: 1.0 La-ZnO, 2.3 La-ZnO, 4.5 La–ZnO, 1.0 Pr-ZnO, 2.3 Pr-ZnO, 4.5 Pr–ZnO, 1.0 Nd-ZnO, 2.3 Nd-ZnO, 4.5 Nd–ZnO, 1.0 Eu-ZnO, 2.3 Eu-ZnO, 4.5 Eu–ZnO, 1.0 Dy-ZnO, 2.3 Dy-ZnO, 4.5 Dy–ZnO, 1.0 Gd-ZnO, 2.3p Gd-ZnO, 4.5 Gd–ZnO, 1.0 Ho-ZnO, 2.3 Ho-ZnO, 4.5 Ho–ZnO. Results showed that 1.0 metal loaded ZnO catalysts have the highest efficiency of photocatalytic degradation of methyl orange.

3.3. Analysis

3.3.1. Characterization Techniques

Different analytical techniques are used to determine the activity of the catalysts. The surface morphological study of the pure ZnO and metal loaded ZnO catalysts was carried out with Scanning Electron Microscopy (SEM) in combination with Energy Dispersive X-ray analysis on an ESEM-FEG/EDAX Philips XL-30 instrument operating at 20 kV using catalyst powders supported on carbon tape.

The crystal structure identification of synthesized catalysts was obtained by X–ray powder diffraction (XRD) using a Rigaku-D/MAX-Ultima diffractometer with Cu Kα radiation ($\lambda = 1.54$ Å) operating at 40 kV and 40 mA and at a scan speed of 2^{o} min^{-1}.

Nitrogen adsorption and desorption isotherms at liquid nitrogen temperature 77 K, were measured on a Quantachrome Nova 2200 automated gas adsorption system. The values of the specific surface area were obtained by a multi-point analysis of adsorption isotherms (BET).

Atomic Force Microscopy (AFM) is a technique where a small probe is scanned across the sample to obtain information about the sample's surface. Microscopic features of pure ZnO and all the other metal loaded catalysts were obtained by using AFM at room temperature with an Universal Scanning Probe Microscope (USPM) (Queosent-Ambios Technology, Santa Cruz, CA). Sample preparation is done by a dip-coater (KSV-LM) forming thin films of the catalysts. Glass microscope slides were dipped in aqueous solution containing 0.1 wt per cent of the catalysts and then pulled out at a constant speed of 20 mm min^{-1} to obtain the films of uniform thickness. The contact mode imaging where the tip scans the sample in close contact with the surface was performed using silicon nitride cantilever probe with a nominal tip radius of 5-10 nm.

The UV-Vis diffuse reflectance spectra (UV-Vis DRS) of the catalysts obtained by using UV-Vis Spectrophotometer (Shimadzu 1600) with an integrating sphere reflectance accessory. The catalysts (~5mg) was finely crushed and applied over Whatman 40 filter paper. The spectra were recorded in the range 200-800 nm for all catalysts using a filter paper as the reference.

The contact angle measurement was performed using KSV CAM 101. The sessile drop method was used in the presence of water at room temperature. Each contact angle reported was the mean value of five measurements taken at different positions on the film.

3.3.2. Photocatalytic Decolorization of Methyl Orange

Photocatalytic experiments were performed in a laboratory constructed irradiation box (Figure 3.4). Irradiation was carried out by using eight-black light fluorescent lamps (8x15 W) that supply light of wavelength 320-440 nm (Figure 3.5) which were positioned to surround the flask from two sides in the irradiation box. The incident photon flux for all lamps was measured as $4.7x10^{15}$ photons/s using potassium ferrioxalate actinometer [53]. A fan was placed at the back-side of the box to eliminate any heating effects of the lamps.

In the experiments carried out in this study, a pyrex erlenmeyer flask was used which has an inlet and outlet for the circulation of air and collection of aliquots, respectively. Air circulation was supplied by using a Cole-Parmer peristaltic pump (2000 rpm) and connection between pump and flask were made with Tygon tubing**.** Pyrex erlenmeyer is placed inside the irradiation box. Photocatalytic decolorization was carried out by mixing 100 ml of a known concentration methyl orange solution at room temperature and 0.1 g of catalysts. Prior to irradiation, the suspension was aerated and magnetically stirred in the dark for 30 min to reach adsorption equilibrium condition followed by UV irradiation. Aliquots were withdrawn from the flask-outlet at specific time intervals. And then, they filtered immediately through a millipore filter (0.45 μm) before UV analysis. The calibration of the UV-Vis spectrophotometer was performed at different pH values; 2-10 (Figure 3.6). The UV-Vis spectra for methyl orange solution show two adsorption maxima. The first band observed at 274 nm and the second band at 464 nm. The band at 464 nm was used to monitor the effect of the photocatalysis on the decolorization of MO during the photocatalytic degradation runs.

Figure 3.4. Irradiation Box

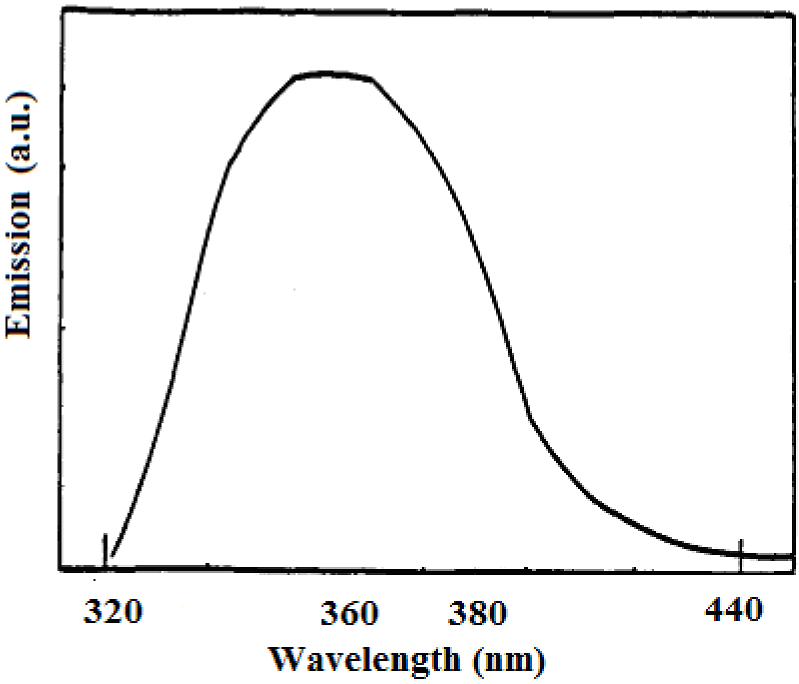

Figure 3.5. Emission spectrum of a black light fluorescent lamp

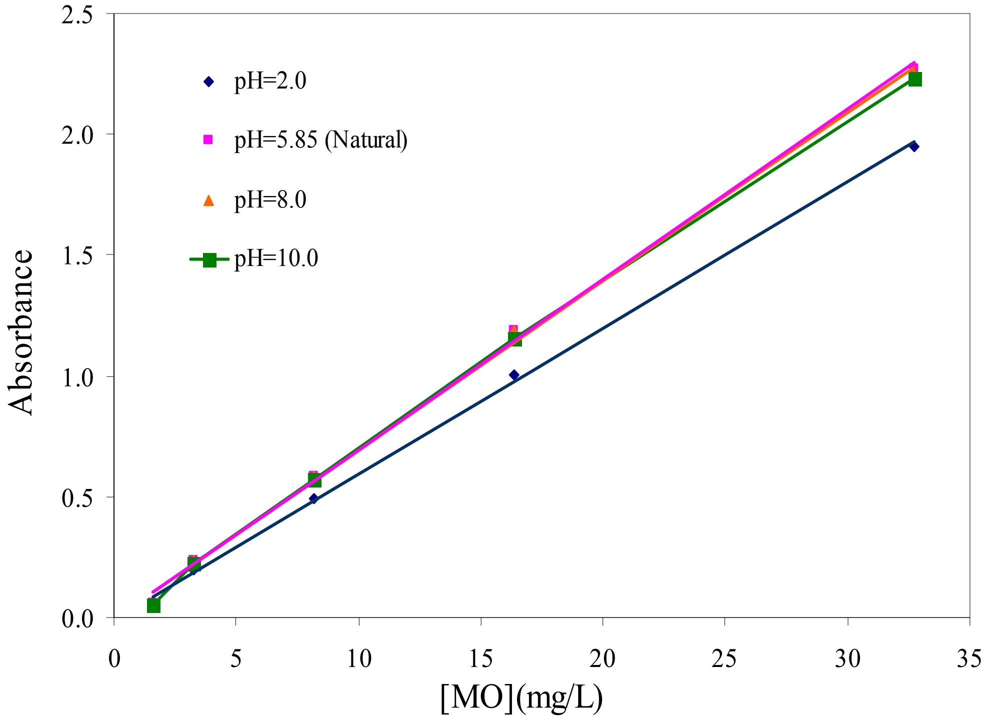

Figure 3.6. Calibration of UV-Vis spectroscopy in the pH range of 2-10. Conditions: [MO]= 8.17 mg/L, I= 4.7x10^{15} photons/s, T=298 K

4. RESULTS and DISCUSSION

4.1. Characterization Results

4.1.1. Characterization of Pure ZnO

4.1.1.1. X-ray Diffraction (XRD) Analysis. X-ray diffraction method is used for the fingerprint characterization of catalyst particles and the determination of their structure. Figure 4.1 shows the XRD spectrum of pure ZnO that is synthesized by coprecipitation method. The characteristic ZnO diffraction peak (101) is detected at 36.440° (2θ). Other ZnO diffractions of (100), (002), (102), (110), (103), (200), (112) and (201) also appeared at 31.97, 34.63, 47.74, 56.78, 63.02, 66.56, 68.14 and 69.29° (2θ), respectively. The peak positions in Figure 4.1 correspond very well with theoretical ZnO patterns. The crystalline size of pure ZnO catalyts is calculated from the (101) peak as 15.2 nm for pure ZnO (400^{o}C) (Table 4.1) by applying Scherrer's equation (Equation 2.10).

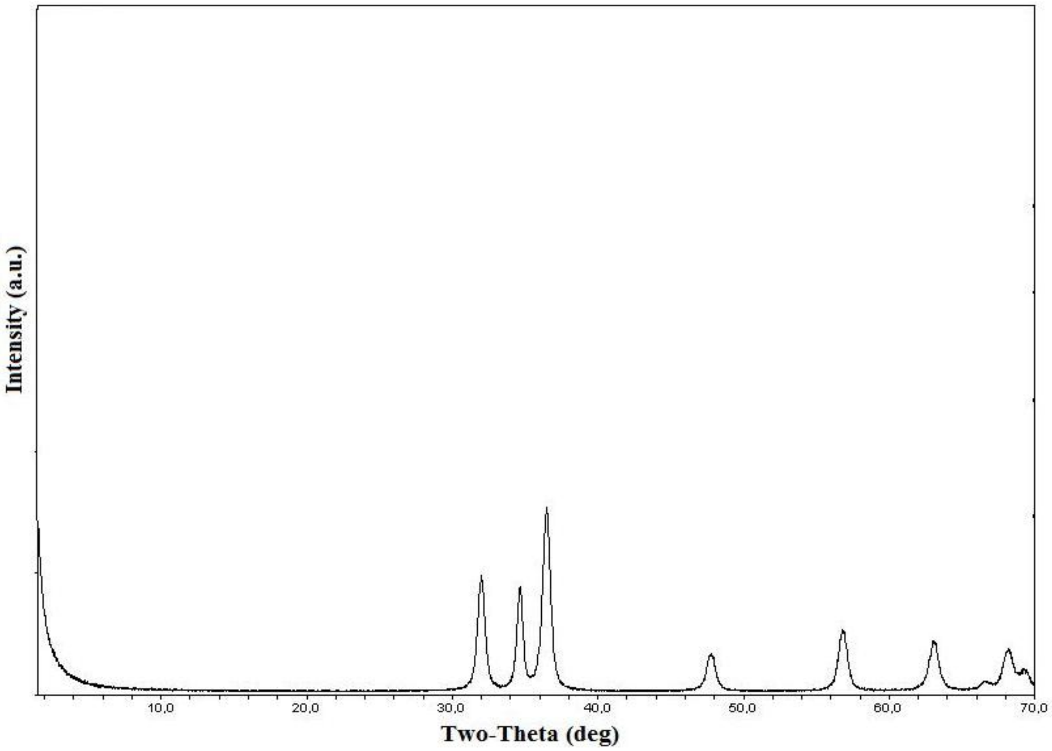

Figure 4.1. XRD patterns of Pure ZnO catalyst

4.1.1.2. BET Analysis. Specific surface areas of ZnO (Merck) and ZnO catalyst obtained by the co-precipitation method (Pure ZnO) are measured by multi-point BET analysis. The commercial catalyst exhibits only 8.66 m^2/g surface area while the as-synthesized catalyst reveals approximately 59.46 m^2/g surface area. Moreover, pore volume of the as-synthesized catalyst is much higher than the value obtained for the commercial catalyst. However, there is no considerable variation in the pore diameters of the catalysts. This indicates that the pore volumes of the catalysts do not depend only on the pore radii, but also depend on the shape of the crystal structures.

Table 4.1. Surface area, pore volume and pore size values of Pure ZnO

Catalyst	BET (m^2/g)	Pore volume (cm^3/g)	Pore Size (nm)
ZnO (Merck)	8.66	0.004	3.5
Pure ZnO	59.46	0.028	3.6

4.1.1.3. Scanning Electron Microscopy (SEM) Analysis. Structural morphology of pure ZnO catalyst is revealed by SEM micrograph. Pure ZnO catalyst illustrated a well ordered morphology with similar kidney shaped crystals (Figure 4.2.). The EDX analysis of pure ZnO catalyst showed zinc and oxygen peak as expected (Figure 4.2 inset).

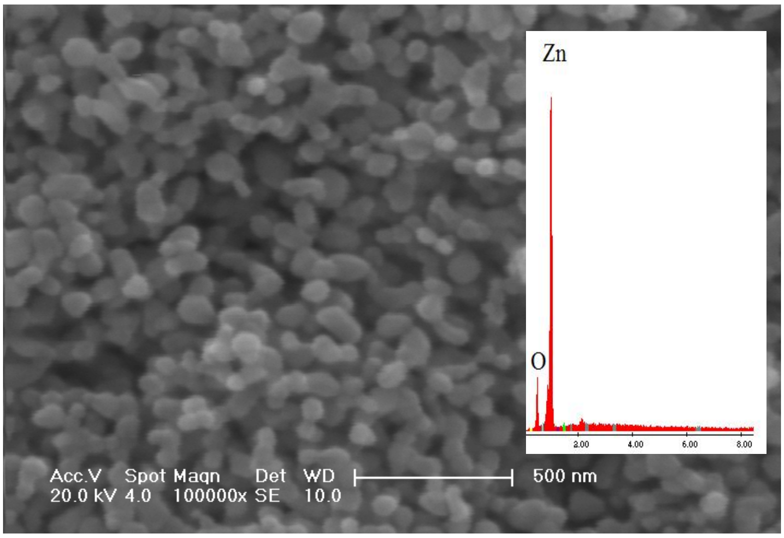

Figure 4.2. SEM image of pure ZnO. Inset: EDX spectrum of the whole surface

4.1.1.4. Atomic Force Microscopy (AFM) Analysis. The morphology of pure ZnO at 400^{o}C is analyzed using AFM technique. The three-dimensional (3-D) and two-dimensional (2-D) with particle size distribution plot AFM image of pure ZnO is shown in Figure 4.3. The corresponding AFM image showed spherical ZnO nanoparticles with uniform size. The data obtained from this image (not shown) was the average roughness value (R_a) of the sample. This value was approximately equal to 2.072 nm for pure ZnO. Two-dimensional (2-D) image (top-view) and underneath this image particle size distribution plot (Figure 4.3 A) of pure ZnO (400^{o}C) are also illustrated. In the distribution plot, a particle with 86.0 nm diameter is labeled as an example.

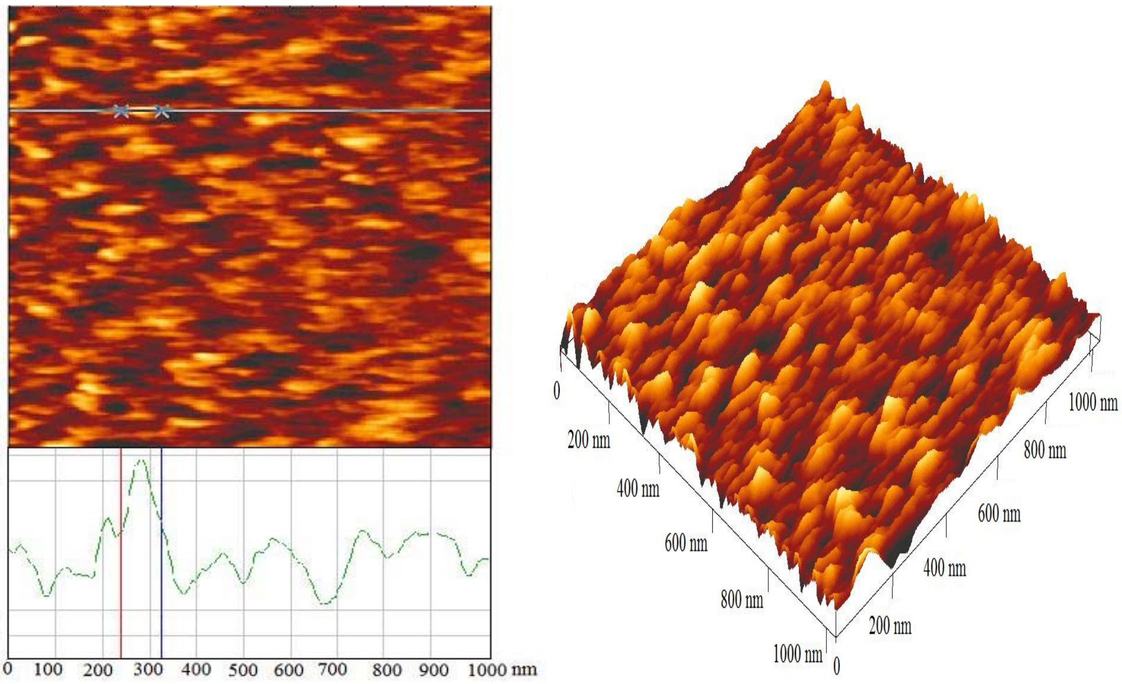

(A) Two-dimensional (top-view) image

(B) Three-dimensional

Figure 4.3. (A) Two-dimensional (top-view) image and (B) Three-dimensional AFM images of pure ZnO

It is showed that the particle size of catalyst extremely different from the XRD calculated size because the technique for the preparation of AFM samples which lead to forming of aggregates, is different than the technique for the preparation of XRD samples.

Due to aggloremation of particles, the measured values by AFM are higher than the size of single crystallites calculated by XRD.

4.1.2. Characterization of Lanthanum (La) Loaded ZnO

4.1.2.1. X-ray Diffraction (XRD) Analysis. The XRD spectras of 1.0 La-ZnO, 2.3 La-ZnO and 4.5 La-ZnO (400°C) catalysts, did not show any additional peaks suggesting that lanthanum oxide was uniformly dispersed in the ZnO surface and there was no change in the crystal structure upon La loading. However, additional diffractions due to the presence of La_2O_3 phase were observed in the XRD pattern of 4.5 La-ZnO catalyst at 800 and 1000°C meaning that calcination temperature enhanced the formation of La_2O_3 crystals. Diffraction peaks of La loaded ZnO catalysts were wider and lower in intensity than that of pure ZnO catalysts. Furthermore, the XRD peaks of La loaded ZnO got broader with increasing La content.

Table 4.2. gives the values of full width half maximum (FWHM) of (101) diffraction peaks and particles sizes (D) of the corresponding catalysts. ZnO crystal sizes do not vary with the content of La^{3+} ion. However, the increase in calcination temperature enhances the oxide formation of the metal ion.

Table 4.2. FWHM and crystal size values of La loaded ZnO

Catalyst		ZnO			La_2O_3	
	Plane	FWHM	D(nm)	Plane	FWHM	D (nm)
1.0 La-ZnO (400°C)	101	0.550	15.1	-	-	-
2.3 La-ZnO (400°C)	101	0.733	11.3	-	-	-
4.5 La-ZnO (400°C)	101	0.561	14.8	-	-	-
	Plane	ZnO FWHM	D(nm)	Plane	La_2O_3 FWHM	D (nm)
4.5 La-ZnO (600°C)	101	0.584	14.3	-	-	-
4.5 La-ZnO (800°C)	101	0.424	19.7	101	0.387	21.2
4.5 La-ZnO (1000°C)	101	0.259	32.2	101	0.268	30.6

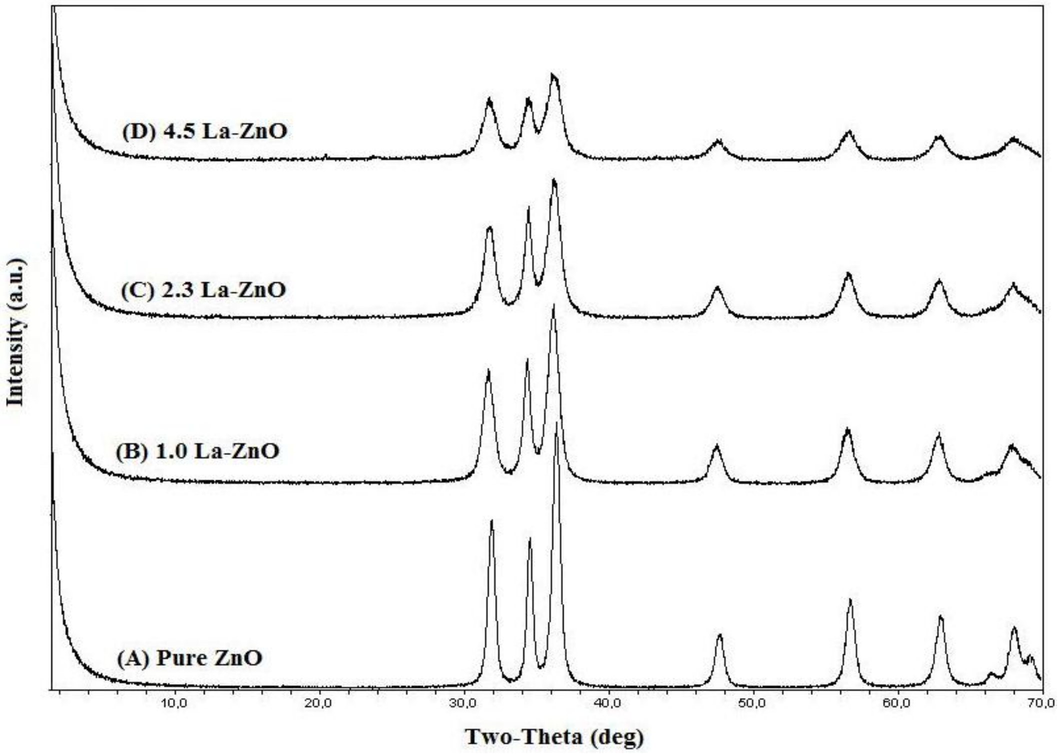

Figure 4.4. XRD patterns of pure ZnO and different content of La loaded ZnO catalysts

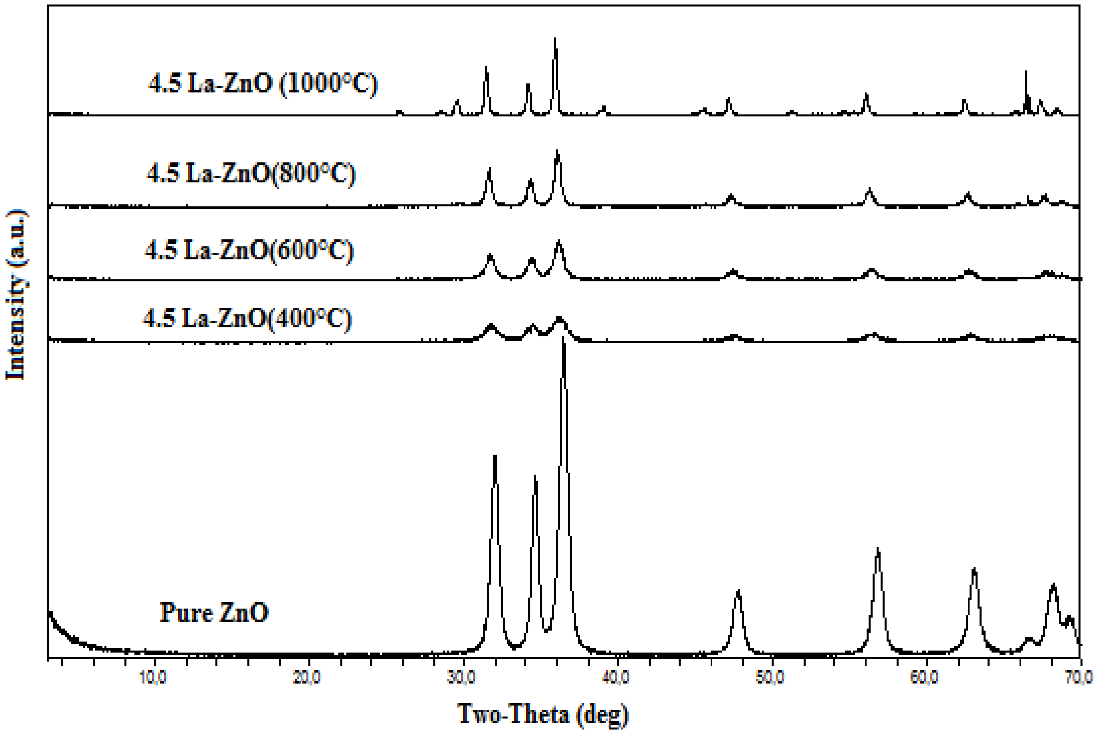

Figure 4.5. XRD patterns of 4.5 La-ZnO catalyst calcined at different temperatures

4.1.2.2. BET Analysis. The values for the specific surface area of 4.5, 2.3 and 1.0 La-ZnO catalysts are obtained as 84.22, 52.04 and 61.78 m^2/g by multi point BET analysis, respectively. It is observed that there is a slight difference between the pore volume and pore size values of the pure ZnO and La^{3+} loaded ZnO catalyst. Besides, pore sizes of the catalysts are very small with respect to the crystal sizes of La_2O_3 particles, indicating distribution of La_2O_3 particles on the surface of the catalysts.

Table 4.3. Surface area, pore volume and pore size values of La loaded ZnO

Catalyst	BET (m^2/g)	Pore volume (cm^3/g)	Pore Size (nm)
Pure ZnO	59.46	0.028	3.5
1.0 La-ZnO	61.78	0.030	3.6
2.3 La-ZnO	52.04	0.028	4.6
4.5 La-ZnO	84.22	0.039	3.5

4.1.2.3. Scanning Electron Microscopy (SEM) Analysis. The SEM image of the 2.3 La-ZnO is shown in Figure 4.6. It was noticed that aggregates were spherical and smaller than that of pure ZnO which indicates that the doping of La suppressed the growth of grains. The EDX analysis of 2.3 La-ZnO catalyst showed zinc, oxygen and lanthanum peaks (Figure 4.6 inset).

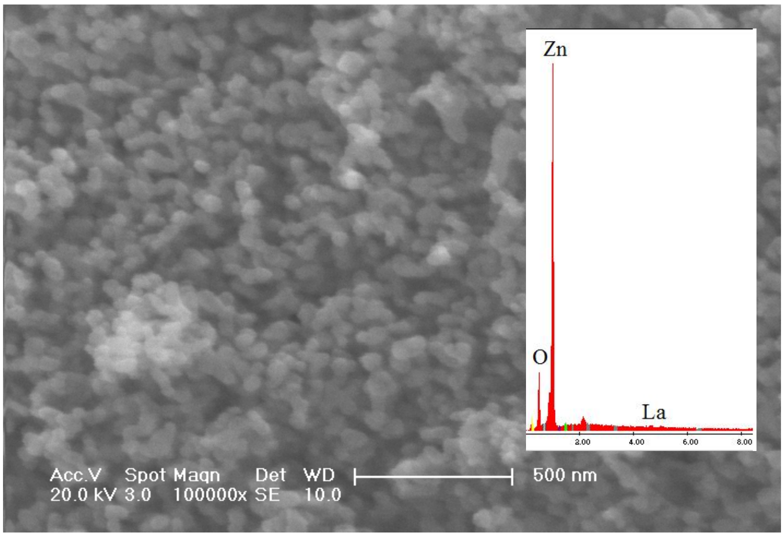

Figure 4.6. SEM image of 2.3 La-ZnO. Inset: EDX spectrum of the whole surface

4.1.2.4. Atomic Force Microscopy (AFM) Analysis.

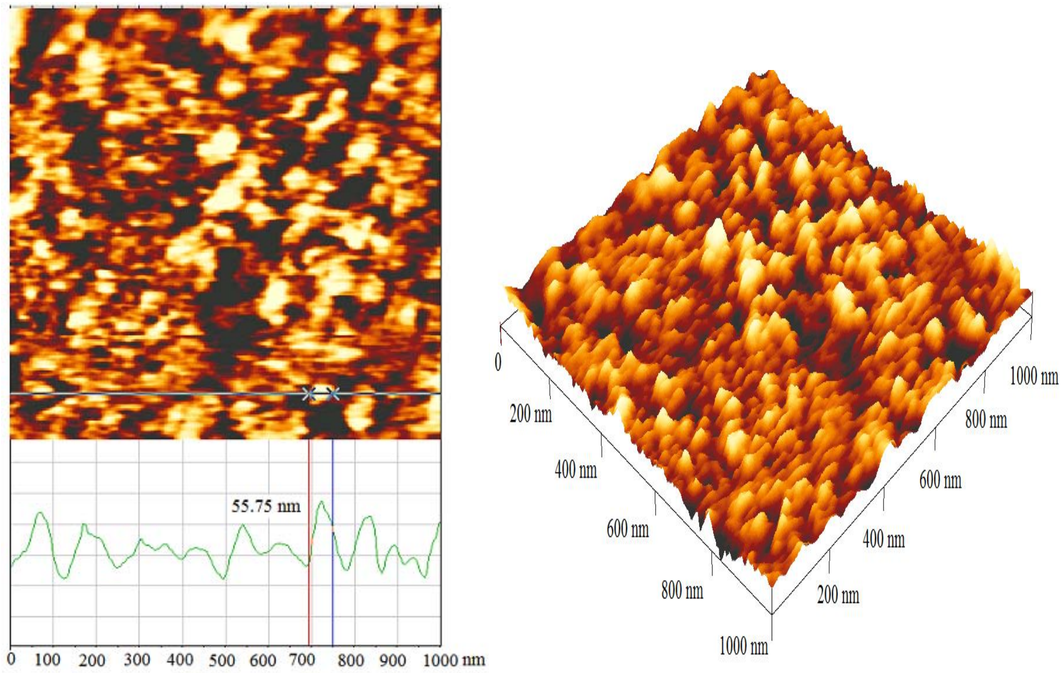

(A) Two-dimensional (top-view) image (B) Three-dimensional

Figure 4.7. (A) Two-dimensional (top-view) image and (B) Three-dimensional AFM images of 2.3 La- ZnO

In the presence of 2.3 La- ZnO catalyst, a uniform protrusion like structure is observed (Figure 4.7 B) and average roughness value (R_a) of 6.398 nm is obtained whereas it was 2.072 nm for the pure ZnO catalyst. Particle sizes were found to be lower in the presence of La loaded catalyst than pure ZnO. In the distribution plot, a particle (more than that seems a kind of aggregate) with 55.75 nm diameter is labeled as an example. Higher surface roughness and smaller particle size values of La loaded samples indicated higher porosity of the catalyst than pure ZnO.

4.1.2.5. Diffuse Reflectance Spectroscopy (DRS) Analysis.

In DRS spectrums, loading with rare earth metal ions make a blue shift in the absorption band of pure ZnO. This shift is enhanced with increasing the metal ion content in the final catalyst configuration. Such variation in absorption band of ZnO causes a slight increase in the band gap energy, reducing the electron-hole recombination reactions. Similar results are obtained in the DRS's of all other catalysts, therefore, in the following chapters only corresponding spectras are shown.

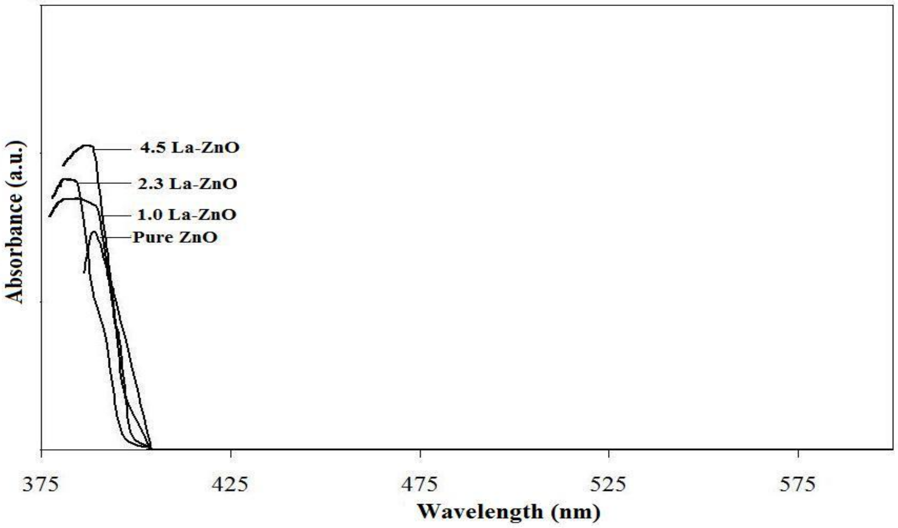

Figure 4.8. UV-vis diffuse reflectance spectra of pure ZnO and different amount La loaded ZnO

4.1.3. Characterization of Praseodymium (Pr) Loaded ZnO

4.1.3.1 X-ray Diffraction (XRD) Analysis. The XRD spectras of 1.0 Pr-ZnO and 2.3 Pr-ZnO (400°C) catalysts did not show any additional peaks whereas additional diffractions due to the presence of Pr_2O_3 phase were observed in the XRD pattern of 4.5 Pr-ZnO (400°C) catalyst. Higher calcination temperatures for a fixed metal content enhanced the formation of metal oxide phase.

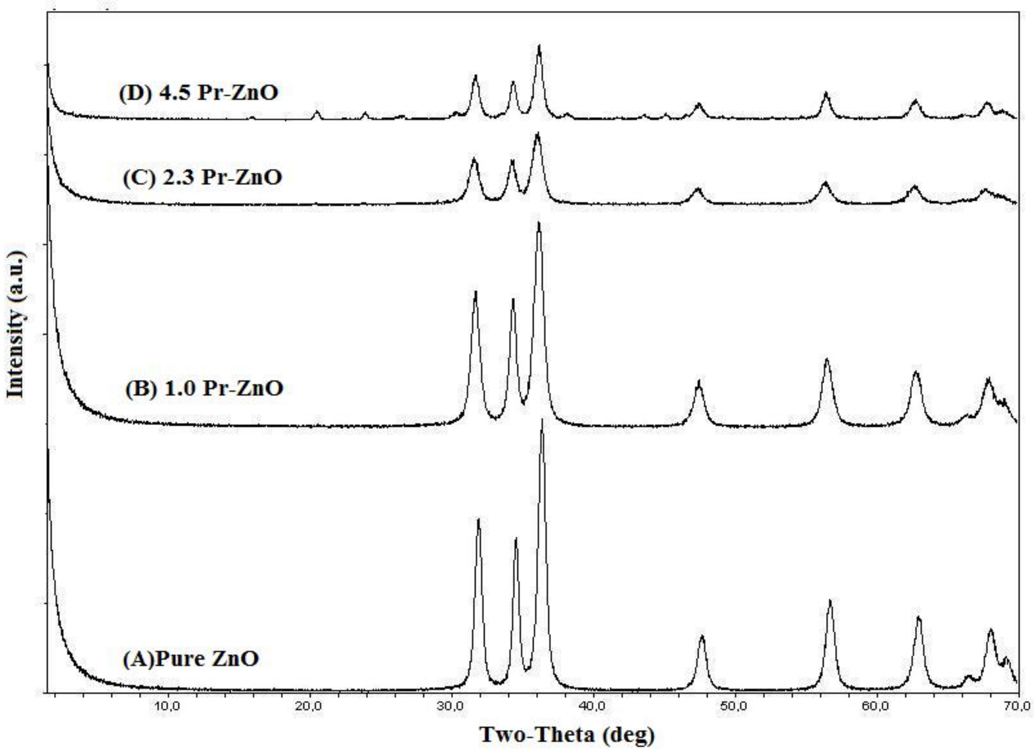

Figure 4.9. XRD patterns of pure ZnO and different content of Pr loaded ZnO catalysts

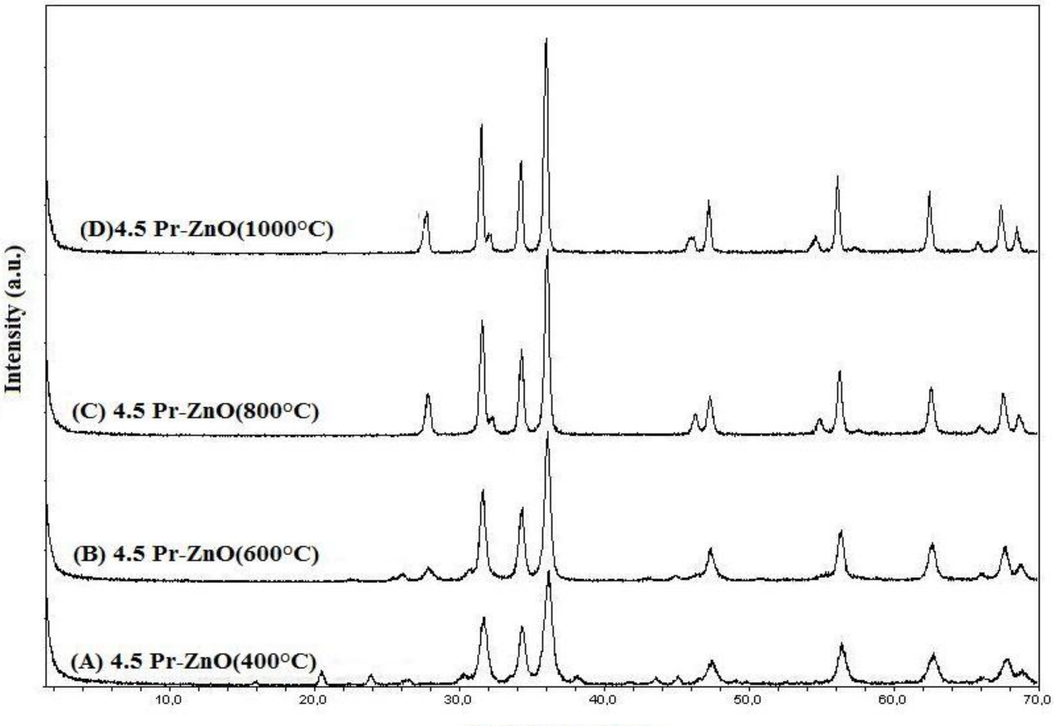

Figure 4.10. XRD patterns of 4.5 Pr-ZnO catalyst calcined at different temperatures

Table 4.4. FWHM and crystal size values of Pr loaded ZnO

Catalyst						
		ZnO			PrO	
	Plane	FWHM	D(nm)	Plane	FWHM	D (nm)
1.0 Pr-ZnO (400°C)	101	0.672	12.4	-	-	-
2.3 Pr-ZnO (400°C)	101	0.699	12.0	-	-	-
4.5 Pr-ZnO (400°C)	101	0.548	15.2	111	0.365	22.4
	Plane	ZnO FWHM	D(nm)	Plane	PrO FWHM	D (nm)
4.5 Pr-ZnO (600°C)	101	0.437	19.1	111	0.525	15.6
4.5 Pr-ZnO (800°C)	101	0.360	23.2	111	0.391	21.0
4.5 Pr-ZnO (1000°C)	101	0.300	27.8	111	0.365	22.4

4.1.3.2. BET Analysis. The values for the specific surface area of 4.5, 2.3 and 1.0 Pr-ZnO catalysts are obtained as 50.827, 56.993 and 72.203 m^2/g by multi point BET analysis, respectively. It is observed that there is a slight difference between the pore volume and pore size values of the pure ZnO and Pr^{3+} loaded ZnO catalyst. Besides, pore sizes of the catalysts are very small with respect to the crystal sizes of Pr_2O_3 particles, indicating distribution of Pr_2O_3 particles on the surface of the catalysts.

Table 4.5. Surface area, pore volume and pore size values of Pr loaded ZnO

Catalyst	BET (m^2/g)	Pore volume (cm^3/g)	Pore Size (nm)
Pure ZnO	59.46	0.028	3.5
1.0 Pr-ZnO	72.2	0.035	3.8
2.3 Pr-ZnO	56.99	0.028	2.6
4.5 Pr-ZnO	50.83	0.024	4.0

4.1.3.3. Scanning Electron Microscopy (SEM) Analysis. The SEM image of the 2.3 Pr-ZnO is shown in Figure 4.11. It was noticed that aggregates were rodlike rather than spherical particles. The EDX analysis of 2.3 Pr-ZnO catalyst showed zinc, oxygen and praseodymium peaks (Figure 4.11 inset).

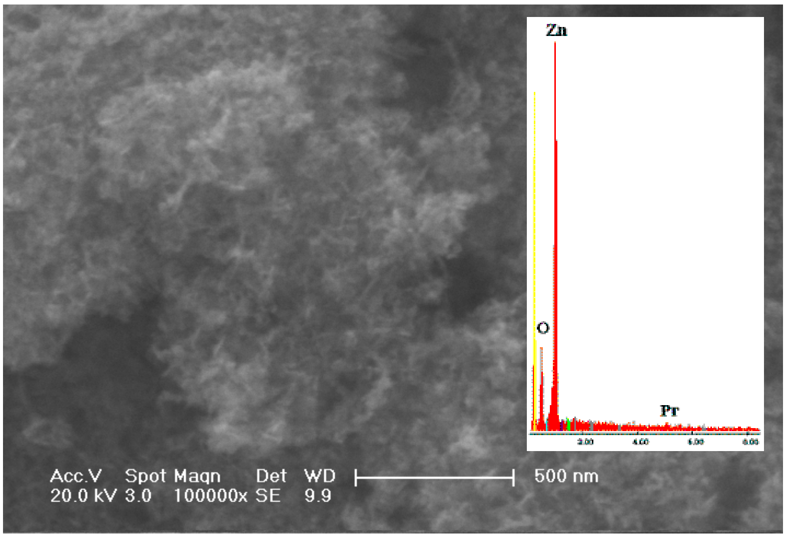

Figure 4.11. SEM image of 2.3 Pr-ZnO. Inset: EDX spectrum of the whole surface

4.1.3.4. Atomic Force Microscopy (AFM) Analysis. The three-dimensional (3-D) AFM image of 2.3 Pr-ZnO is shown in Figure 4.13 B. In the presence of 2.3 Pr-ZnO catalyst, a uniform protrusion like structure (Figure 4.13 A) is observed, too. Average roughness value (R_a) of 6.688 nm is obtained and a particle with 34 nm diameter is labeled as an example in the distribution plot.

4.1.3.5. Diffuse Reflectance Spectroscopy (DRS) Analysis

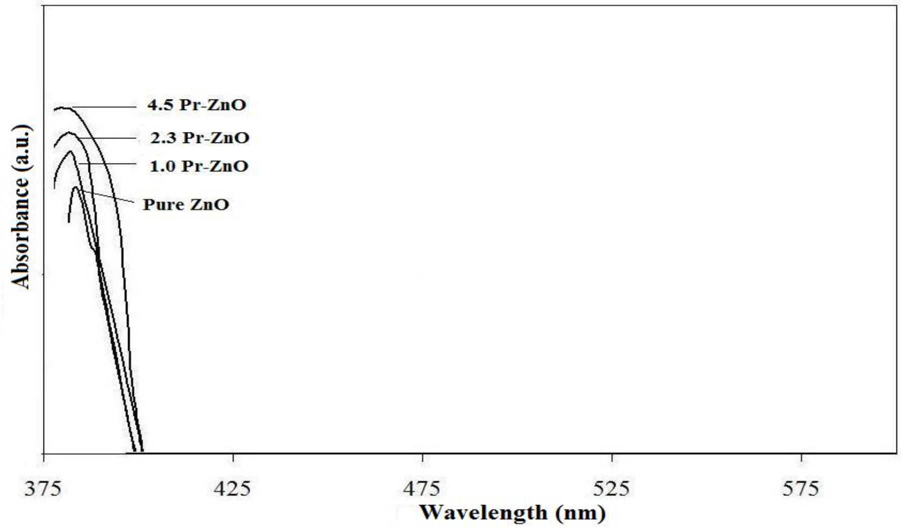

Figure 4.12. UV-vis diffuse reflectance spectra of pure ZnO and different amount Pr loaded ZnO

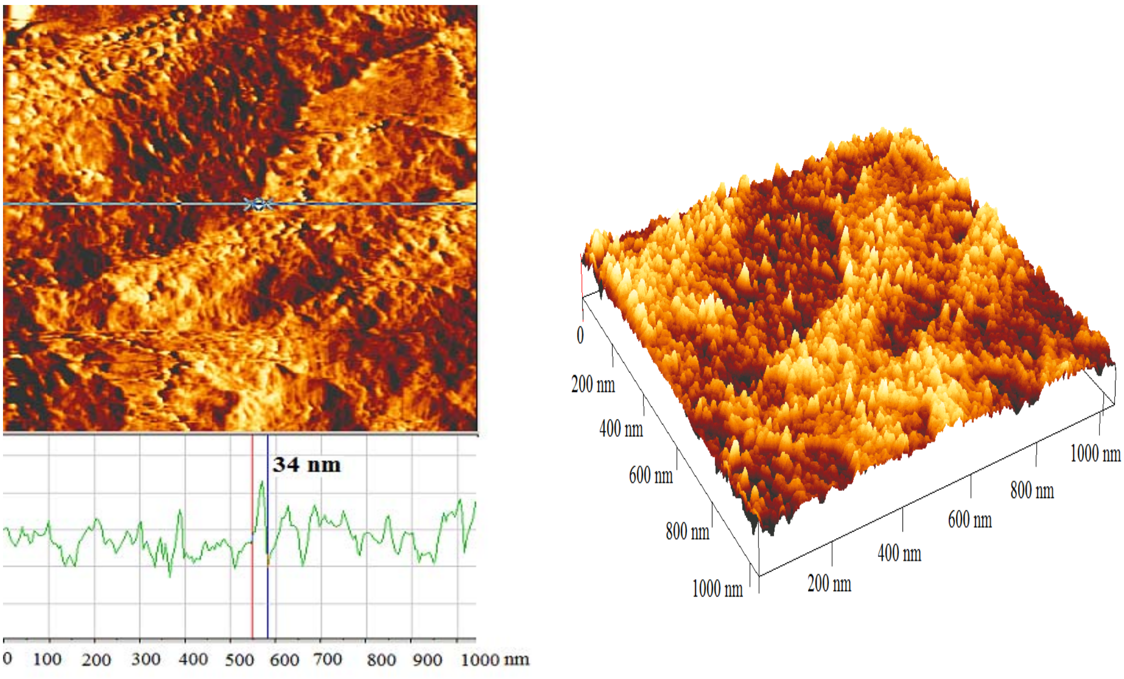

(A) Two-dimensional (top-view) image (B) Three-dimensional

Figure 4.13. (A) Two-dimensional (top-view) image and (B) Three-dimensional AFM images of 2.3 Pr- ZnO

4.1.4. Characterization of Neodymium (Nd) Loaded ZnO

4.1.4.1. X-ray Diffraction (XRD) Analysis. The XRD spectras of 1.0 Nd-ZnO, 2.3 Nd-ZnO and 4.5 Nd-ZnO (400^{o}C) catalysts, did not show any additional peaks. However, additional diffractions due to the presence of Nd_2O_3 phase were observed in the XRD pattern of 4.5 Nd-ZnO catalyst at 600, 800 and 1000˚C meaning that calcination temperature enhanced the formation of Nd_2O_3 crystals.

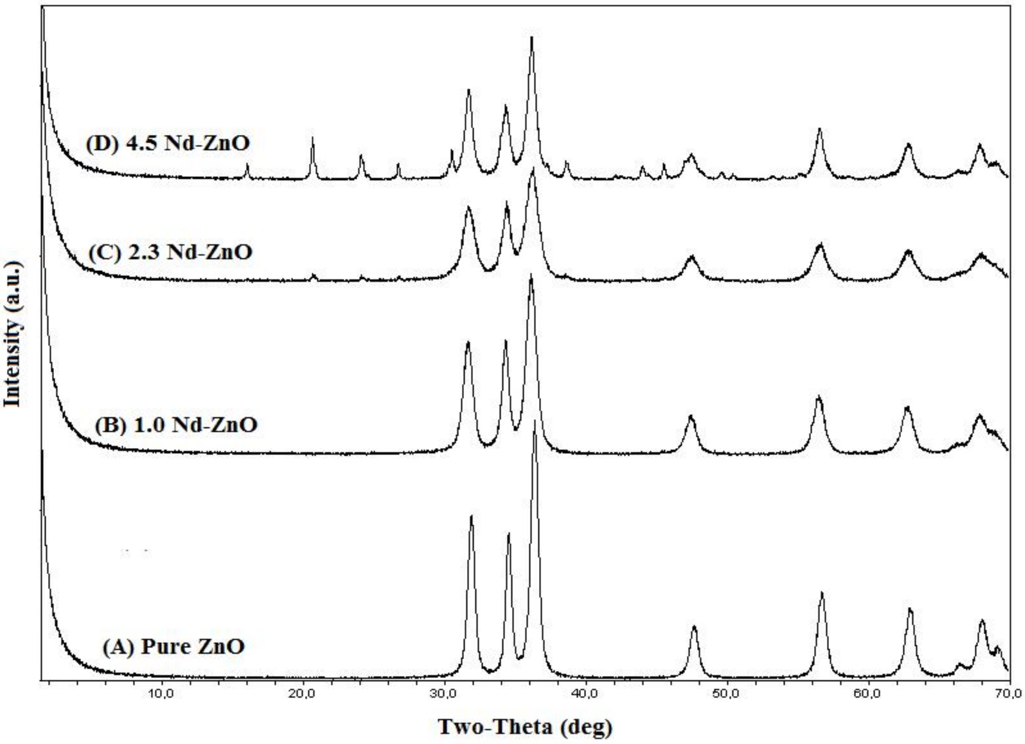

Figure 4.14. XRD patterns of pure ZnO and different content of Nd loaded ZnO catalysts

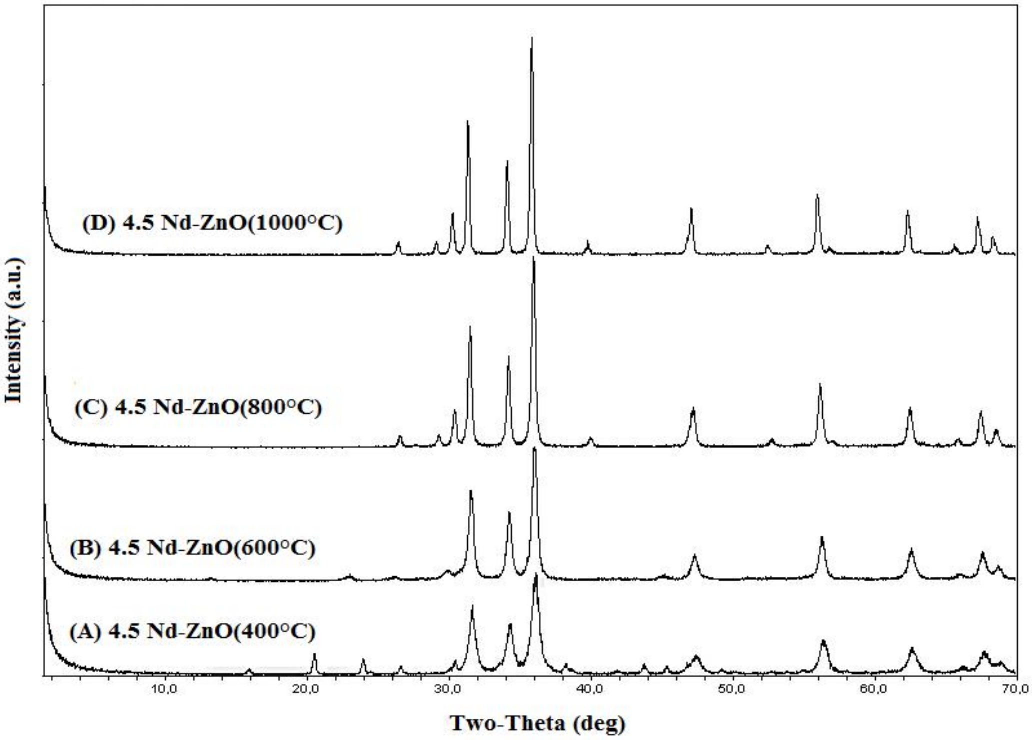

Figure 4.15. XRD patterns of 4.5 Nd-ZnO catalyst calcined at different temperatures

Table 4.6. FWHM and crystal size values of Nd loaded ZnO

Catalyst		ZnO			Nd_2O_3	
	Plane	FWHM	D(nm)	Plane	FWHM	D (nm)
1.0 Nd-ZnO (400˚C)	101	0.678	12.3	-	-	-
2.3 Nd-ZnO (400˚C)	101	0.748	11.2	-	-	-
4.5 Nd-ZnO (400˚C)	101	0.566	14.8	-	-	-
	Plane	ZnO FWHM	D(nm)	Plane	Nd_2O_3 FWHM	D (nm)
4.5 Nd-ZnO (600˚C)	101	0.436	19.0	101	0.562	14.6
4.5 Nd-ZnO (800˚C)	101	0.306	27.3	101	0.287	28.7
4.5 Nd-ZnO (1000˚C)	101	0.233	35.8	101	0.233	36.3

4.1.4.2. BET Analysis. The values for the specific surface area of 4.5, 2.3 and 1.0 Nd-ZnO catalysts are obtained as 52.385, 60.718 and 70.01 by multi point BET analysis, respectively. It is observed that there is a slight difference between the pore volume and pore size values of the pure ZnO and Nd^{3+} loaded ZnO catalyst. Besides, pore sizes of the catalysts are very small with respect to the crystal sizes of Nd_2O_3 particles, indicating distribution of Nd_2O_3 particles on the surface of the catalysts.

Table 4.7. Surface area, pore volume and pore size values of Nd loaded ZnO

Catalyst	BET (m^2/g)	Pore volume (cm^3/g)	Pore Size (nm)
Pure ZnO	59.46	0.028	3.5
1.0 Nd-ZnO	70.01	0.026	3.1
2.3 Nd-ZnO	60.72	0.027	2.6
4.5 Nd-ZnO	52.38	0.025	3.4

4.1.4.3. Scanning Electron Microscopy (SEM) Analysis. The SEM image of the 2.3 Nd-ZnO is shown in Figure 4.16. It was noticed that aggregates has the morphology of nanorod. The EDX analysis of 2.3 Nd-ZnO catalyst showed zinc, oxygen and neodymium peaks (Figure 4.16 inset).

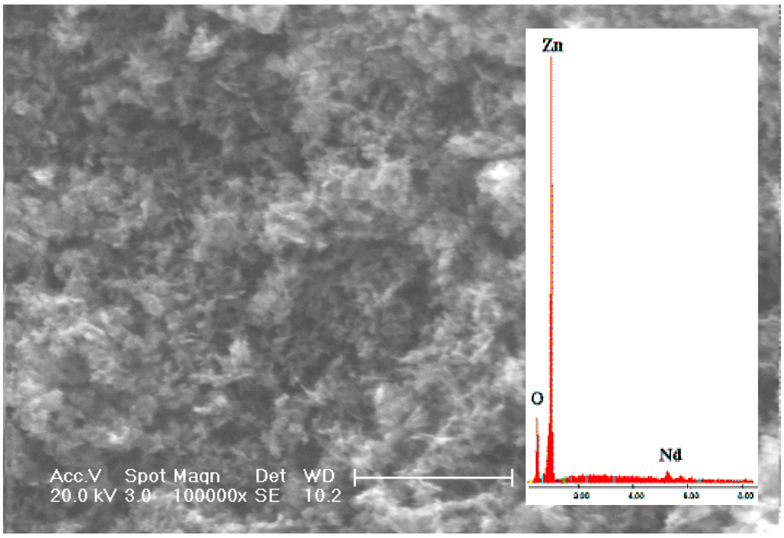

Figure 4.16. SEM image of 2.3 Nd-ZnO. Inset: EDX spectrum of the whole surface

4.1.3.4. Atomic Force Microscopy (AFM) Analysis. The three-dimensional (3-D) AFM image of 2.3 Nd-ZnO is shown in Figure 4.18 B. It can be observed that uniform protrusion like structures are bigger in the presence of 2.3 Nd-ZnO catalyst. Average roughness value (R_a) of 1.140 nm is obtained and a particle with 60.44 nm diameter is labeled as an example in the distribution plot.

4.1.4.5. Diffuse Reflectance Spectroscopy (DRS) Analysis

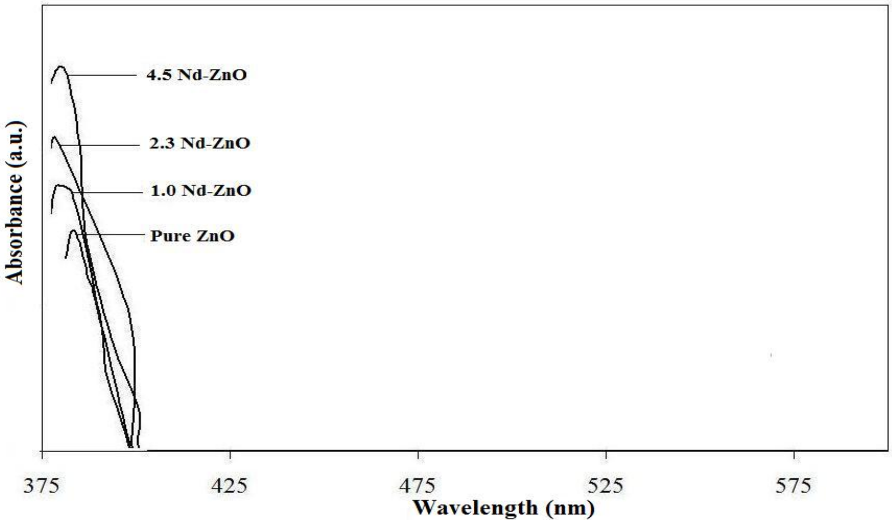

Figure 4.17. UV-vis diffuse reflectance spectra of pure ZnO and different amount Nd loaded ZnO

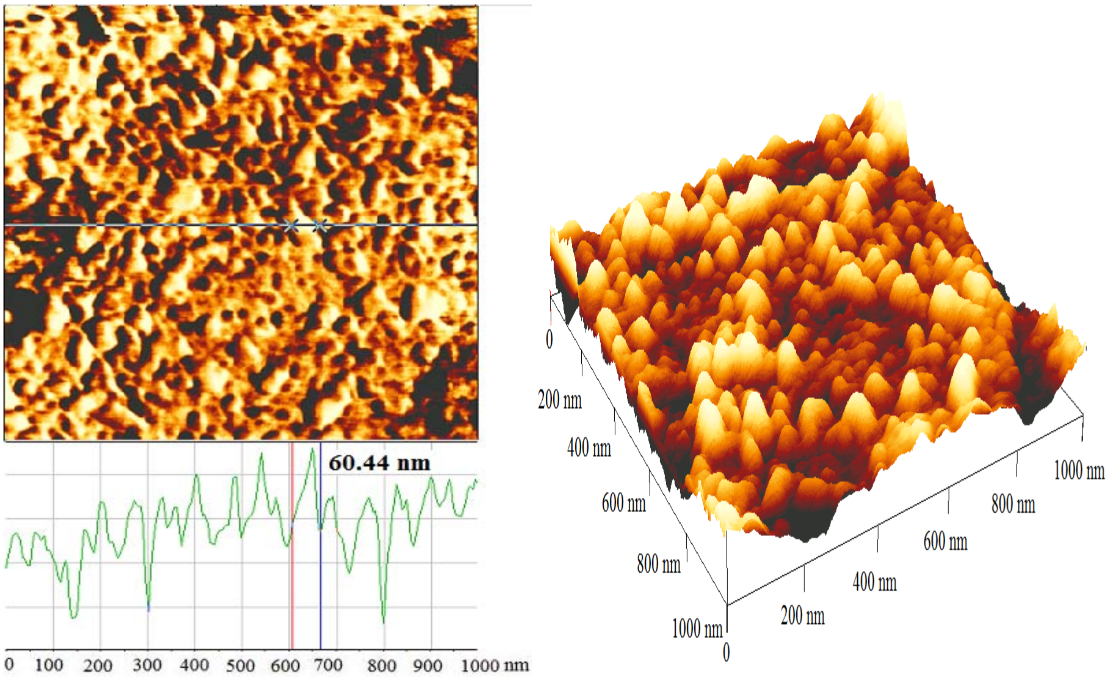

A) Two-dimensional (top-view) image

(B) Three-dimensional

Figure 4.18. (A) Two-dimensional (top-view) image and (B) Three-dimensional AFM images of 2.3 Nd- ZnO

4.1.5. Characterization of Dysprosium (Dy) Loaded ZnO

<u>4.1.5.1. X-ray Diffraction (XRD) Analysis.</u> The XRD spectras of 1.0 Dy-ZnO, 2.3 Dy-ZnO and 4.5 Dy-ZnO (400°C) catalysts, did not show any additional peaks. However, additional diffractions due to the presence of Dy_2O_3 phase were observed in the XRD pattern of 4.5 Dy-ZnO catalyst at 800 and 1000˚C meaning that calcination temperature enhanced the formation of Dy_2O_3 crystals.

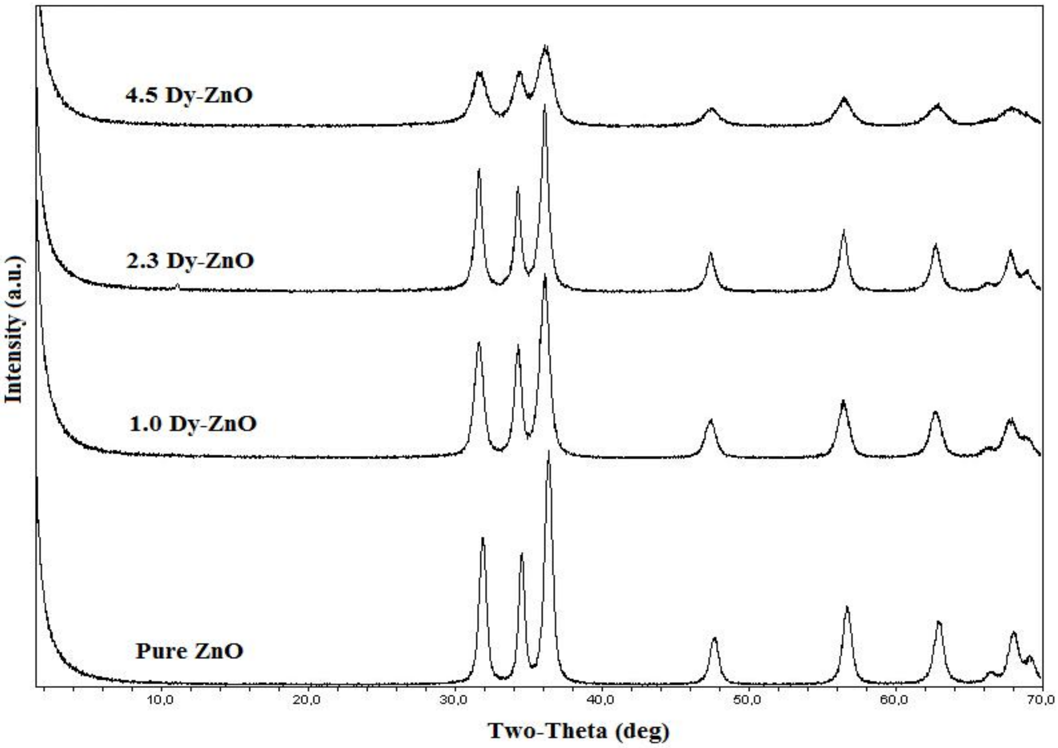

Figure 4.19. XRD patterns of pure ZnO and different content of Dy loaded ZnO catalysts

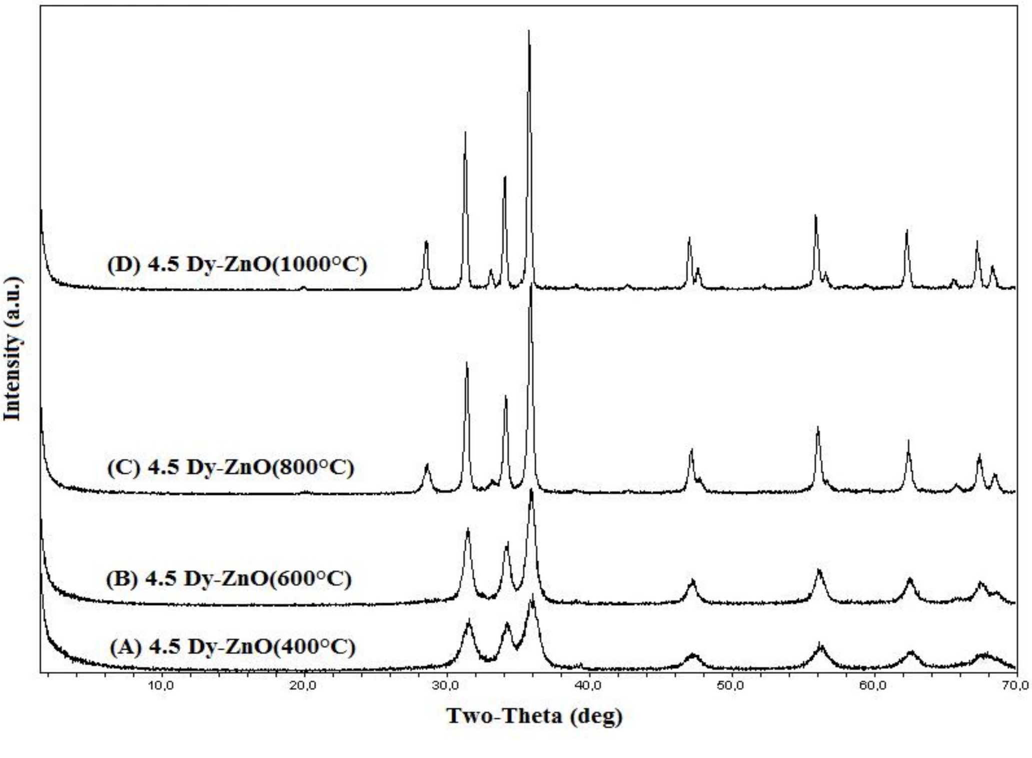

Figure 4.20. XRD patterns of 4.5 Dy-ZnO catalyst calcined at different temperatures

Table 4.8. FWHM and crystal size values of Dy loaded ZnO

Catalyst		ZnO			Dy_2O_3	
	Plane	FWHM	D(nm)	Plane	FWHM	D (nm)
1.0 Dy-ZnO (400°C)	101	0.639	13.1	-	-	-
2.3 Dy-ZnO (400°C)	101	0.525	16.0	-	-	-
4.5 Dy-ZnO (400°C)	101	0.904	9.2	-	-	-
	Plane	ZnO FWHM	D(nm)	Plane	Dy_2O_3 FWHM	D (nm)
4.5 Dy-ZnO (600°C)	101	0.623	13.4	-	-	-
4.5 Dy-ZnO (800°C)	101	0.340	24.6	222	0.444	20.3
4.5 Dy-ZnO (1000°C)	101	0.251	33.3	222	0.308	26.6

4.1.5.2. BET Analysis. The values for the specific surface area of 4.5, 2.3 and 1.0 Dy-ZnO catalysts are obtained as 64.110, 60.847 and 66.965 m^2/g by multi point BET analysis, respectively. It is observed that there is a slight difference between the pore volume and pore size values of the pure ZnO and Dy^{3+} loaded ZnO catalyst. Besides, pore sizes of the catalysts are very small with respect to the crystal sizes of Dy_2O_3 particles, indicating distribution of Dy_2O_3 particles on the surface of the catalysts.

Table 4.9. Surface area, pore volume and pore size values of Dy loaded ZnO

Catalyst	BET (m^2/g)	Pore volume (cm^3/g)	Pore Size (nm)
Pure ZnO	59.46	0.028	3.5
1.0 Dy-ZnO	66.96	0.031	3.5
2.3 Dy-ZnO	60.85	0.028	3.7
4.5 Dy-ZnO	64.11	0.030	2.9

4.1.5.3. Scanning Electron Microscopy (SEM) Analysis. The SEM image of the 2.3 Dy-ZnO is shown in Figure 4.21. It was noticed that aggregates were spherical and smaller than that of pure ZnO which also indicates that the doping of Dy suppressed the growth of grains. The EDX analysis of 2.3 Dy-ZnO catalyst showed zinc, oxygen and dysprosium peaks (Figure 4.21 inset).

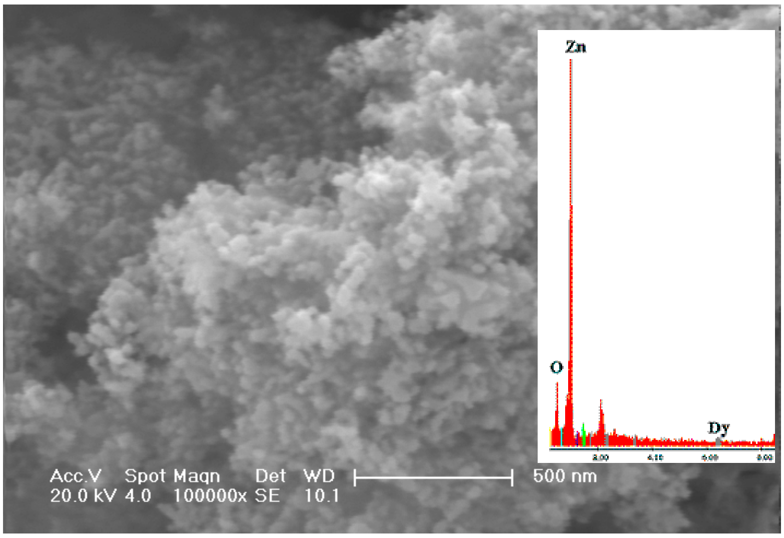

Figure 4.21. SEM image of 2.3 Dy-ZnO. Inset: EDX spectrum of the whole surface

4.1.5.4. Atomic Force Microscopy (AFM) Analysis. The three-dimensional (3-D) AFM image of 2.3 Dy-ZnO is shown in Figure 4.23 B. It can be observed that very uniform protrusion like structures are smaller in the presence of 2.3 Dy-ZnO catalyst. Average roughness value (R_a) of 0.6188 nm is obtained and a particle with 42.20 nm diameter is labeled as an example in the distribution plot.

4.1.5.5 Diffuse Reflectance Spectroscopy (DRS) Analysis

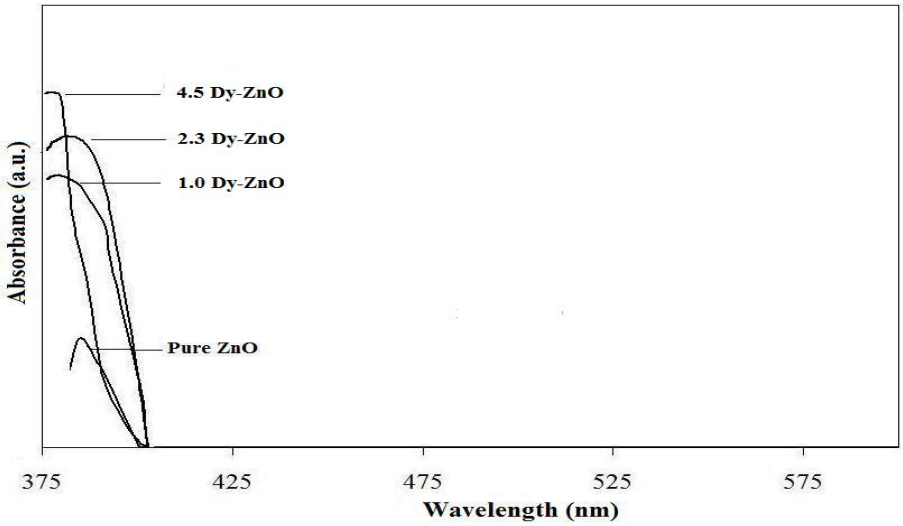

Figure 4.22. UV-vis diffuse reflectance spectra of pure ZnO and different amount Dy loaded ZnO

A) Two-dimensional (top-view) image (B) Three-dimensional

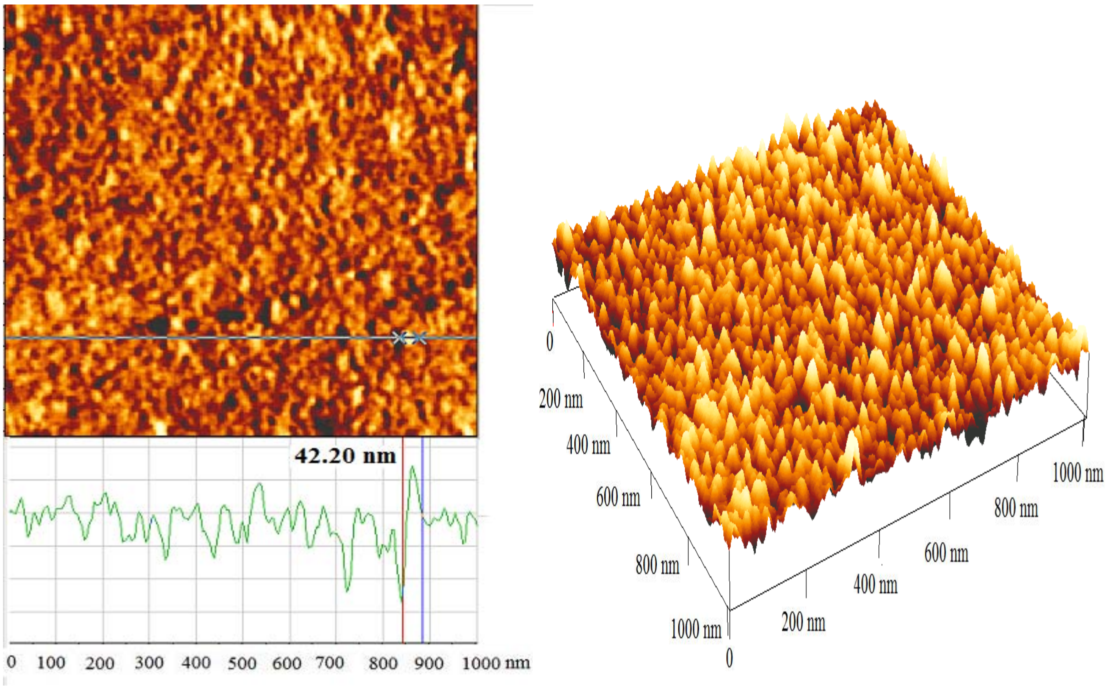

Figure 4.23. (A) Two-dimensional (top-view) image and (B) Three-dimensional AFM images of 2.3 Dy-ZnO

4.1.6. Characterization of Europium (Eu) Loaded ZnO

4.1.6.1. X-ray Diffraction (XRD) Analysis. The XRD spectras of 1.0 Eu-ZnO, 2.3 Eu-ZnO catalysts did not show any additional peaks. However, additional diffractions due to the presence of Dy_2O_3 phase were observed in the XRD pattern of 4.5 Eu-ZnO catalyst at 400, 600, 800 and 1000˚C meaning that calcination temperature enhanced the formation of Eu_2O_3 crystals.

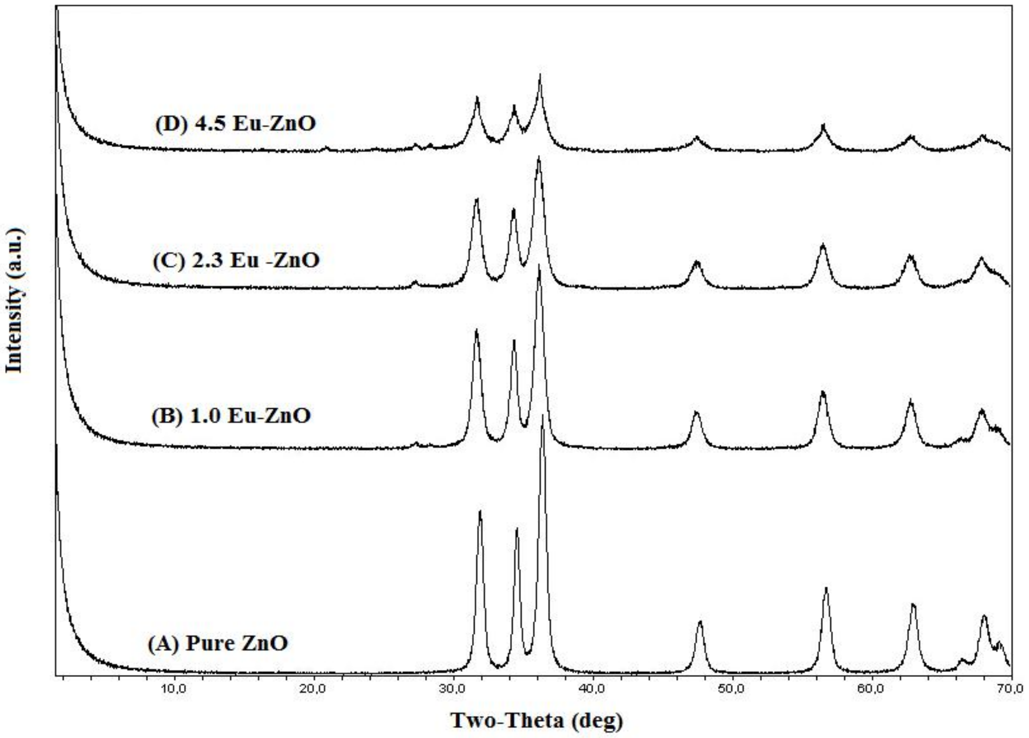

Figure 4.24. XRD patterns of pure ZnO and different content of Eu loaded ZnO catalysts

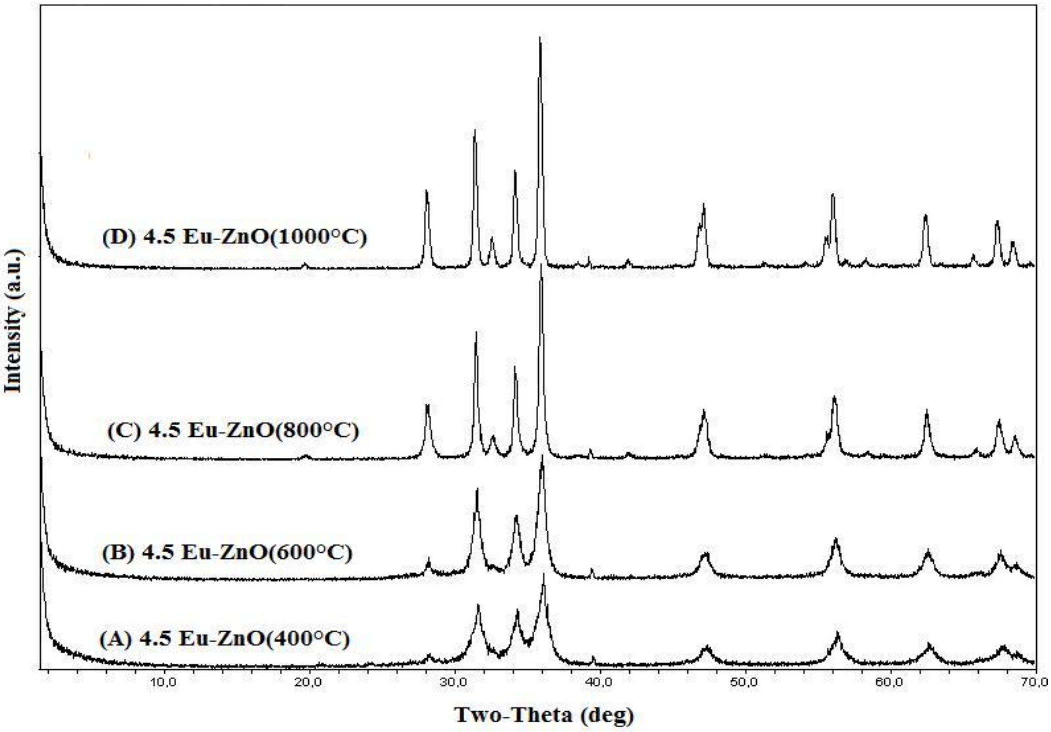

Figure 4.25. XRD patterns of 4.5 Eu-ZnO catalyst calcined at different temperatures

Table 4.10. FWHM and crystal size values of Eu loaded ZnO

Catalyst		ZnO			Eu_2O_3	
	Plane	FWHM	D(nm)	Plane	FWHM	D (nm)
1.0 Eu-ZnO (400˚C)	101	0.643	13.0	-	-	-
2.3 Eu-ZnO (400˚C)	101	0.698	12.0	-	-	-
4.5 Eu-ZnO (400˚C)	101	0.569	14.7	222	0.386	21.2
	Plane	ZnO FWHM	D(nm)	Plane	Eu_2O_3 FWHM	D (nm)
4.5 Eu-ZnO (600˚C)	101	0.554	15.1	222	0.257	32.5
4.5 Eu-ZnO (800˚C)	101	0.536	15.6	222	0.421	19.5
4.5 Eu-ZnO (1000˚C)	101	0.327	25.5	222	0.313	26.1

4.1.6.2. BET Analysis. The values for the specific surface area of 4.5, 2.3 and 1.0 Eu-ZnO catalysts are obtained as 67.679, 75.789 and 83.53 m^2/g by multi point BET analysis, respectively. It is observed that there is a slight difference between the pore volume and pore size values of the pure ZnO and Eu^{3+} loaded ZnO catalyst. Besides, pore sizes of the catalysts are very small with respect to the crystal sizes of Eu_2O_3 particles, indicating distribution of Eu_2O_3 particles on the surface of the catalysts.

Table 4.11. Surface area, pore volume and pore size values of Eu loaded ZnO

Catalyst	BET (m^2/g)	Pore volume (cm^3/g)	Pore Size (nm)
Pure ZnO	59.46	0.028	3.5
1.0 Eu-ZnO	67.68	0.032	3.6
2.3 Eu-ZnO	75.79	0.037	3.7
4.5 Eu-ZnO	83.53	0.038	2.9

4.1.6.3. Scanning Electron Microscopy (SEM) Analysis. The SEM image in Figure 4.26 shows bunches of thick rodlike shaped particles of the 2.3 Eu-ZnO. Also, it was observed that size distribution is narrow. The EDX analysis of 2.3 Eu-ZnO catalyst showed zinc, oxygen and europium peaks (Figure 4.26 inset).

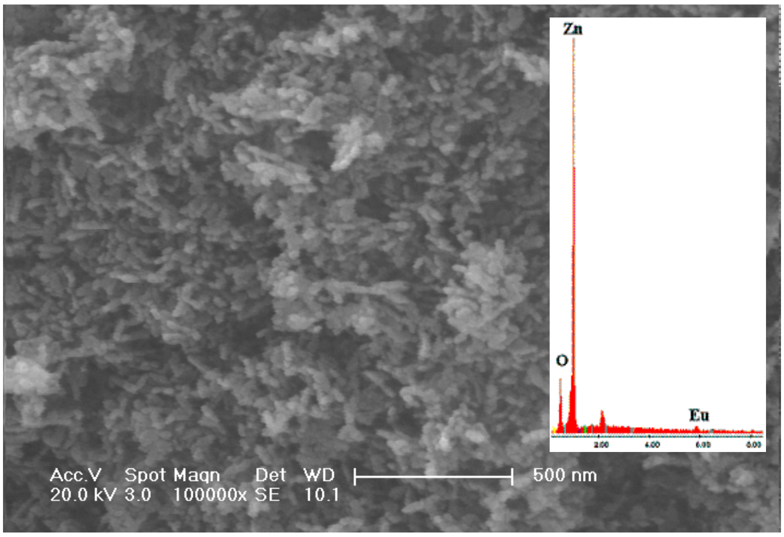

Figure 4.26. SEM image of 2.3 Eu-ZnO. Inset: EDX spectrum of the whole surface

4.1.6.4. Atomic Force Microscopy (AFM) Analysis. The three-dimensional (3-D) AFM image of 2.3 Eu-ZnO is shown in Figure 4.28 B. Bigger protrusion like structures can be observed in the presence of 2.3 Eu-ZnO catalyst. Average roughness value (R_a) of 3.670 nm is obtained and a particle with 86 nm diameter is labeled as an example in the distribution plot.

4.1.6.5. Diffuse Reflectance Spectroscopy (DRS) Analysis

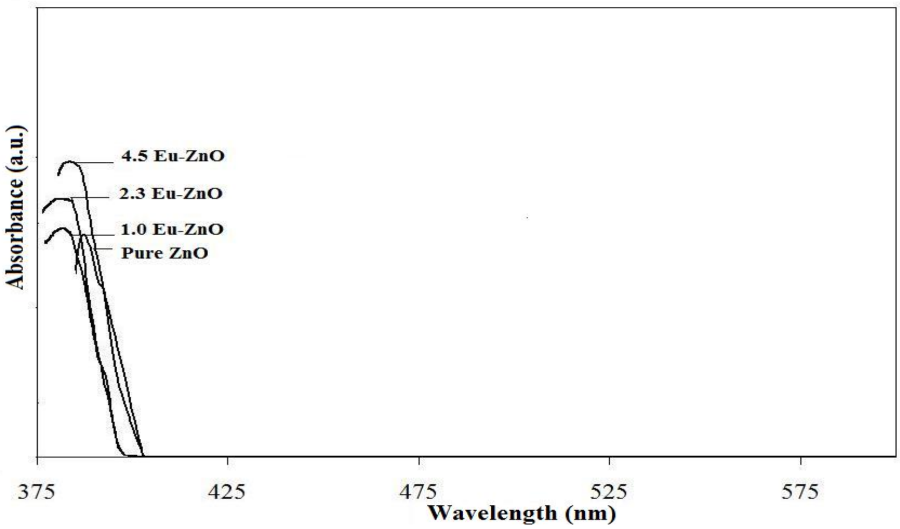

Figure 4.27. UV-vis diffuse reflectance spectra of pure ZnO and different amount Eu loaded ZnO

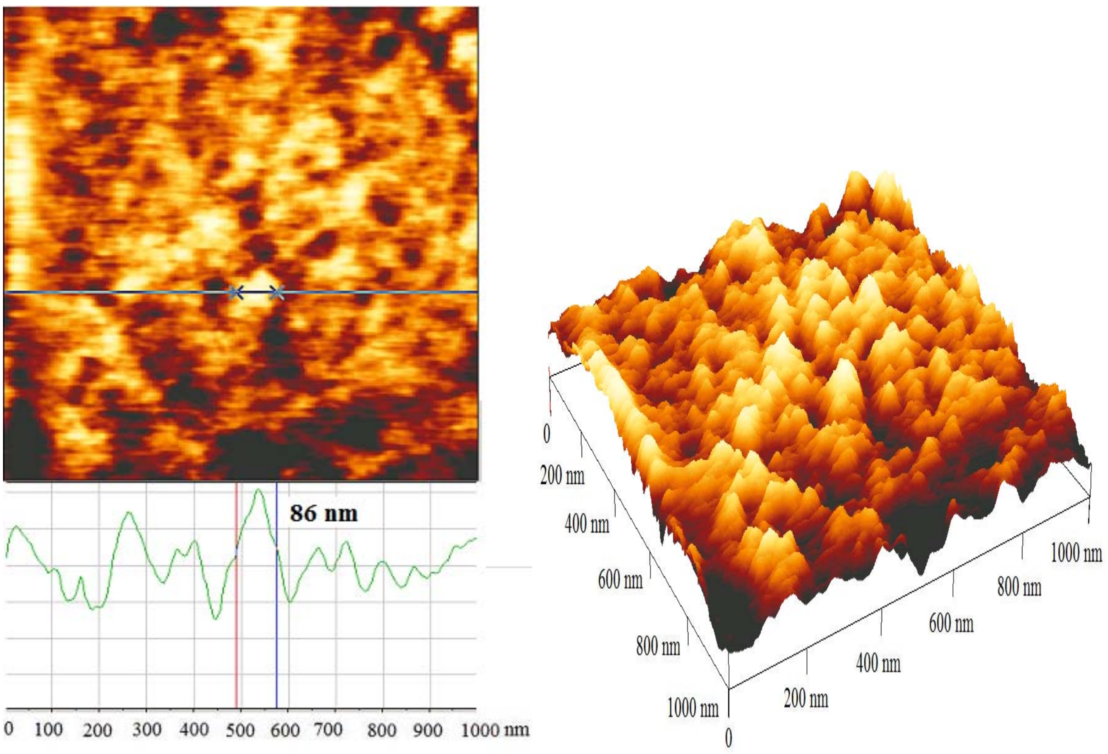

A) Two-dimensional (top-view) image (B) Three-dimensional

Figure 4.28. (A) Two-dimensional (top-view) image and (B) Three-dimensional AFM images of 2.3 Eu-ZnO

4.1.7. Characterization of Gadolinum (Gd) Loaded ZnO

<u>4.1.7.1. X-ray Diffraction (XRD) Analysis.</u> The XRD spectras of 1.0 Gd-ZnO, 2.3 Gd-ZnO catalysts did not show any additional peaks. However, additional diffractions due to the presence of Gd_2O_3 phase were observed in the XRD pattern of 4.5 Gd-ZnO catalyst at 400, 600, 800 and 1000˚C meaning that calcination temperature enhanced the formation of Gd_2O_3 crystals.

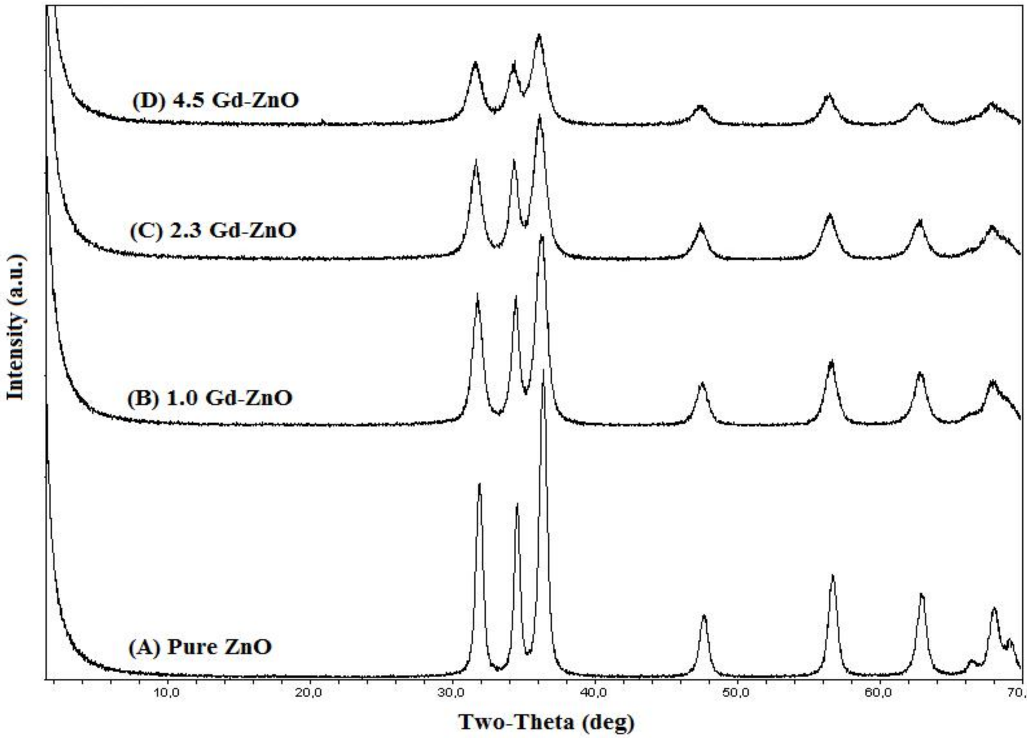

Figure 4.29. XRD patterns of pure ZnO and different content of Gd loaded ZnO catalysts

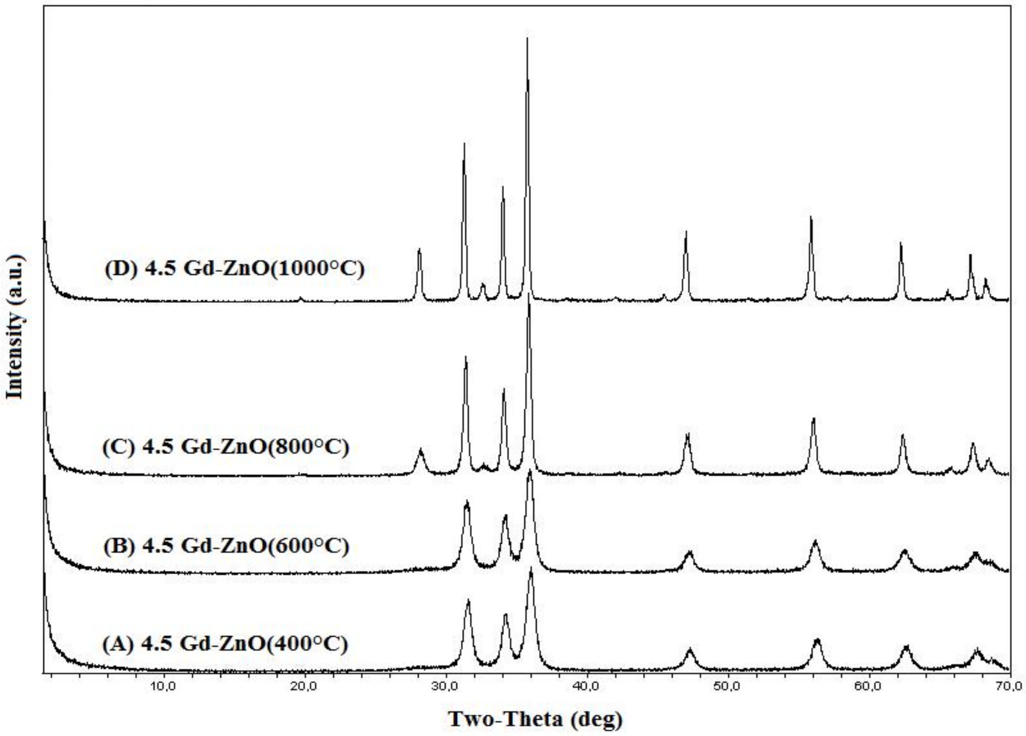

Figure 4.30. XRD patterns of 4.5 Gd-ZnO catalyst calcined at different temperatures

Table 4.12. FWHM and crystal size values of Gd loaded ZnO

Catalyst						
		ZnO			Gd_2O_3	
	Plane	FWHM	D(nm)	Plane	FWHM	D (nm)
1.0 Gd-ZnO (400°C)	101	0.739	12.5	-	-	-
2.3 Gd-ZnO (400°C)	101	0.727	11.5	-	-	-
4.5 Gd-ZnO (400°C)	101	0.777	10.7	-	-	-
		ZnO			Gd_2O_3	
	Plane	FWHM	D(nm)	Plane	FWHM	D (nm)
4.5 Gd-ZnO (600°C)	101	0.585	14.8	-	-	-
4.5 Gd-ZnO (800°C)	101	0.349	24.0	111	0.470	17.4
4.5 Gd-ZnO (1000°C)	101	0.219	38.1	111	0.293	27.9

4.1.7.2. BET Analysis. The values for the specific surface area of 4.5, 2.3 and 1.0 Gd - ZnO catalysts are obtained as 57.88, 80.75 and 98.84 m^2/g by multi point BET analysis, respectively. It is observed that there is a slight difference between the pore volume and pore size values of the pure ZnO and Gd^{3+} loaded ZnO catalyst. Besides, pore sizes of the catalysts are very small with respect to the crystal sizes of Gd_2O_3 particles, indicating distribution of Gd_2O_3 particles on the surface of the catalysts.

Table 4.13. Surface area, pore volume and pore size values of Gd loaded ZnO

Catalyst	BET (m^2/g)	Pore volume (cm^3/g)	Pore Size (nm)
Pure ZnO	59.46	0.028	3.5
1.0 Gd-ZnO	98.84	0.047	3.8
2.3 Gd-ZnO	80.75	0.038	3.1
4.5 Gd-ZnO	57.88	0.027	3.2

4.1.7.3. Scanning Electron Microscopy (SEM) Analysis. The SEM image in Figure 4.31 shows relatively thinner bunches of rodlike shaped particles of the 2.3 Gd-ZnO. The EDX analysis of 2.3 Gd-ZnO catalyst showed zinc, oxygen and gadolinum peaks (Figure 4.31 inset).

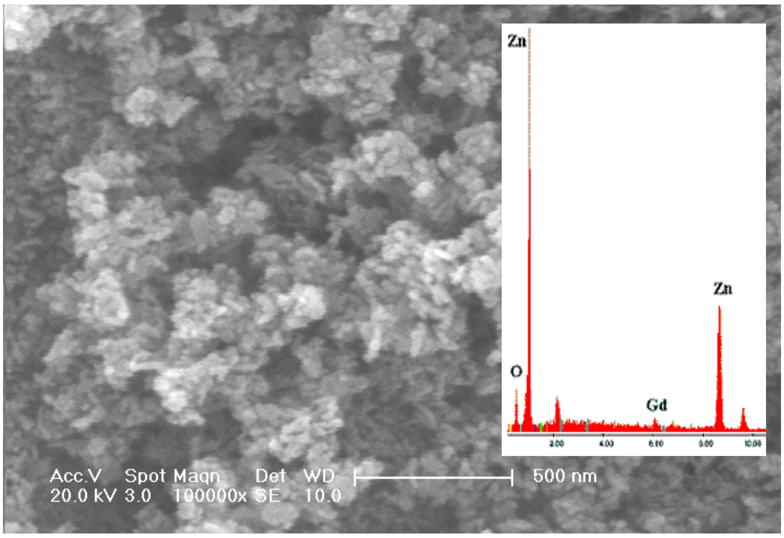

Figure 4.31. SEM image of 2.3 Gd-ZnO. Inset: EDX spectrum of the whole surface

4.1.7.4. Atomic Force Microscopy (AFM) Analysis. The three-dimensional (3-D) AFM image of 2.3 Gd-ZnO is shown in Figure 4.33 B. The corresponding AFM image showed rodlike ZnO nanoparticles with uniform size. Average roughness value (R_a) of 0.2451 nm is obtained and a particle with 52 nm diameter is labeled as an example in the distribution plot.

4.1.7.5. Diffuse Reflectance Spectrocopy (DRS) Analysis

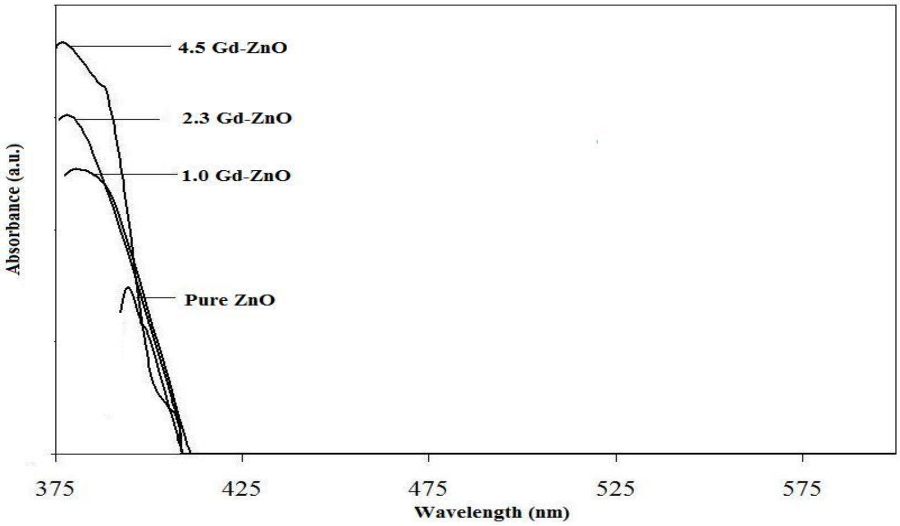

Figure 4.32. UV-vis diffuse reflectance spectra of pure ZnO and different amount Gd loaded ZnO

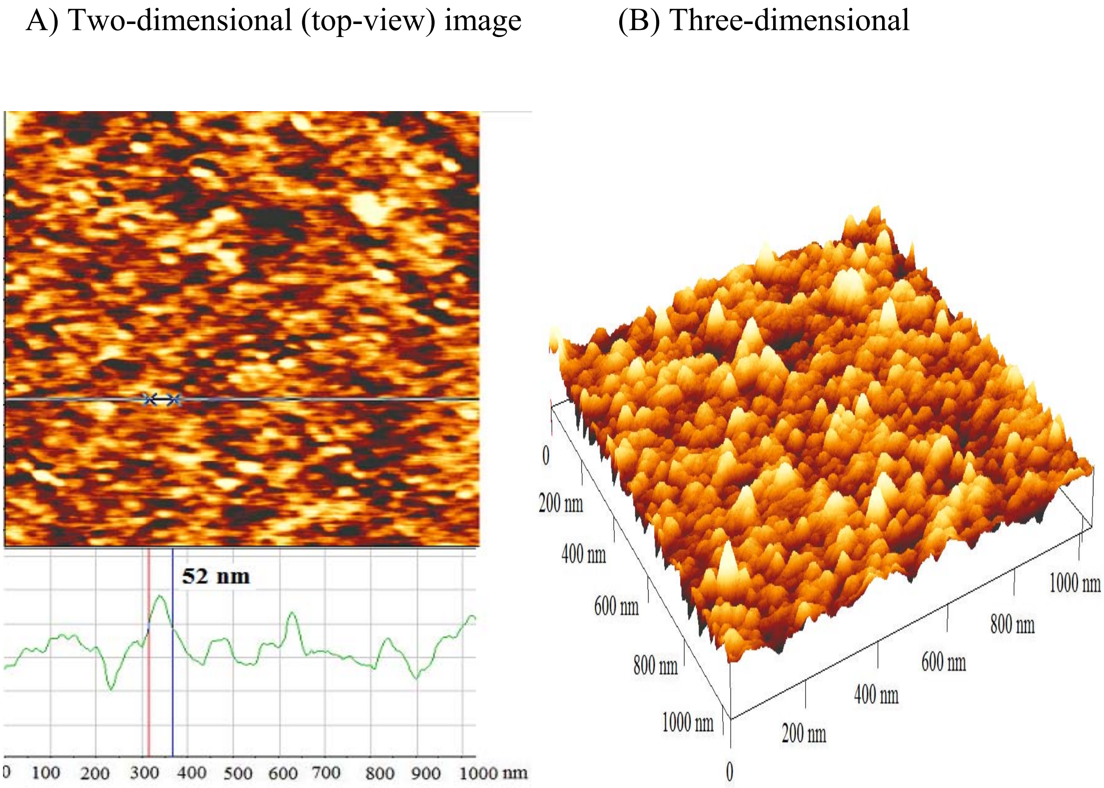

A) Two-dimensional (top-view) image (B) Three-dimensional

Figure 4.33. (A) Two-dimensional (top-view) image and (B) Three-dimensional AFM images of 2.3 Gd-ZnO

4.1.8. Characterization of Holmium (Ho) Loaded ZnO

4.1.8.1. X-ray Diffraction (XRD) Analysis. The XRD spectras of 1.0 Ho-ZnO, 2.3 Ho-ZnO and 4.5 Ho-ZnO catalysts did not show any additional peaks. However, additional diffractions due to the presence of Ho_2O_3 phase were observed in the XRD pattern of at 600, 800 and 1000˚C meaning that calcination temperature enhanced the formation of Ho_2O_3 crystals.

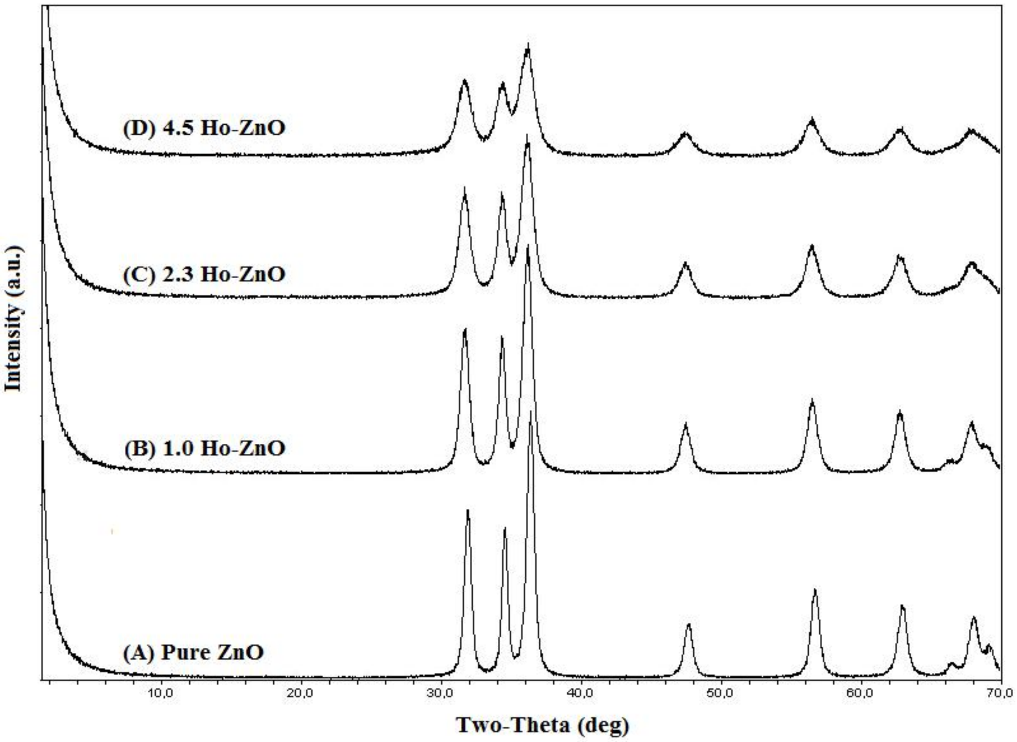

Figure 4.34. XRD patterns of pure ZnO and different content of Ho loaded ZnO catalysts

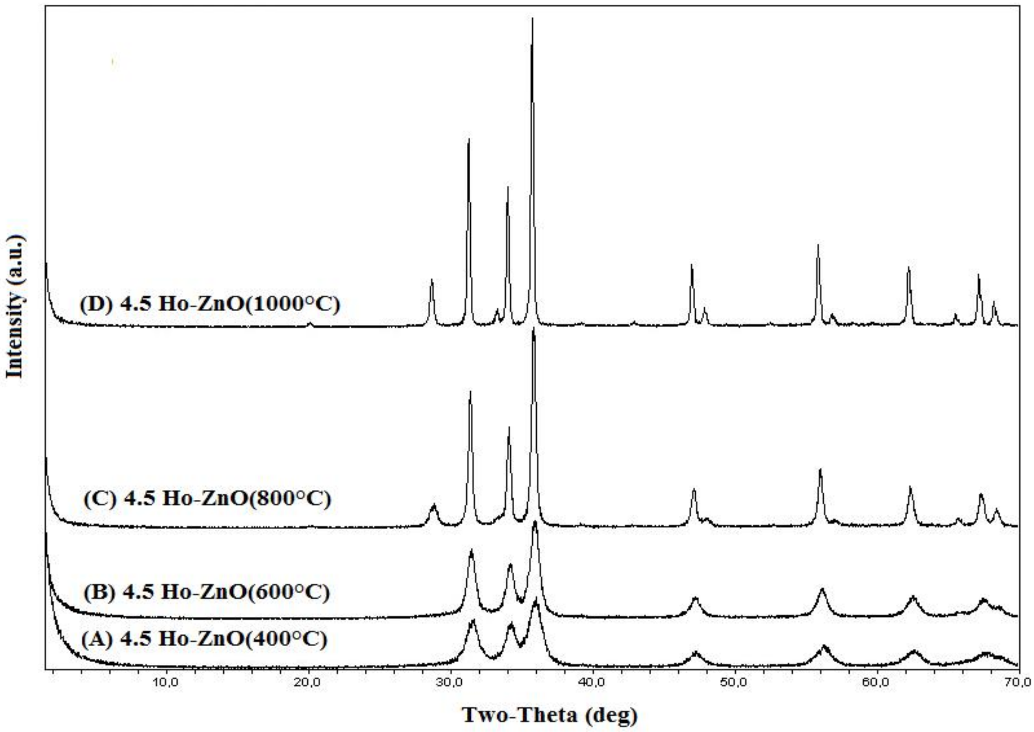

Figure 4.35. XRD patterns of 4.5 Ho-ZnO catalyst calcined at different temperatures

Table 4.14. FWHM and crystal size values of Ho loaded ZnO

Catalyst						
		ZnO			Ho_2O_3	
	Plane	FWHM	D(nm)	Plane	FWHM	D (nm)
1.0 Ho-ZnO (400˚C)	101	0.662	12.6	-	-	-
2.3 Ho-ZnO (400˚C)	101	0.728	11.5	-	-	-
4.5 Ho-ZnO (400˚C)	101	0.713	11.7	-	-	-
	Plane	ZnO FWHM	D(nm)	Plane	Ho_2O_3 FWHM	D (nm)
4.5 Ho-ZnO (600˚C)	101	0.536	15.6	-	-	-
4.5 Ho-ZnO (800˚C)	101	0.349	24.0	222	0.505	16.2
4.5 Ho-ZnO (1000˚C)	101	0.216	38.7	222	0.294	27.9

4.1.8.2. BET Analysis. The values for the specific surface area of 4.5, 2.3 and 1.0 Ho-ZnO catalysts are obtained as 95.6, 76.78 and 76.04 m^2/g by multi point BET analysis, respectively. It is observed that there is a slight difference between the pore volume and pore size values of the pure ZnO and Ho^{3+} loaded ZnO catalyst. Besides, pore sizes of the catalysts are very small with respect to the crystal sizes of Ho_2O_3 particles, indicating distribution of Ho_2O_3 particles on the surface of the catalysts.

Table 4.15. Surface area, pore volume and pore size values of Ho loaded ZnO

Catalyst	BET (m^2/g)	Pore volume (cm^3/g)	Pore Size (nm)
Pure ZnO	59.46	0.028	3.5
1.0 Ho-ZnO	76.04	0.035	3.1
2.3 Ho-ZnO	76.78	0.035	3.1
4.5 Ho-ZnO	95.6	0.044	3.0

4.1.8.3. Scanning Electron Microscopy (SEM) Analysis. The SEM image in Figure 4.36 shows bunches of rodlike shaped particles of the 2.3 Ho-ZnO. The EDX analysis of the 2.3 Ho-ZnO catalyst showed zinc, oxygen and holmium peaks (Figure 4.36 inset).

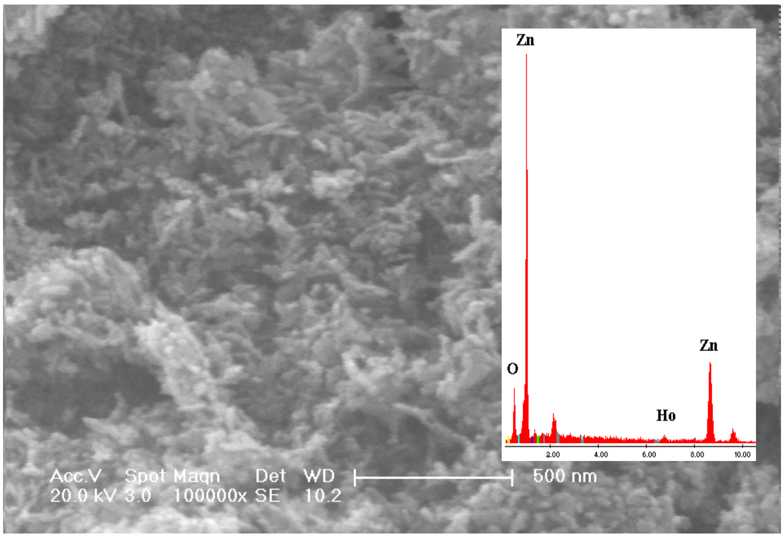

Figure 4.36. SEM image of 2.3 Ho-ZnO. Inset: EDX spectrum of the whole surface

4.1.8.4. Atomic Force Microscopy (AFM) Analysis. The three-dimensional (3-D) AFM image of 2.3 Ho-ZnO showing uniformly distributed is shown in Figure 4.38 B. Average roughness value (R_a) of 0.1380 nm is obtained and a particle with 35 nm diameter is labeled as an example in the distribution plot.

4.1.8.5. Diffuse Reflectance Spectrocopy (DRS) Analysis

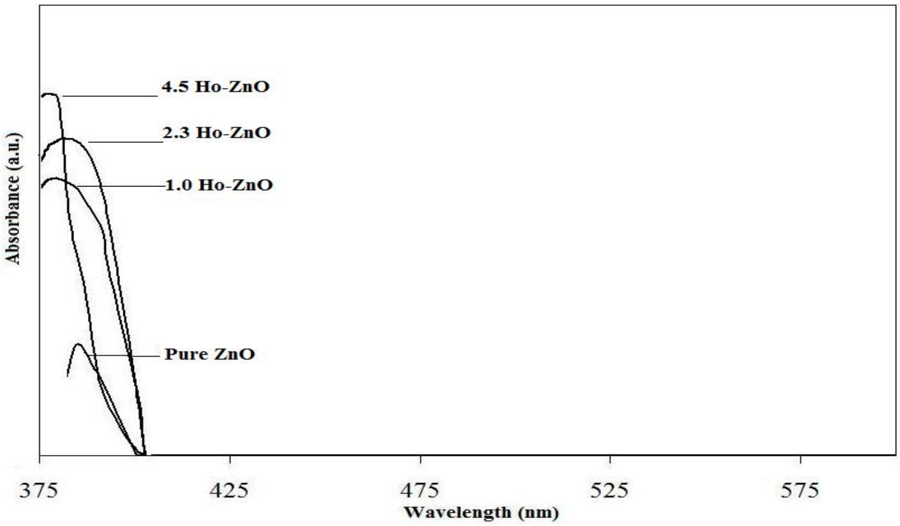

Figure 4.37. UV-vis diffuse reflectance spectra of pure ZnO and different amount Ho loaded ZnO

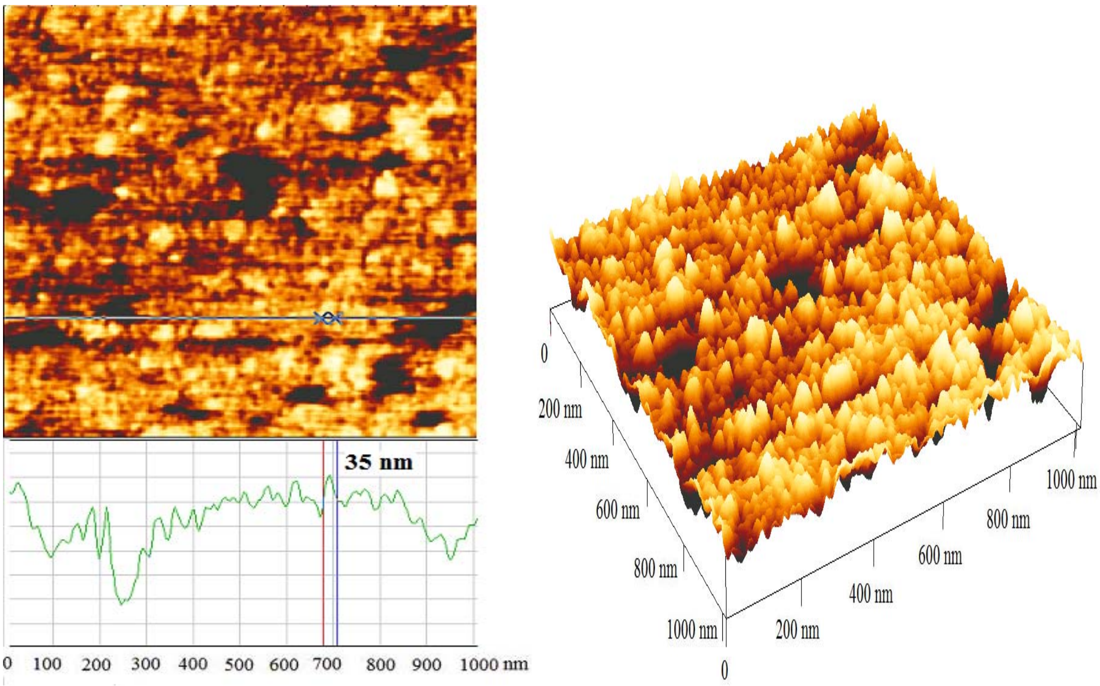

A) Two-dimensional (top-view) image

(B) Three-dimensional

Figure 4.38. (A) Two-dimensional (top-view) image and (B) Three-dimensional AFM images of 2.3 Ho-ZnO

4.2. Photolytic Decolorization of MO

The photolytic decolorization process was followed at different initial concentrations of MO; 16.34 mg/L, 8.17 mg/L and 3.27 mg/L about 90 min irradiation time at 464 nm (Figure 4.39). For each of these concentrations, the amount of MO remaining in solution did not exhibit a significant variation. Thus, it was concluded that in the absence of catalysts, MO decolorization was negligible. The inset in Figure 4.39 represents UV-Vis spectrum of 3.27 mg/L sample.

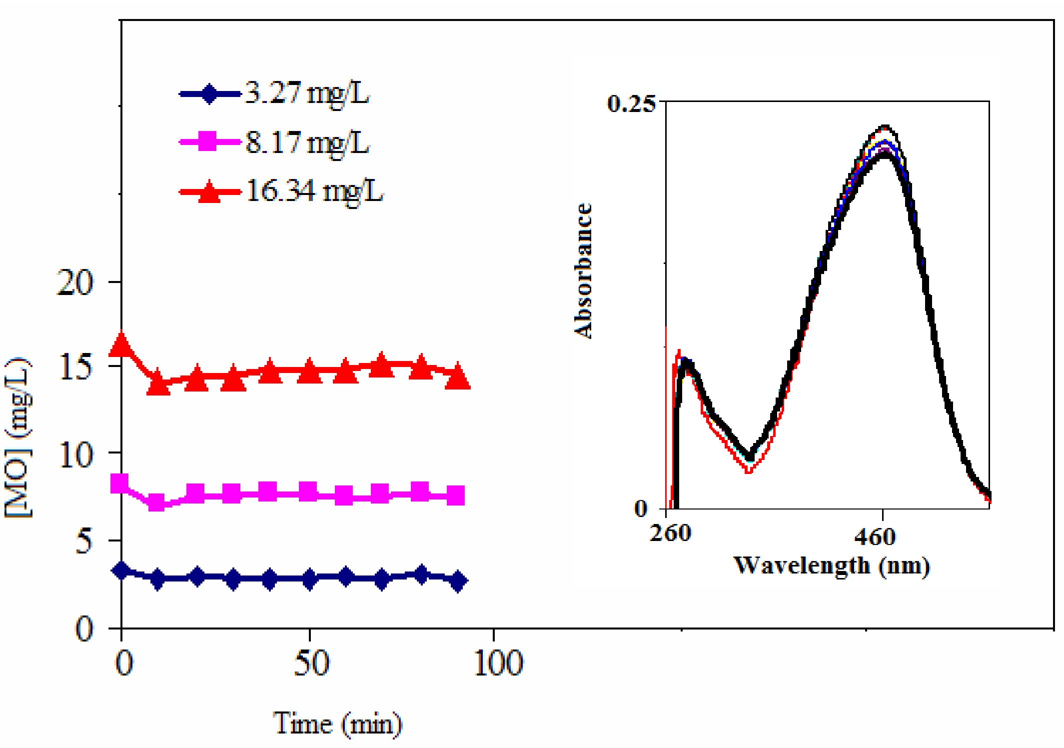

Figure 4.39. Photolytic decolorization of MO at different concentrations. Inset: UV-Vis spectrum of 3.27 mg/L sample. Conditions: pH= 5.85 (Natural), I= 4.7x10^{15} photons/s, T=298 K

4.3. Contact Angle Measurements

Contact angle measurements were performed to understand whether as-prepared catalysts induced hydrophilic or hydrophobic characters. Experiments were conducted at two steps; in the first step, a known concentration of catalysts was well-dispersed in water and then, dip coated on glass-substrates. The obtained films were dried at room temperature and then calcined at 500°C with a heating rate of 10°C min^{-1} for 5 h. The contact angles were detected as 37.01°, 42.13°, 46.88° and 55.33° for pure ZnO, 1.0 Metal-ZnO, 2.3 Metal-ZnO and 4.5 Metal-ZnO, respectively (Table 4.16). Since these numerical values indicate hydrophilicity, the resulting films are also accepted as hydrophilic [54]. Besides, pure ZnO catalyst showed the most hydrophilic character. As the content of metal ion increased in the final catalyst configuration, the contact angles were found to increase. This reveals a kind of variation in the hydrophilic nature of the catalysts. However, such increments in the contact angles still do not exhibit formation of a hydrophobic surface. Generation of oxygen deficient sites throughout the formation processes of the films may lead to the adsorption of water molecules for the occupation of these vacancies. This, finally, produces more OH groups on the surface of the catalysts and creates a hydrophilic surface. On the other hand, in the presence of metal ion loaded samples, the number of such vacancies is limited owing to the already existing metal ions or their oxide forms and their inhibition effect for the formation of deficiencies in the crystal structure.

In the second step, following the same experimental procedures, films were irradiated with the same irradiation source used in all photocatalytic degradation experiments about one hour. The decrements noticed in the contact angles after irradiation indicate an increase in the hydrophilicity of all samples (Table 4.16). The synergetic effect of photocatalysis and hydrophilicity can be understood as; because more OH groups can be adsorbed on the surface due to hydrophilicity, the photocatalytic activity is enhanced. So, hydrophilicity can increase photoactivity [54].

Table 4.16. Contact angles of the films

Catalyst	Before Irradiation	After Irradiation
Pure ZnO	37.01°	15.01°
1.0 Metal-ZnO	42.13°	24.58°
2.3 Metal-ZnO	46.88°	22.73°
4.5 Metal-ZnO	55.33°	25.16°

4.4. Comparison of Photocatalytic Activities: TiO_2 (Alrich), TiO_2 (Merck), ZnO (Merck), Pure ZnO, La-ZnO

As already mentioned, ZnO was used as an alternative photocatalyst to TiO_2 in this study. With this purpose, prior to the details of the experiments performed in the presence of ZnO-based catalysts, two sets of preliminary experiments were designed. In the first set, TiO_2 catalysts with surface areas (~8-10 m^2/g) similar to that of commercial ZnO (~10 m^2/g-Merck) were selected. The activities of these catalysts were compared with the activities of commercial ZnO, synthesized ZnO (pure ZnO) and also La loaded ZnO (1.0 La-ZnO) (Figure 4.40). In contrast to the TiO_2 catalysts, ZnO (commercial), pure ZnO and 1.0 La-ZnO catalysts exhibited higher decolorization percentages of MO. In the second set of experiments, dark adsorption capacities of pure ZnO and 1.0 La-ZnO catalysts were controlled (Figure 4.40 inset). 1.0 La-ZnO catalyst revealed a better adsorption ability in comparison to pure ZnO. The following sections will focus on the photocatalytic performances of pure ZnO and rare earth metal ion loaded ZnO catalysts in detail.

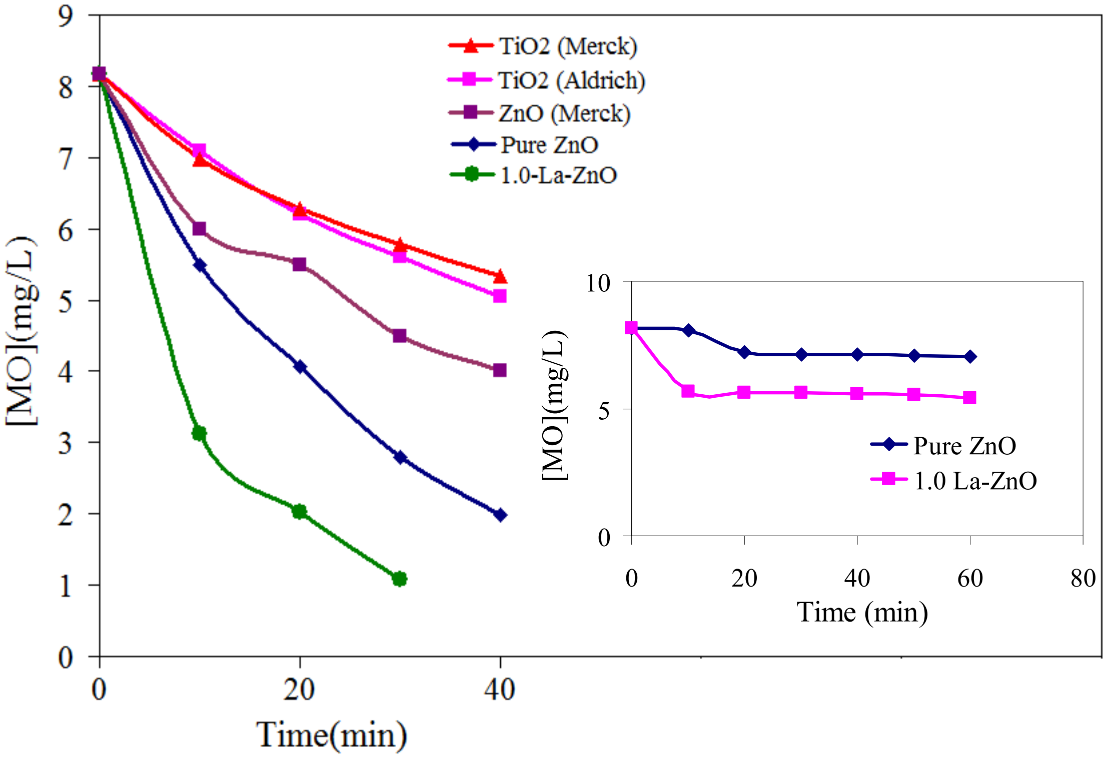

Figure 4.40. Results of preliminary experiments. Inset: Dark adsorption capacities of pure ZnO and 1.0 La-ZnO

4.5. Photocatalytic Decolorization of MO in the Presence of Pure ZnO

4.5.1. Effect of MO concentration

The influence of initial MO concentration on the degree of photodecolorization was studied in the range of 3.27-32.68 mg/L with pure ZnO (Figure 4.41). It was found that decolorization rate was inversely related to the dye concentration. High concentration of MO molecules may block the photocatalytically active centers on the surface of the catalyst, inhibit the adsorption of OH^- ions and increase the amount of MO remaining in solution. Furthermore, as MO concentration increased, photons of the light get intercepted before reaching the catalyst surface and hence, resulting in a decrease in adsorption of photons by the catalyst.

Photodecolorization experiments of MO exhibited pseudo-first order kinetics with respect to the concentration of the dye and the rate expression was given in equation (4.1).

$$\text{Rate} = \frac{-dC}{dt} = k_{app}C \qquad (4.1)$$

where k_{app} was the apparent rate constant. The integration of the equation yielded equation (4.2):

$$\ln\left(\frac{C_0}{C}\right) = k_{app}t \qquad (4.2)$$

where C_0 was the equilibrium concentration of MO after dark adsorption, C was the remaining concentration in solution by time and k_{app} was the apparent rate constant. Figure 4.42 shows the natural log of the ratio of the initial MO concentration to the concentration at given irradiation times. Pseudo-first order kinetics was proved by the linearity obtained for all concentrations. Calculated apparent rate-constants (slopes of the lines) and regression values were shown in Table 4.17.

Table 4.17. Apparent first order rate constants (k_{app}) for the photocatalytic decolorization of MO at different initial concentrations and linear regression values

$[MO]_0$ (mg/L)	k_{app} (min^{-1})	R
32.68	0.0206	0.9754
16.34	0.0255	0.9833
8.17	0.0358	0.9969
3.27	0.0518	0.9990

Also, the linear plot obtained by plotting the reciprocal of 1/Rate against $1/C_0$ (Figure 4.42 Inset), showed the applicability of Langmuir-Hinshelwood model for the photocatalytic decolorization of MO. Accordingly, adsorption rate constant (K) and reaction rate constant (k_r) were calculated as 0.085 $mg^{-1}L$ and 0.765 mg/L min, respectively.

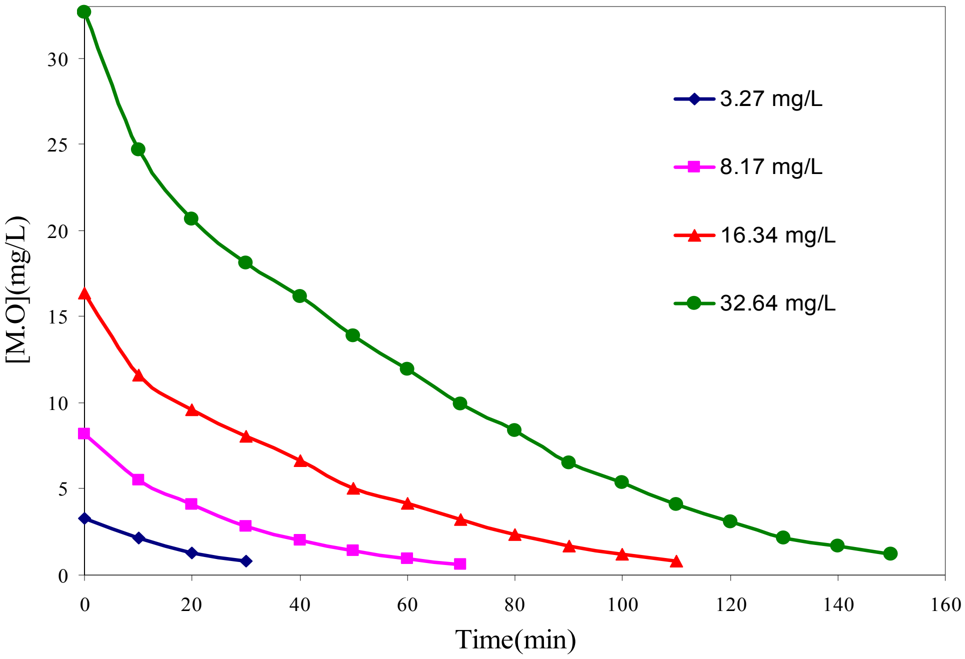

Figure 4.41. Photodecolorization of MO in the presence of pure ZnO at different initial MO concentrations. Conditions: pH= 5.85 (Natural), I= $4.7x10^{15}$ photons/s, T=298 K

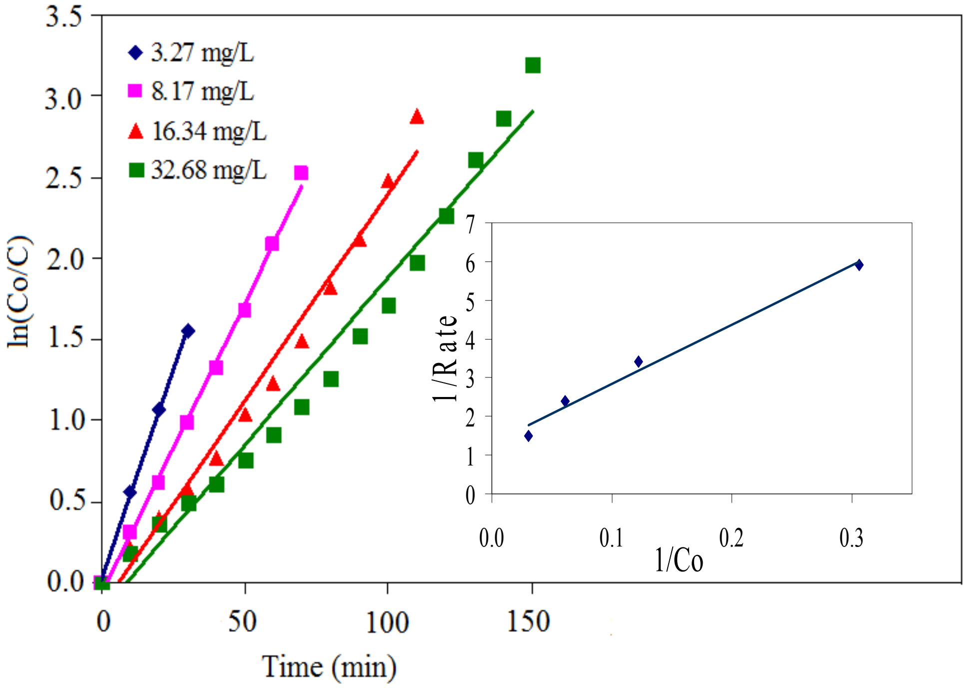

Figure 4.42. ln (C_o/C) vs. time plot in the presence of pure ZnO. Conditions: pH= 5.85 (Natural), I= 4.7x10^{15} photons/s, T=298 K.

Inset: 1/Rate vs. 1/C_o plot in the presence of pure ZnO

4.5.2. Effect of catalyst loading

The effect of catalyst loading on the decolorization of MO was investigated using pure ZnO from 0.1 g to 0.4 g under 40 min irradiation time (Figure 4.43). At higher loading levels, while agglomeration of particles increases, the availability of active sites and the penetration of UV light into the suspension decrease. Hence, 0.1 g of catalyst loading was selected throughout the experiments including metal loaded ZnO catalysts.

4.5.3. Effect of pH

The solution pH is one of the important parameters in reactions taking place on the semiconductor surfaces [55]. Generally, the effect of pH is related to the establishment of acid-base equilibria on the catalyst surface and there is a strong dependence on the pH of zero point-charge (pH_{zpc}) of the semiconductors. The pH_{zpc} value of ZnO is known as 9.0

[26]. Accordingly, the surface of ZnO is either positively or negatively charged depending on the pH of the reaction medium (Equation 4.3 and 4.4).

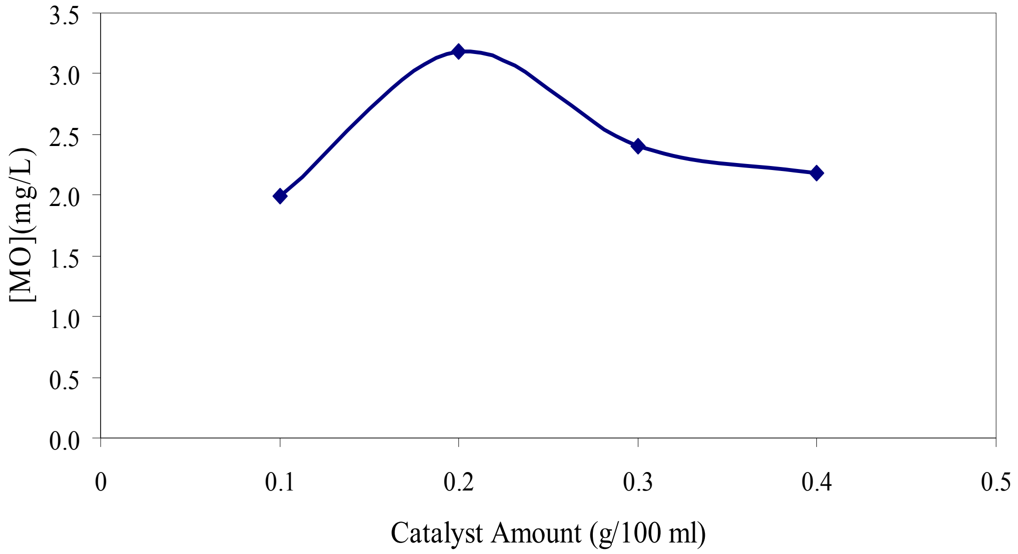

Figure 4.43. Effect of catalyst loading for the photocatalytic decolorization of MO. Conditions: pH= 5.85 (Natural), [MO]= 8.17 mg/L, Irradiation Time= 40 min, I= 4.7×10^{15} photons/s, T=298 K, Flow rate= 2000 rpm

at $pH<pH_{zpc}$: $ZnOH_2^+ \leftrightarrow Zn\text{-}OH + H^+$ (4.3)

at $pH>pH_{zpc}$: $Zn\text{-}OH + OH^- \leftrightarrow ZnO^- + H_2O$ (4.4)

Thus; at $pH<pH_{zpc}$, attractive forces are dominant between the ZnO surface and the dye. This favors adsorption of MO molecules on the catalyst surface, since MO is negatively charged above pH 5.8 (natural pH) whereas the catalyst is positively charged below 9.0. On the contrary, at $pH>pH_{zpc}$, ZnO surface is negatively charged and repulsive forces between the ZnO surface and the dye lead to a lower adsorption. Moreover, competition between MO and OH^- ions decreases the photocatalytic activity at higher pH values.

Based on the resulting line equations in Figure 3.4, the remaining concentration values of MO were calculated in the experiments performed at different pH values under one hour irradiation (Figure 4.44). The lowest amount of MO remained in solution was obtained at pH 8, indicating the highest activity of the pure ZnO catalyst. This was followed with the natural pH value (5.85). At pH 10, the fight between MO molecules and OH^- ions increased the remaining MO amount in the solution. According to Equation 4.3, the least MO concentration was expected in solution at pH 2. However, an obvious increase was noticed in the MO concentration at pH 2 owing to the photocorrosion of ZnO through self-oxidation at low pH values (Equation 4.5) [26].

$$ZnO + 2h^+ \rightarrow Zn^{2+} + \tfrac{1}{2} O_2 \tag{4.5}$$

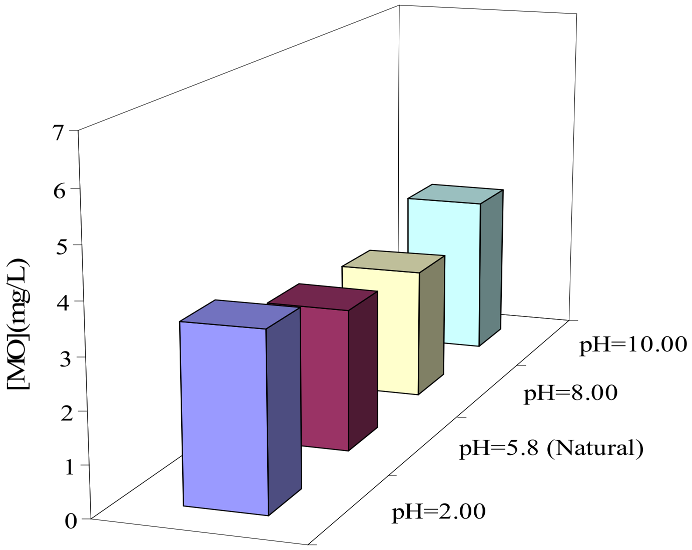

Figure 4.44. [MO] remaining in the solution (mg/L) after photodecolorization in the presence of pure ZnO at different pH values. Conditions: [MO]= 8.17 mg/L, I= $4.7x10^{15}$ photons/s, T=298 K

4.6. Photocatalytic Decolorization of MO in the Presence of La loaded ZnO

4.6.1. Effect of La^{3+} ion content

The presence of dissolved metal ions effect the efficiency of photocatalytic reactions. An optimum loading of La^{3+} ion is required to enhance the potential difference between surface and the center of the particles to separate photoinduced electron-hole pairs. The effect of content of metal ion is shown in Figure 4.45. It is found that the optimum value of La^{3+} ion loading is 1.00 per cent which means 1.0 La-ZnO catalyst is more efficient for separating photoinduced electron-hole pairs. However when the content of loading ion is excessively high, the space charge region becomes very narrow and covers the most of the ZnO surface that inhibit the direct exposure of UV light on the surface of the catalyst. Hence, excitation of electron from valence band to conduction band is limited and increased the recombination of photoinduced electron-hole pairs.

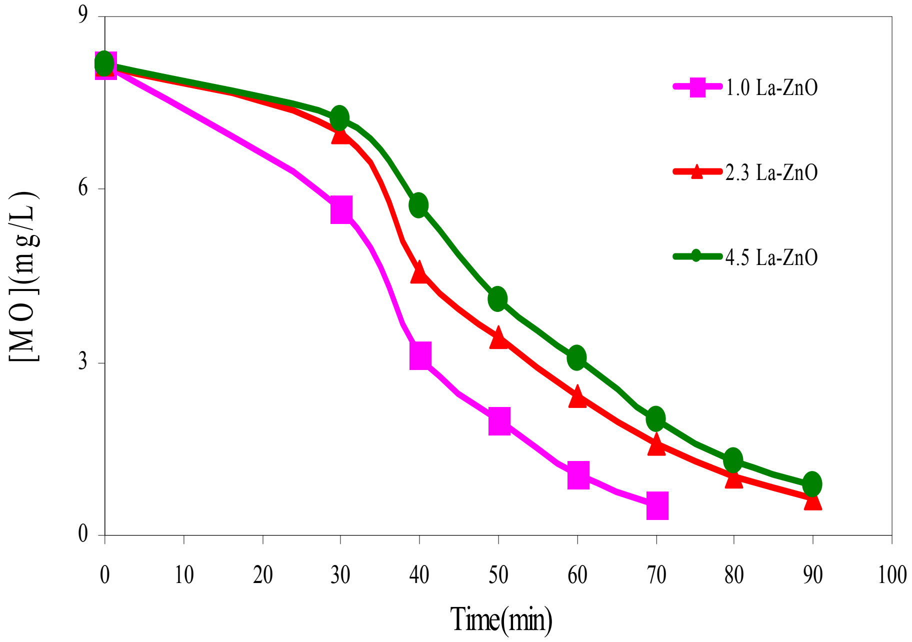

Figure 4.45. Effect of La loading on ZnO for the photocatalytic decolorization of MO. Conditions: pH= 5.85 (Natural), [MO]= 8.17 mg/L, I= $4.7x10^{15}$ photons/s, T=298 K

4.6.2. Effect of MO Concentration

The effect of initial dye concentration was investigated over a range of 3.27- 32.68 mg/L also in the presence of 1.0 La-ZnO (Figure 4.46). It is showed that decolorization rate is inversely related to the dye concentration due to less photocatalytically active centers and light scattering effect. Furthermore, photodecolorization experiments of MO by UV/ 1.0 La-ZnO process exhibited pseudo-first order kinetics, too. In Figure 4.47 linearity is noticed which proves that reactions followed pseudo-first order kinetics. Calculated apparent rate-constants (slopes of the lines) and regression values are shown in Table 4.18.

For 1.0 La-ZnO catalyst, adsorption rate constants (K) and reaction rate constants (k_r) are also calculated as 0.156 $mg^{-1}L$ and 0.634 mg/L min, respectively.

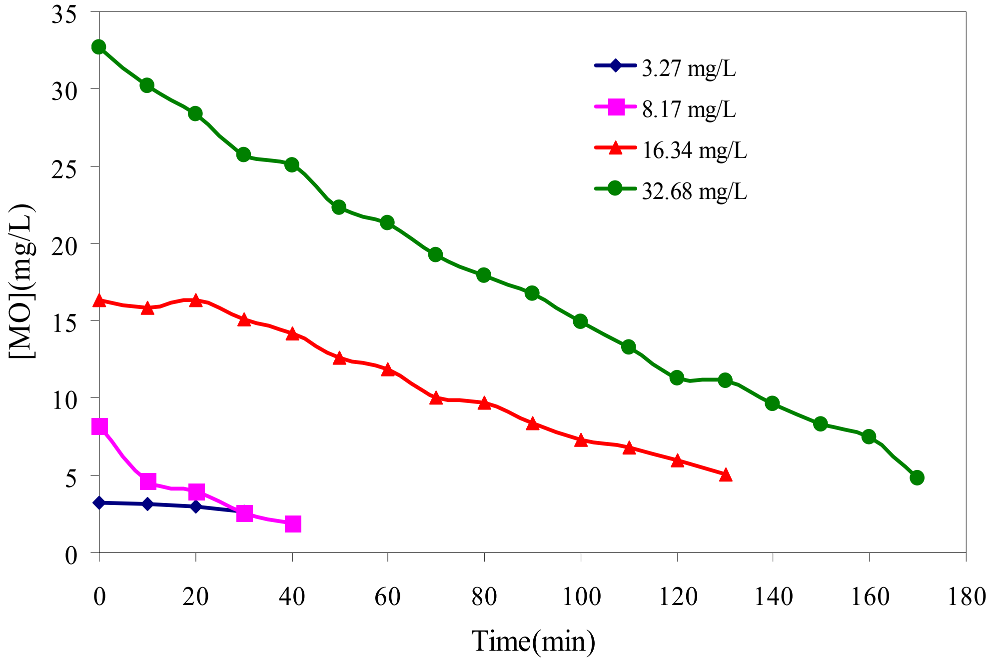

Figure 4.46. Photodecolorization of MO in the presence of 1.0 La-ZnO at different initial MO concentrations. Conditions: pH= 5.85 (Natural), I= 4.7x10^{15} photons/s, T=298 K

Table 4.18. Apparent first order rate constants (k_{app}) for the photocatalytic decolorization of MO at different initial concentrations and linear regression values

$[MO]_0$ (mg/L)	k_{app} (min^{-1})	R
32.68	0.017	0.9841
16.34	0.022	0.9890
8.17	0.058	0.9940
3.27	0.063	0.9959

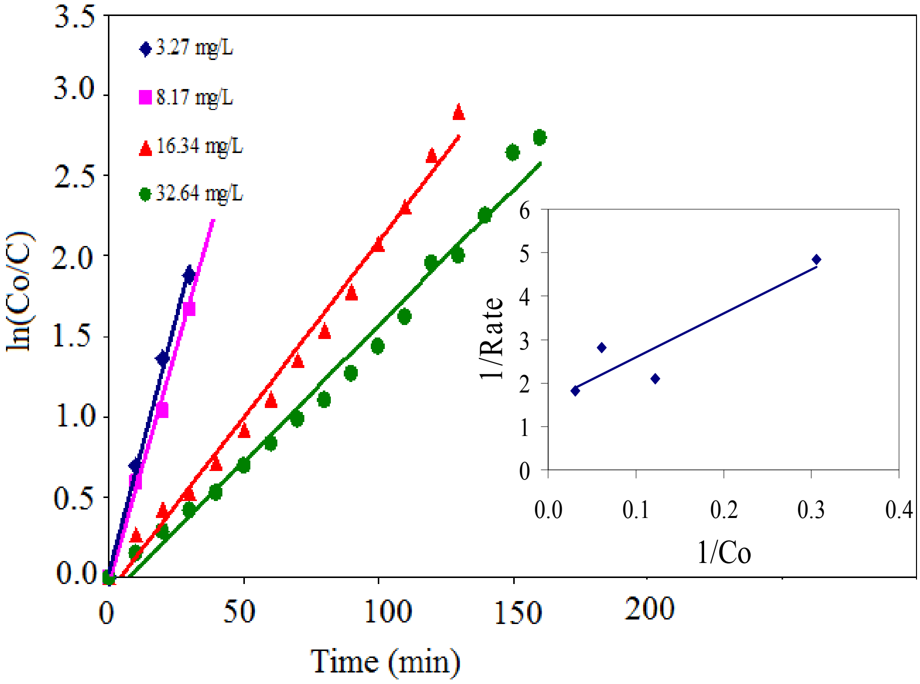

Figure 4.47. ln (C_o/C) vs. time plot in the presence of 1.0 La-ZnO. Conditions: pH= 5.85 (Natural), I= $4.7x10^{15}$ photons/s, T=298 K. Inset: 1/Rate vs. 1/C_o plot in the presence of 1.0 per cent La-ZnO

4.6.3. Effect of pH

In Figure 4.48, the degree of photodecolorization of MO with 1.0 La-ZnO at a fixed reaction time is shown in the pH range of 2.0-10.0. Almost the same trend is observed for 1.0 La-ZnO. At $pH<pH_{zpc}$, attractive forces between the catalyst surface and MO will favour adsorption whereas at pH>pHzpc, catalyst surface is negatively charged and repulsive forces between the catalyst surface and MO lead to a lower adsorption. Moreover, concentration of MO remaining in the solution (mg/L) after photodecolorization in the presence of 1.0 La-ZnO at pH=10.0 is higher than that of pure ZnO. This means La loading increased the competititon between MO and OH^- ions at pH 10 and inhibit the formation of hydroxyl radicals.

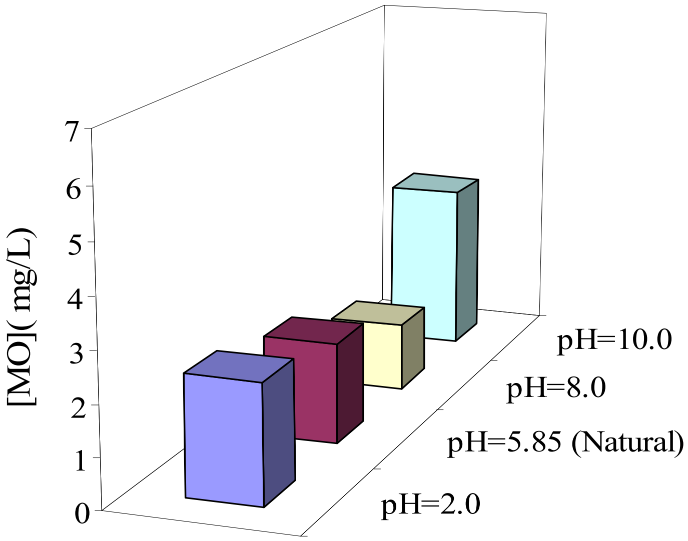

Figure 4.48. [MO] remaining in the solution (mg/L) after photodecolorization in the presence of 1.0 per cent La-ZnO at different pH values. Conditions: [MO] = 8.17 mg/L, I= 4.7×10^{15} photons/s, T=298 K

4.7. Photocatalytic Decolorization of MO in the Presence of Pr loaded ZnO

4.7.1. Effect of Pr^{3+} ion content

The effect of content of Pr^{3+} ion on decolorization of MO is shown in Figure 4.49. Optimum value of loading Pr^{3+} ion is 4.5 per cent to separate photoinduced electron-hole pairs by the large electric field before recombination which led to the higher photocatalytic activity.

4.7.2. Effect of MO Concentration

In the presence of 1.0 Pr-ZnO, the effect of initial dye concentration was investigated over a range of 3.27- 32.68 mg/L (Figure 4.50). It is showed that decolorization rate increases as the dye concentration decreases. Moreover, photodecolorization experiments of MO by UV/ 1.0 Pr-ZnO process exhibited pseudo-first order kinetics, too. In Figure 4.51 linearity is noticed which proves that reactions followed pseudo-first order kinetics. Calculated apparent rate-constants (slopes of the lines) and regression values are shown in

Table 4.19. For 1.0 Pr-ZnO catalyst, adsorption rate constants (K) and reaction rate constants (k_r) are also calculated as 0.129mg^{-1}L and 0.438 mg/L min, respectively.

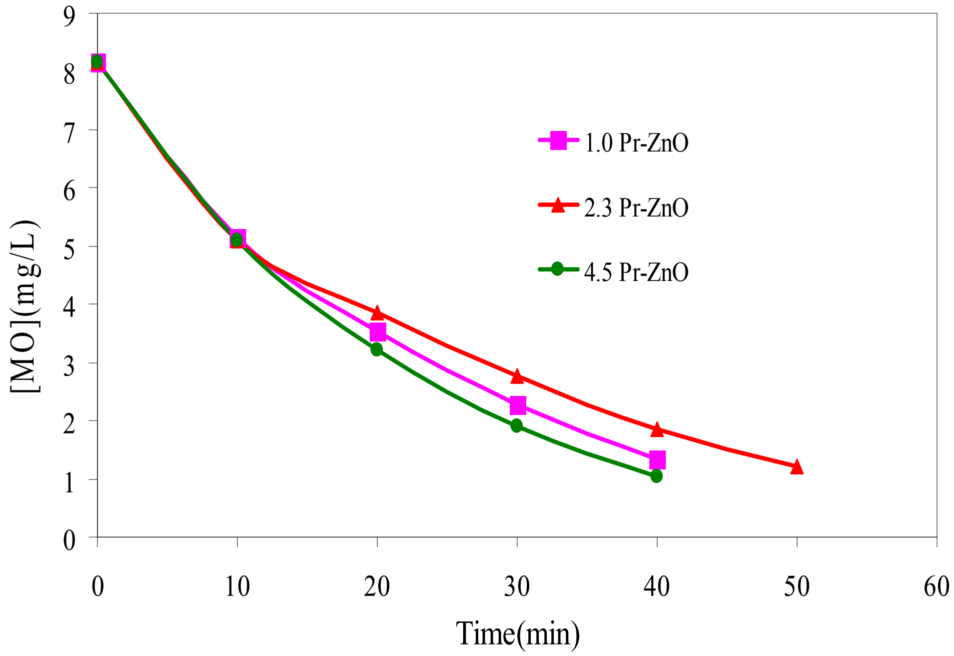

Figure 4.49. Effect of Pr loading on ZnO for the photocatalytic decolorization of MO. Conditions: pH= 5.85 (Natural), [MO]= 8.17 mg/L, I= 4.7x10^{15} photons/s, T=298 K

Table 4.19. Apparent first order rate constants (k_{app}) for the photocatalytic decolorization of MO at different initial concentrations and linear regression values

$[MO]_0$ (mg/L)	k_{app} (min^{-1})	R
32.68	0.007	0.9861
16.34	0.024	0.9936
8.17	0.034	0.9975
3.27	0.037	1.0

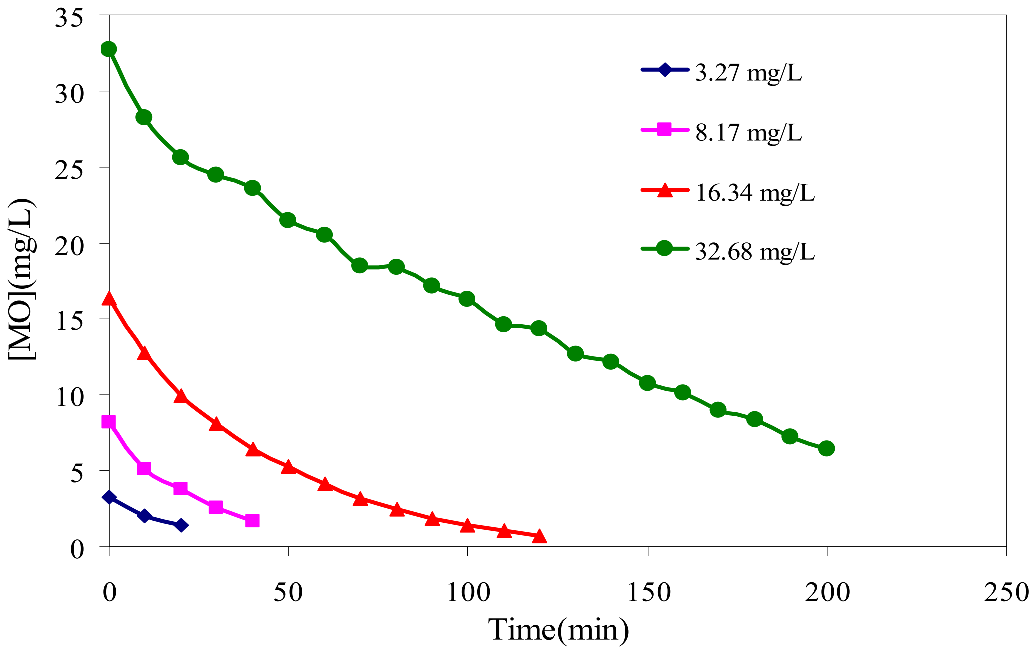

Figure 4.50. Photocolorization of MO in the presence of 1.0 Pr-ZnO at different initial MO concentrations. Conditions: pH= 5.85 (Natural), I= 4.7×10^{15} photons/s, T=298 K

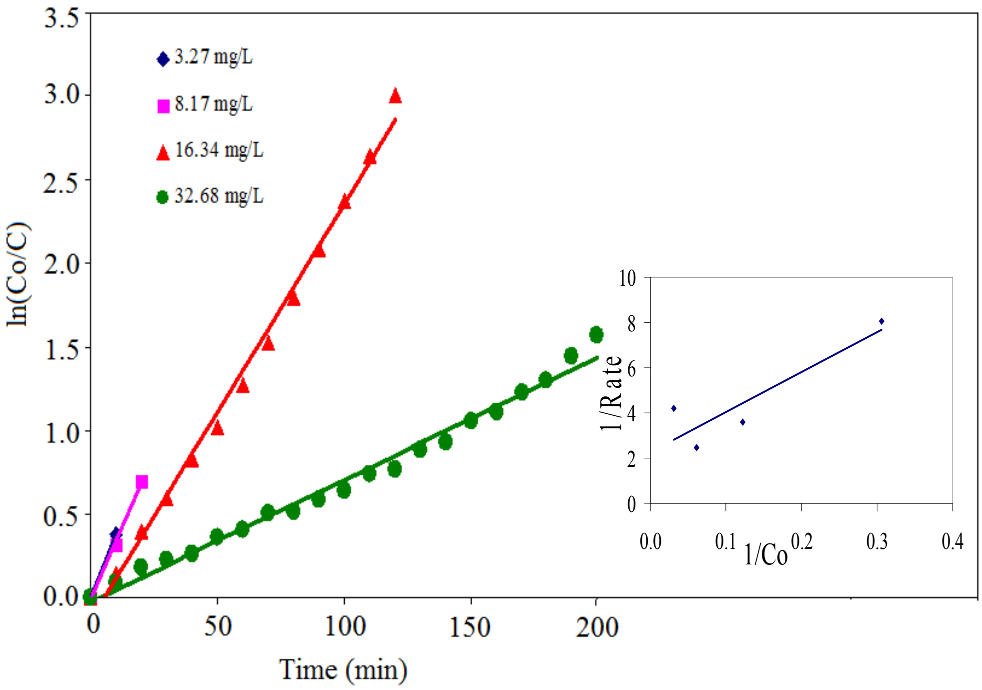

Figure 4.51. ln (C_o/C) vs. time plot in the presence of 1.0 Pr-ZnO. Conditions: pH= 5.85 (Natural), I= 4.7×10^{15} photons/s, T=298 K. Inset: 1/Rate vs. 1/C_o plot in the presence of 1.0 per cent Pr-ZnO

4.7.3. Effect of pH

In figure 4.52, the degree of photodecolorization of MO with 1.0 Pr-ZnO at a fixed reaction time is shown in the pH range of 2.0-10.0. The trend is a bit different for 1.0 Pr-ZnO than pure and 1.0 La-ZnO. It is observed that highest activity is obtained at pH 5.85 (natural pH) and lowest percentage is noticed at pH 2.

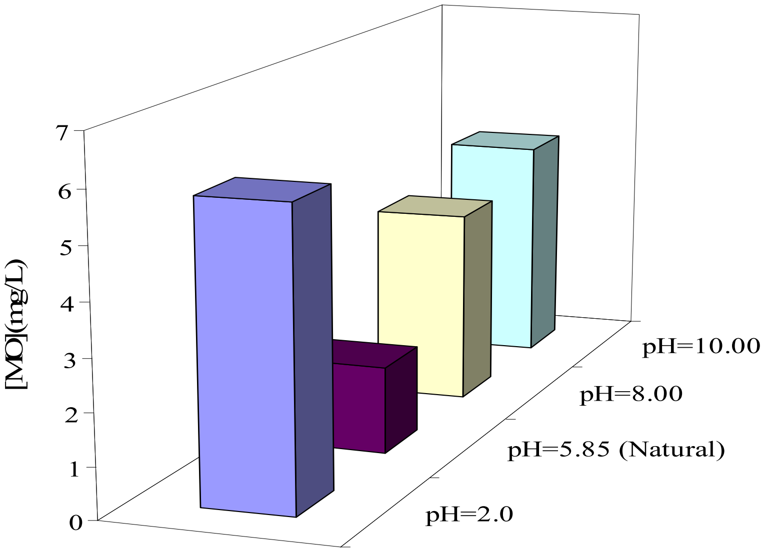

Figure 4.52. [MO] remaining in the solution (mg/L) after photodecolorization in the presence of 1.0 Pr-ZnO at different pH values. Conditions: [MO] = 8.17 mg/L, I= 4.7x1015 photons/s, T=298 K

4.8. Photocatalytic Decolorization of MO in the Presence of Nd loaded ZnO

4.8.1. Effect of Nd^{3+} ion content

The effect of content of Nd^{+3} ion on decolorization of MO is shown in Figure 4.53. 2.3 Nd-ZnO catalyst showed the highest photocatalytic performance. It is also observed that the crystal size of 2.3 Nd-ZnO is smaller than the 1.0 Nd-ZnO catalyst which indicates inhibition of crystal growth with an increase in metal ion content.

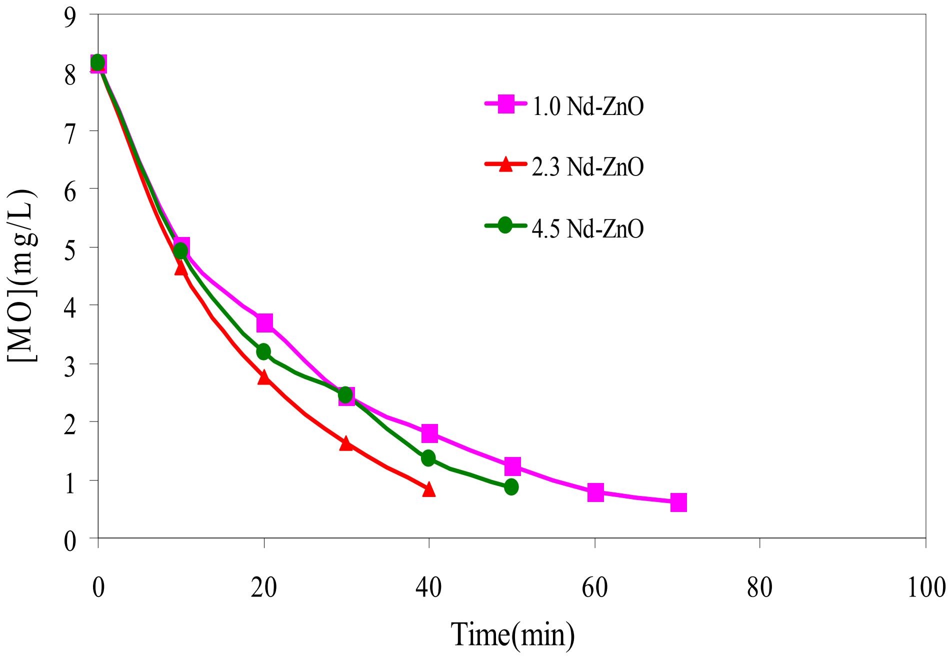

Figure 4.53. Effect of Nd loading on ZnO for the photocatalytic decolorization of MO. Conditions: pH= 5.85 (Natural), [MO]= 8.17 mg/L, I= 4.7x10^{15} photons/s, T=298 K

4.8.2. Effect of MO Concentration

The effect of initial dye concentration was investigated over a range of 3.27- 32.68 mg/L also in the presence of 1.0 Nd-ZnO (Figure 4.54). It is found that as the concentration of MO increases, the decolorization rate decreases due to the decreased probability of hydroxyl radical generation. Furthermore, in Figure 4.55 linearity is noticed which proves that MO by UV/ 1.0 Nd-ZnO process followed pseudo-first order kinetics. Calculated apparent rate-constants and regression values are shown in Table 4.20. For 1.0 Nd-ZnO catalyst, adsorption rate constants (K) and reaction rate constants (k_r) are also calculated as 0.210 mg^{-1}L and 0.441 mg/L min, respectively.

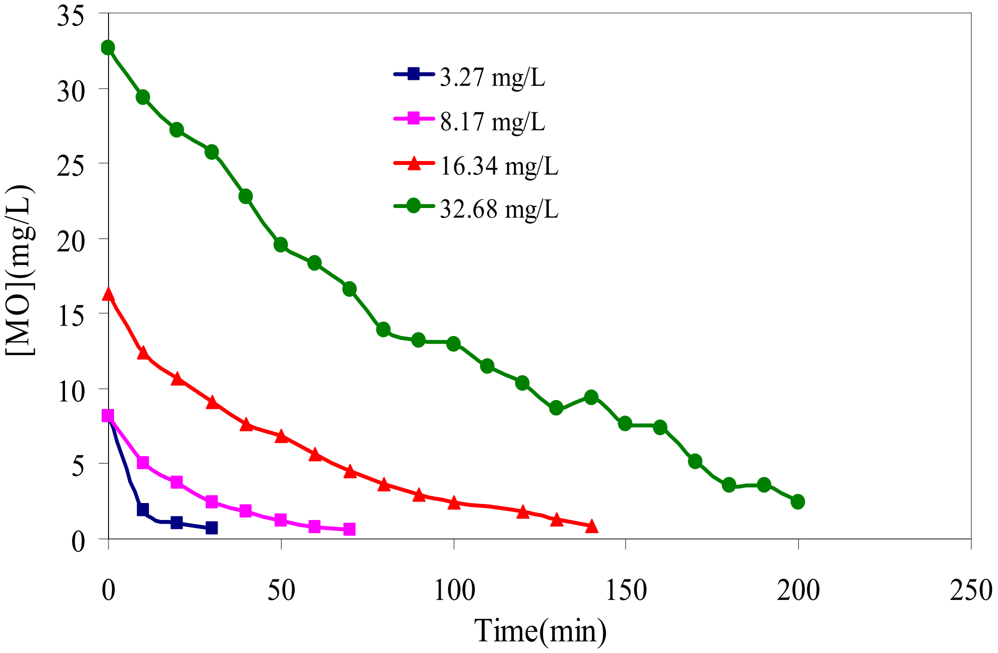

Figure 4.54. Photodecolorization of MO in the presence of 1.0 Nd-ZnO at different initial MO concentrations. Conditions: pH= 5.85 (Natural), I= 4.7x10^{15} photons/s, T=298 K

Table 4.20. Apparent first order rate constants (k_{app}) for the photocatalytic decolorization of MO at different initial concentrations and linear regression values

$[MO]_0$ (mg/L)	k_{app} (min^{-1})	R
32.68	0.0115	0.9524
16.34	0.0206	0.9805
8.17	0.0356	0.9978
3.27	0.0545	0.9985

4.8.3. Effect of pH

In Figure 4.56, the degree of photodecolorization of MO in the presence of 1.0 Nd-ZnO at a fixed reaction time is shown in the pH range of 2.0-10.0. The trend is same with the 1.0 Pr-ZnO. It is observed that the highest activity is obtained at pH 5.8 (natural pH) and the lowest percentage is noticed at pH 2.

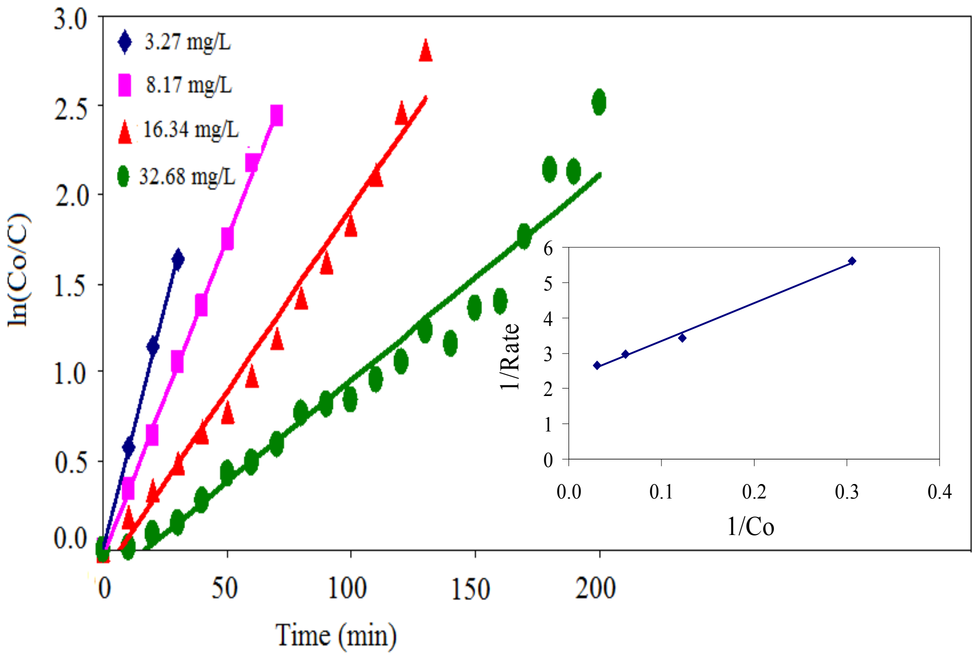

Figure 4.55. ln (C_o/C) vs. time plot in the presence of 1.0 Nd-ZnO. Conditions: pH= 5.85 (Natural), I= 4.7x10^{15} photons/s, T=298 K. Inset: 1/Rate vs. 1/C_o plot in the presence of 1.0 Nd-ZnO

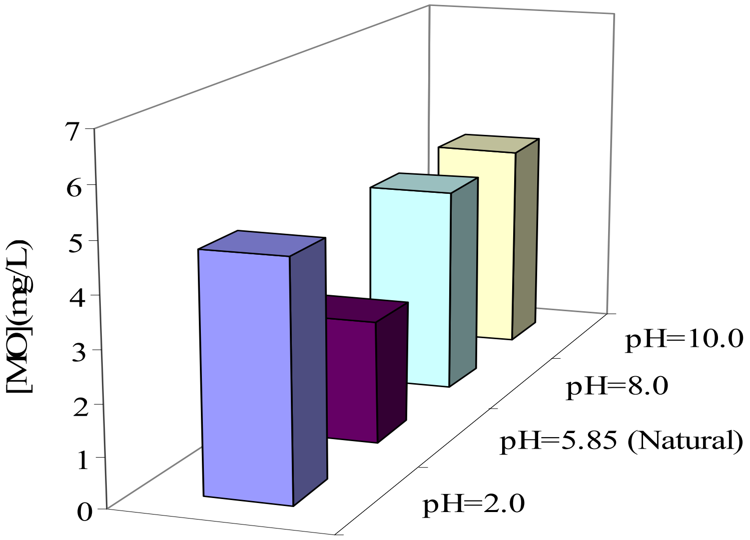

Figure 4.56. [MO] remaining in the solution (mg/L) after photodecolorization in the presence of 1.0 Nd-ZnO at different pH values. Conditions: [MO] = 8.17 mg/L, I= 4.7x1015 photons/s, T=298 K

4.9. Photocatalytic Degradation of MO in the Presence of Dy loaded ZnO

4.9.1. Effect of Dy^{3+} ion content

The effect of content of Dy^{+3} ion on decolorization of MO is shown in Figure 4.57. 1.0 Dy-ZnO catalyst showed the highest efficiency on photodegradation of MO.

4.9.2. Effect of MO Concentration

It is found that as the concentration of MO increases, the decolorization rate decreases in the presence of 1.0 Dy-ZnO over a range of 3.27- 32.68 mg/L (Figure 4.58). Also, in Figure 4.59 linearity is noticed proving that MO by UV/ 1.0 Dy-ZnO process followed pseudo-first order kinetics. Calculated apparent rate-constants and regression values are shown in Table 4.21. For 1.0 Dy-ZnO catalyst, adsorption rate constants (K) and reaction rate constants (k_r) are also calculated as 0.146 $mg^{-1}L$ and 0.507 mg/L min, respectively.

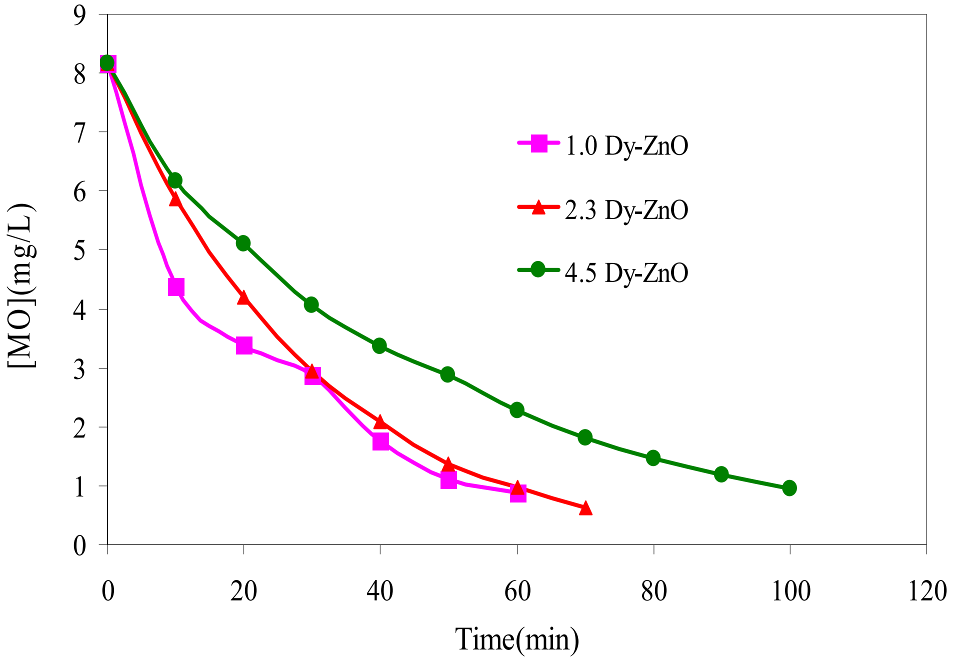

Figure 4.57. Effect of Dy loading on ZnO for the photocatalytic decolorization of MO. Conditions: pH= 5.85 (Natural), [MO]= 8.17 mg/L, I= $4.7x10^{15}$ photons/s, T=298 K

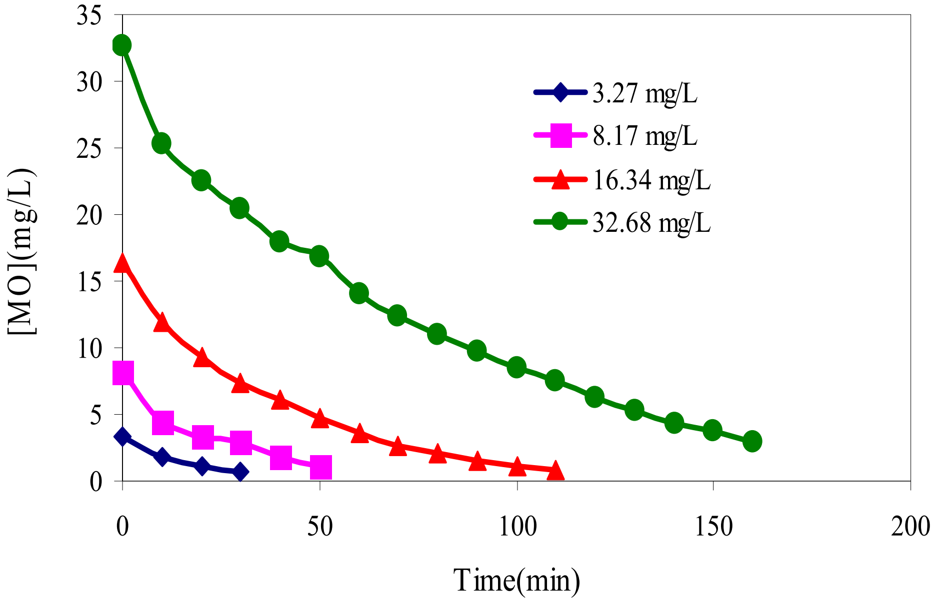

Figure 4.58. Photocolorization of MO in the presence of 1.0 Dy-ZnO at different initial MO concentrations. Conditions: pH= 5.85 (Natural), I= 4.7×10^{15} photons/s, T=298 K

Table 4.21. Apparent first order rate constants (k_{app}) for the photocatalytic decolorization of MO at different initial concentrations and linear regression values

$[MO]_0$ (mg/L)	k_{app} (min^{-1})	R
32.68	0.0140	0.9900
16.34	0.0264	0.9963
8.17	0.0344	0.9854
3.27	0.0524	0.9977

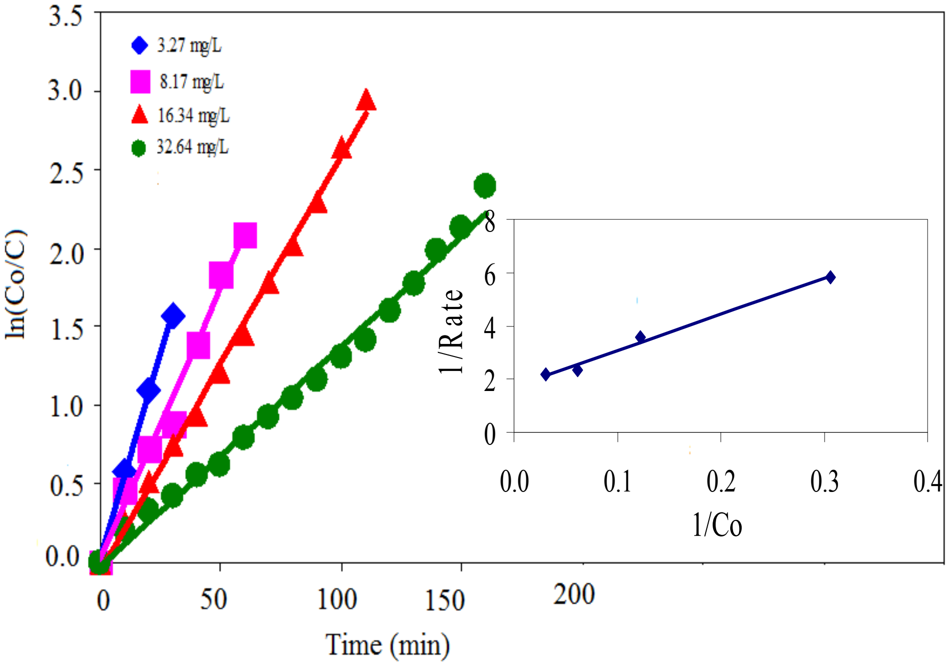

Figure 4.59. ln (C_o/C) vs. time plot in the presence of 1.0 Dy-ZnO.

Conditions: pH= 5.85 (Natural), I= 4.7×10^{15} photons/s, T=298 K

Inset: 1/Rate vs. 1/C_o plot in the presence of 1.0 Dy-ZnO

4.9.3. Effect of pH

In Figure 4.60, the degree of photodecolorization of MO with 1.0 Dy-ZnO at a fixed reaction time is shown in the pH range of 2.0-10.0. It is showed that the highest and lowest activity is obtained at pH 8 and pH 2 due to the favoured adsorption at $pH<pH_{zpc}$ and photocorrosion of ZnO through self-oxidation, respectively.

4.10. Photocatalytic Degradation of MO in the Presence of Eu loaded ZnO

4.10.1. Effect of Eu^{3+} ion content

The effect of content of Eu^{+3} ion on degradation of MO is shown in Figure 4.61. 1.0 Eu-ZnO catalyst showed the highest efficiency on photodecolorization of MO.

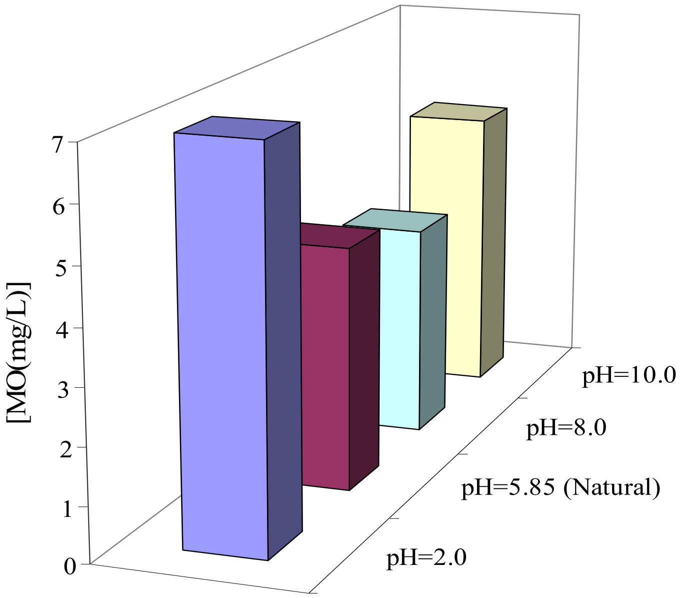

Figure 4.60. [MO] remaining in the solution (mg/L) after photodegradation in the presence of 1.0 Dy-ZnO at different pH values. Conditions: [MO] = 8.17 mg/L, I= 4.7x1015 photons/s, T=298 K

4.10.2. Effect of MO Concentration

It is found that as the concentration of MO increases, the decolorization rate decreases in the presence of 1.0 Eu-ZnO over a range of 3.27- 32.68 mg/L (Figure 4.62). Also, in Figure 4.63 linearity is noticed proving that MO by UV/ 1.0 Eu-ZnO process followed pseudo-first order kinetics. Calculated apparent rate-constants and regression values are shown in Table 4.22. For 1.0 Eu-ZnO catalyst, adsorption rate constants (K) and reaction rate constants (k_r) are also calculated as 0.041 $mg^{-1}L$ and 0.738 mg/L min, respectively.

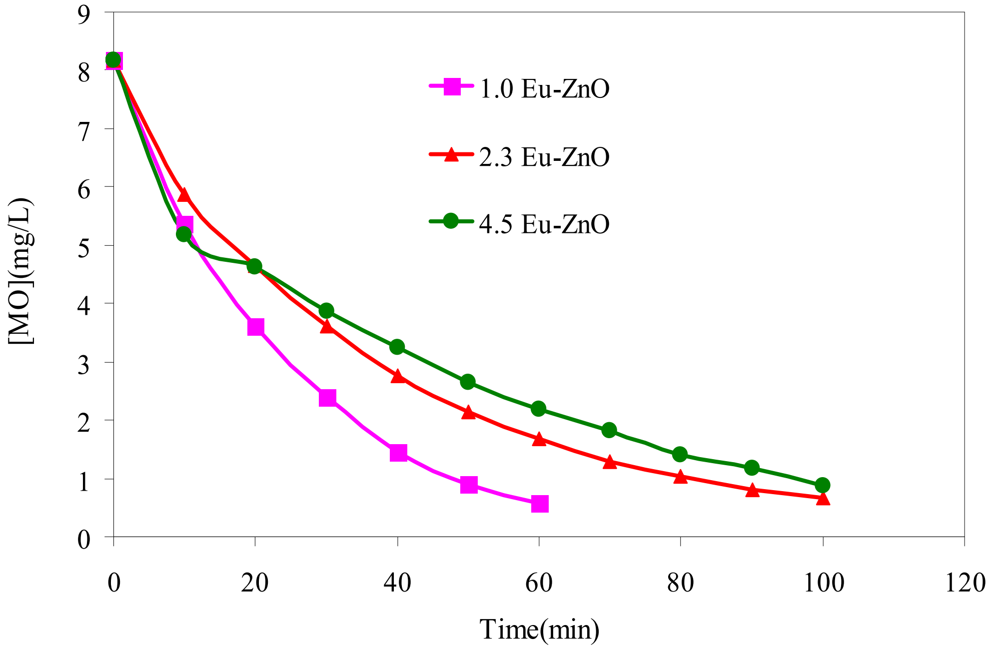

Figure 4.61. Effect of Eu loading on ZnO for the photocatalytic decolorization of MO. Conditions: pH= 5.85 (Natural), [MO]= 8.17 mg/L, I= 4.7×10^{15} photons/s, T=298 K

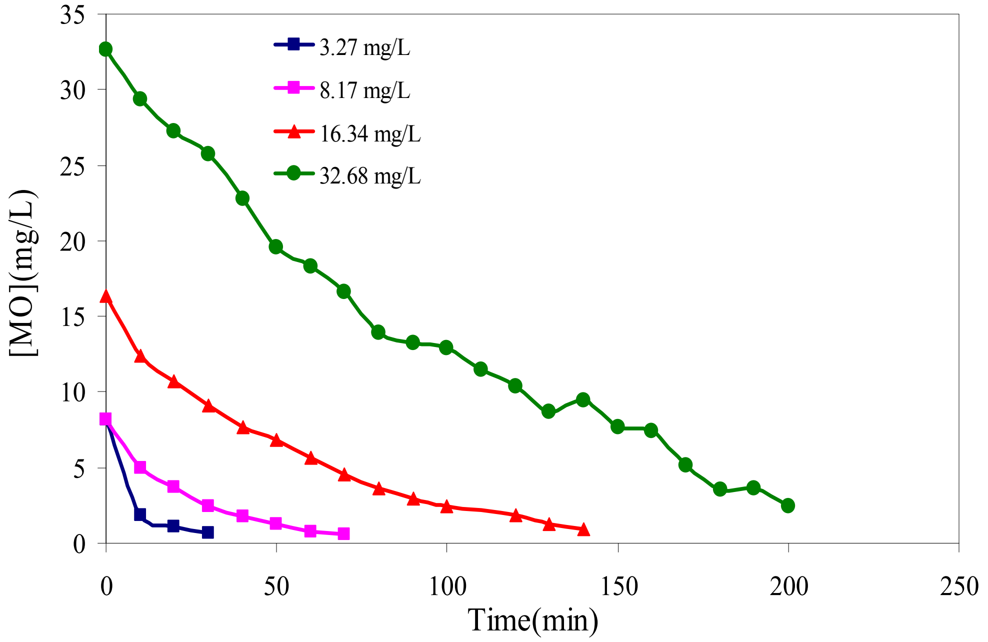

Figure 4.62. Photodecolorization of MO in the presence of 1.0 Eu-ZnO at different initial MO concentrations. Conditions: pH= 5.85 (Natural), I= 4.7×10^{15} photons/s, T=298 K

Table 4.22. Apparent first order rate constants (k_{app}) for the photocatalytic decolorization of MO at different initial concentrations and linear regression values

$[MO]_0$ (mg/L)	k_{app} (min^{-1})	R
32.68	0.0129	0.9800
16.34	0.0206	0.9986
8.17	0.0209	0.9935
3.27	0.0270	0.9996

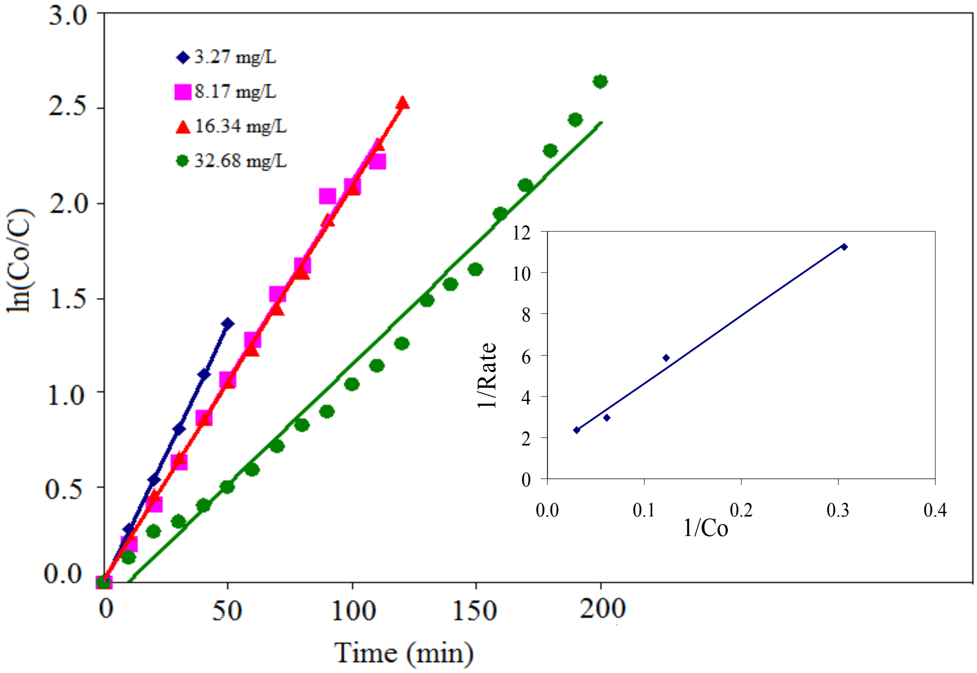

Figure 4.63. ln (C_o/C) vs. time plot in the presence of 1.0 Eu-ZnO.

Conditions: pH= 5.85 (Natural), I= $4.7x10^{15}$ photons/s, T=298 K.

Inset: 1/Rate vs. $1/C_o$ plot in the presence of 1.0 Eu-ZnO

4.10.3. Effect of pH

In Figure 4.64, the degree of photodecolorization of MO with 1.0 Eu-ZnO at a fixed reaction time is shown in the pH range of 2.0-10.0. It is showed that the highest and lowest activity is obtained at pH 8 and pH 2 due to the favoured adsorption at $pH<pH_{ZPC}$ and photocorrosion of ZnO through self-oxidation, respectively.

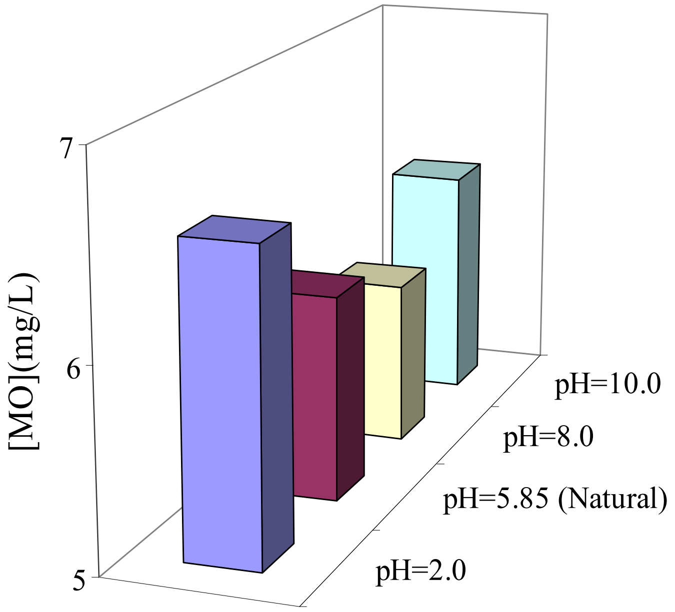

Figure 4.64. [MO] remaining in the solution (mg/L) after photodecolorization in the presence of 1.0 Eu-ZnO at different pH values. Conditions: [MO] = 8.17 mg/L, I= 4.7x1015 photons/s, T=298 K

4.11. Photocatalytic Degradation of MO in the Presence of Gd loaded ZnO

4.11.1. Effect of Gd^{3+} ion content

The effect of content of Gd^{+3} ion on decolorization of MO is shown in Figure 4.65 1.0 Gd-ZnO catalyst showed the highest efficiency on photodecolorization of MO.

4.11.2. Effect of MO Concentration

It is found that as the concentration of MO increases, the decolorization rate decreases in the presence of 1.0 Gd-ZnO over a range of 3.27- 32.68 mg/L (Figure 4.66). Also, in Figure 4.67 linearity is noticed proving that MO by UV/ 1.0 Gd-ZnO process followed pseudo-first order kinetics. Calculated apparent rate-constants and regression values are shown in Table 4.23. For 1.0 Gd-ZnO catalyst, adsorption rate constants (K) and reaction rate constants (k_r) are also calculated as 0.142 $mg^{-1}L$ and 0.512 mg/L min, respectively.

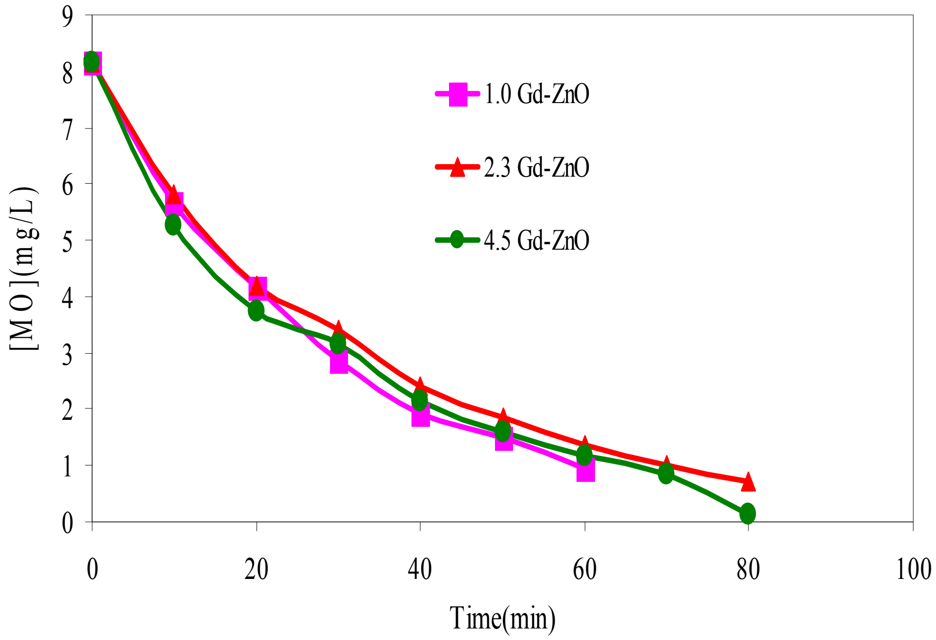

Figure 4.65. Effect of Gd loading on ZnO for the photocatalytic decolorization of MO. Conditions: pH= 5.85 (Natural), [MO]= 8.17 mg/L, I= 4.7x10^{15} photons/s, T=298 K

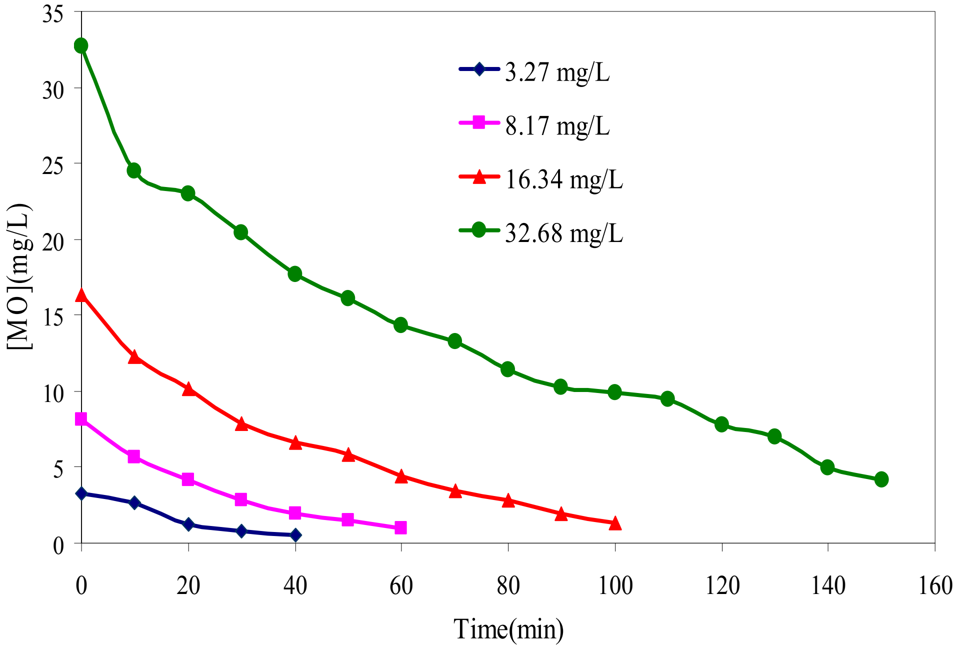

Figure 4.66. Photodecolorization of MO in the presence of 1.0 Gd-ZnO at different initial MO concentrations. Conditions: pH= 5.85 (Natural), I= 4.7x10^{15} photons/s, T=298 K

Table 4.23. Apparent first order rate constants (k_{app}) for the photocatalytic decolorization of MO at different initial concentrations and linear regression values

$[MO]_0$ (mg/L)	k_{app} (min^{-1})	R
32.68	0.0118	0.9775
16.34	0.0231	0.9880
8.17	0.0349	0.9968
3.27	0.0491	0.9773

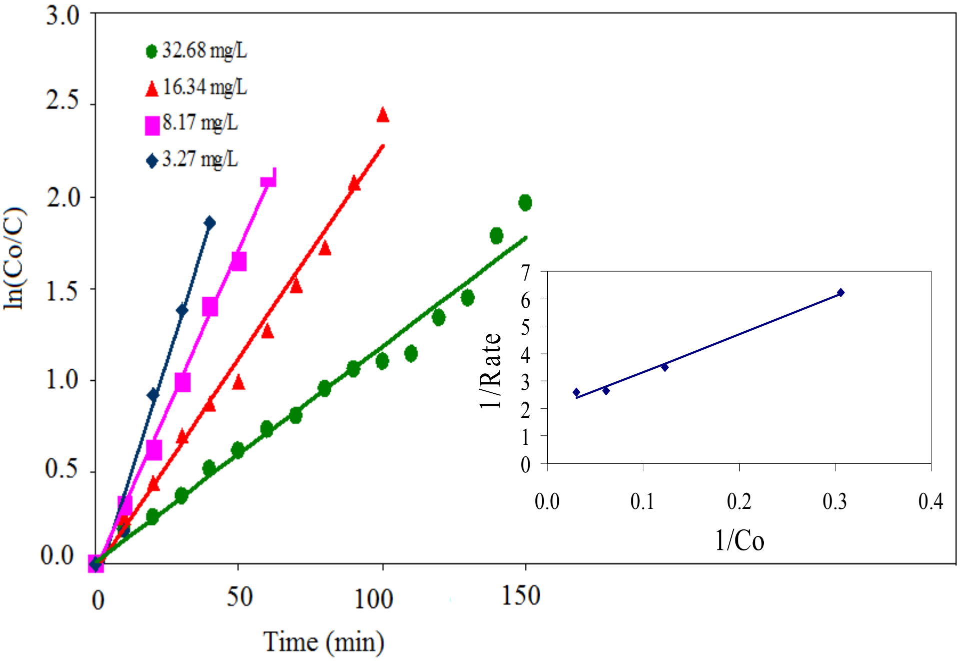

Figure 4.67. ln (C_o/C) vs. time plot in the presence of 1.0 Gd-ZnO.
Conditions: pH= 5.85 (Natural), I= 4.7x10^{15} photons/s, T=298 K.
Inset: 1/Rate vs. 1/C_o plot in the presence of 1.0 Gd-ZnO

4.11.3. Effect of pH

In Figure 4.68, the degree of photodecolorization of MO with 1.0 Gd-ZnO at a fixed reaction time is shown in the pH range of 2.0-10.0. It is showed that the highest and lowest activity is obtained at pH 8 and pH 2 due to the favoured adsorption at $pH<pH_{ZPC}$ and photocorrosion of ZnO through self-oxidation, respectively.

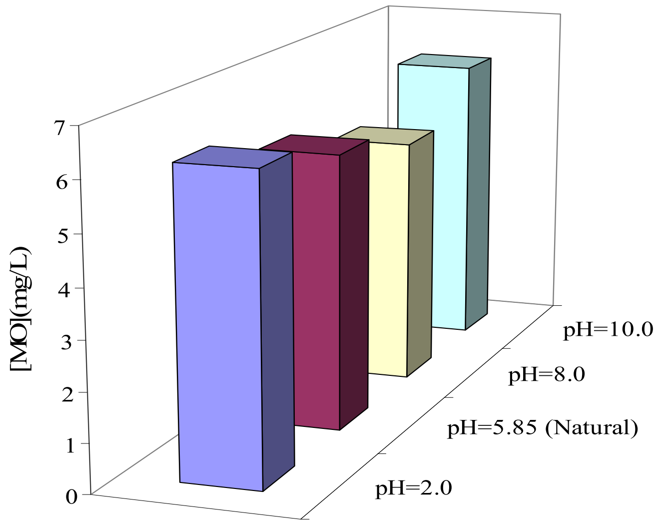

Figure 4.68. [MO] remaining in the solution (mg/L) after photodecolorization in the presence of 1.0 Gd-ZnO at different pH values. Conditions: [MO] = 8.17 mg/L, I= 4.7x1015 photons/s, T=298 K

4.12. Photocatalytic Degradation of MO in the Presence of Ho loaded ZnO

4.12.1. Effect of Ho^{3+} ion content

The effect of content of Ho^{+3} ion on decolorization of MO is shown in Figure 4.69. 1.0 Ho-ZnO catalyst showed the highest efficiency on photodecolorization of MO.

4.12.2. Effect of MO Concentration

It is found that as the concentration of MO increases, the decolorization rate decreases in the presence of 1.0 Ho-ZnO over a range of 3.27- 32.68 mg/L (Figure 4.70). Also, in Figure 4.71 linearity is noticed proving that MO by UV/ 1.0 Ho-ZnO process followed pseudo-first order kinetics. Calculated apparent rate-constants and regression values are shown in Table 4.24. For 1.0 Ho-ZnO catalyst, adsorption rate constants (K) and reaction rate constants (k_r) are also calculated as 0.136 $mg^{-1}L$ and 0.718 mg/L min, respectively.

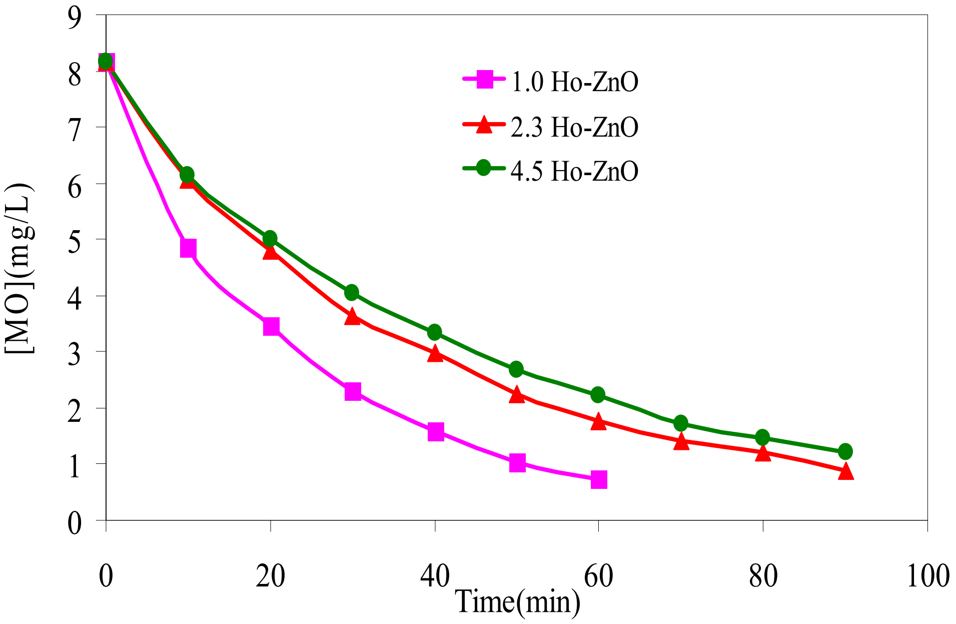

Figure 4.69. Effect of Ho loading on ZnO for the photocatalytic decolorization of MO. Conditions: pH= 5.85 (Natural), [MO]= 8.17 mg/L, I= 4.7x10^{15} photons/s, T=298 K

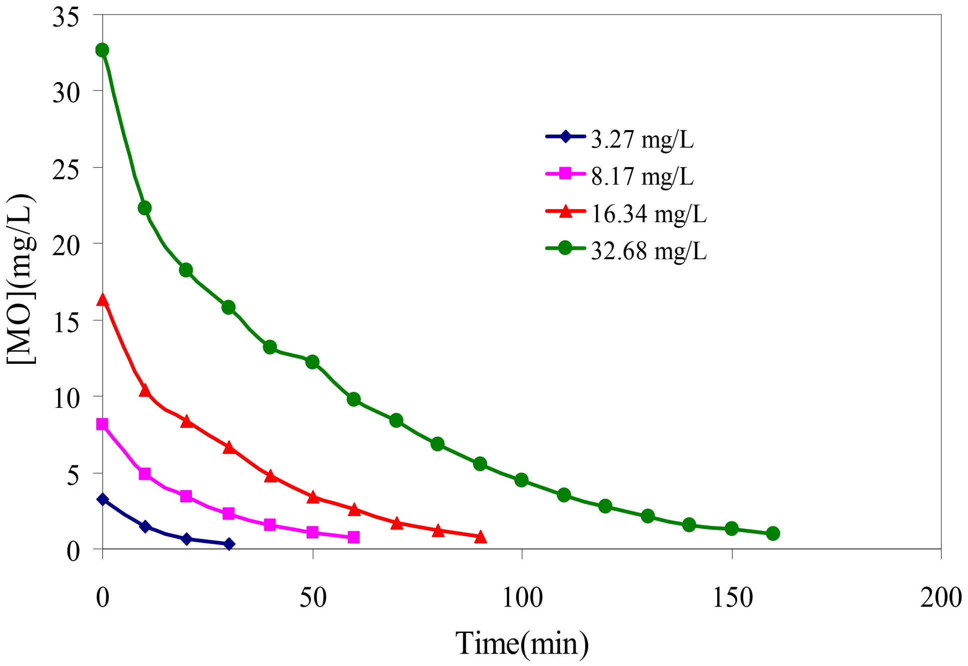

Figure 4.70. Photodecolorization of MO in the presence of 1.0 Ho-ZnO at different initial MO concentrations.
Conditions: pH= 5.85 (Natural), I= 4.7x10^{15} photons/s, T=298 K

Table 4.24. Apparent first order rate constants (k_{app}) for the photocatalytic decolorization of MO at different initial concentrations and linear regression values

$[MO]_0$ (mg/L)	k_{app} (min^{-1})	R
32.68	0.0204	0.9976
16.34	0.0316	0.9995
8.17	0.0386	0.9929
3.27	0.0702	0.9886

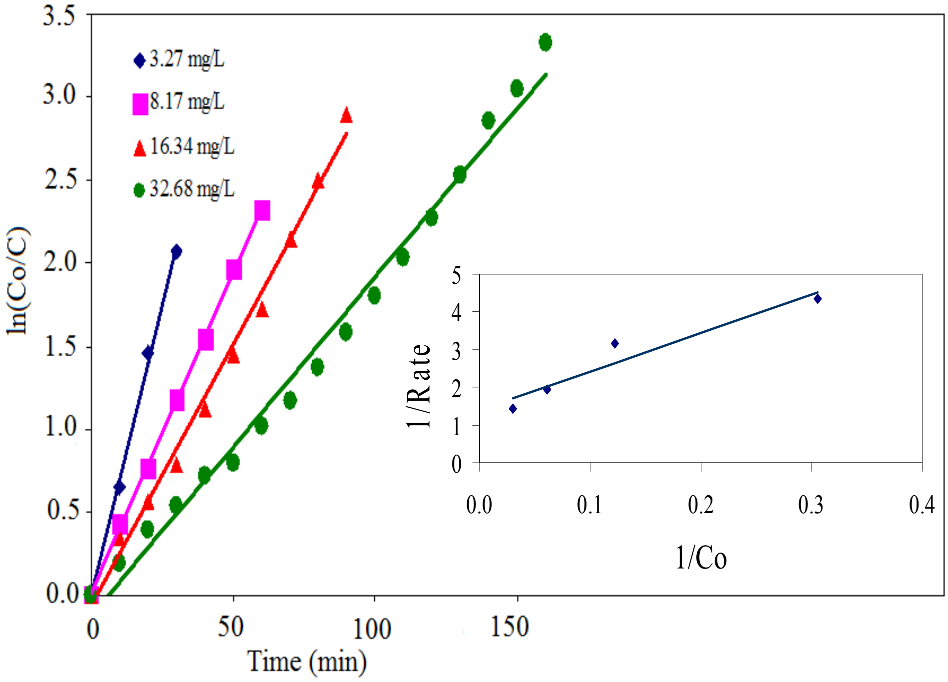

Figure 4.71. ln (C_o/C) vs. time plot in the presence of 1.0 Ho-ZnO. Conditions: pH= 5.85 (Natural), I= 4.7×10^{15} photons/s, T=298 K. Inset: 1/R vs. 1/C_o plot in the presence of 1.0 Ho-ZnO

4.12.3. Effect of pH

In Figure 4.72, the degree of photodecolorization of MO with 1.0 Ho-ZnO at a fixed reaction time is shown in the pH range of 2.0-10.0. It is showed that the highest and lowest activity is obtained at pH 8 and pH 2 due to the favoured adsorption at $pH<pH_{zpc}$ and photocorrosion of ZnO through self-oxidation, respectively.

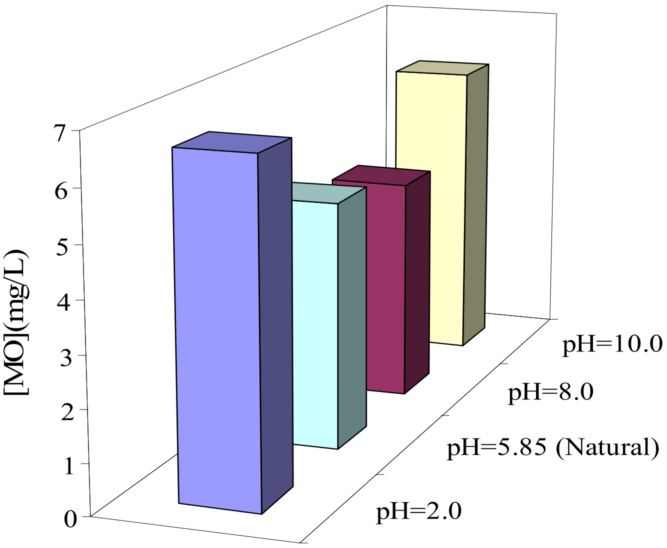

Figure 4.72. [MO] remaining in the solution (mg/L) after photodecolorization in the presence of 1.0 Ho-ZnO at different pH values. Conditions: [MO] = 8.17 mg/L, I= 4.7×10^{15} photons/s, T=298 K

4.12. General Remarks

To sum up our results, the catalysts in the order of decreasing photocatalytic performances are illustrated in Figure 4.73. It seems that few factors have an interrelated influence on the effect of lanthanide (Ln) ions loading in our catalyst systems:

The ionic radii of La^{3+}, Pr^{3+}, Nd^{3+}, Eu^{3+}, Gd^{3+}, Dy^{3+} and Ho^{3+} are 0.116, 0.113, 0.111, 0.107, 0.105, 0.103 and 0.102 nm, respectively, and much larger than that of Zn^{2+} (0.074 nm). Therefore, it is difficult for these rare earth ions to enter into the lattice of ZnO. The formation of oxide forms of these ions during the calcination process proved by the XRD analysis. Since calculated crystal sizes of the oxides cannot match with the pore sizes of the catalysts, distribution of these oxides on the surface of ZnO catalyst is accepted.

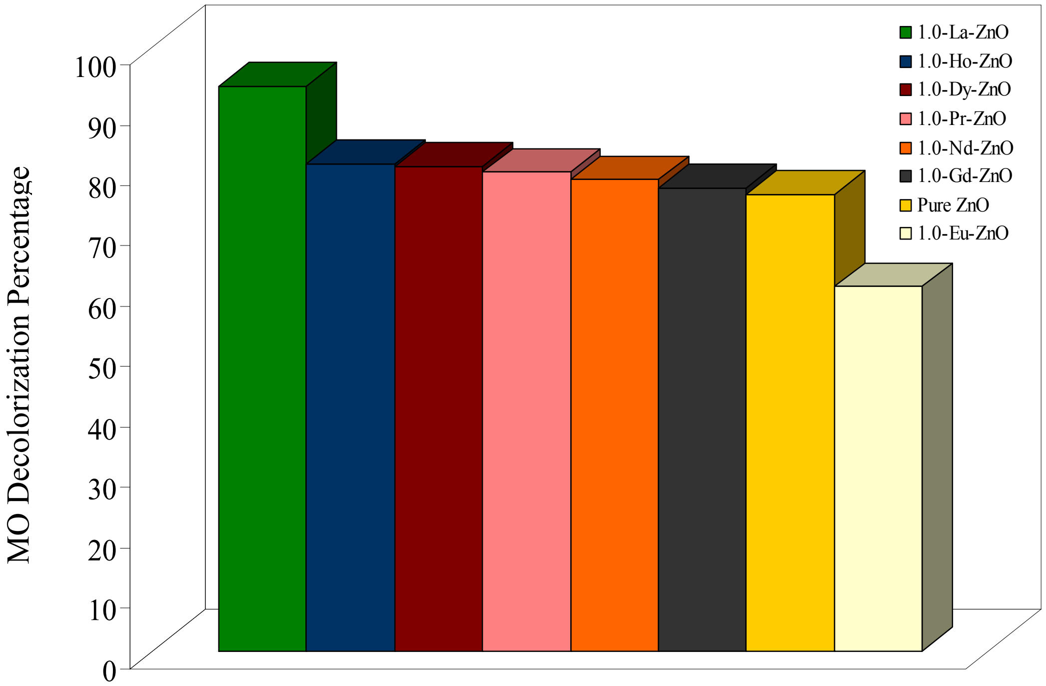

Figure 4.73. MO decolorization percentage after 40 min irradiation time

Accordingly, such a new catalyst system may favour separating charge carriers efficiently, prolonging the life of carriers, inhibiting the recombination of electron-hole pairs and eventually causing enhancement of the reactivity with the following reactions.

Rare earth metal ions used in this study are all in +3 oxidation state. The electron configurations are as La^{3+} = [Xe], Pr^{3+}= [Xe] $4f^{2}$, Nd^{3+}= [Xe] $4f^{3}$, Eu^{3+}= [Xe] $4f^{6}$, Gd^{3+}= [Xe] $4f^{7}$, Dy^{3+}= [Xe] $4f^{9}$, Ho^{3+}= [Xe] $4f^{10}$. Accordingly, these ions are able to scavenge photogenerated electrons (Equation 4.6).

$$Ln^{3+} + e_{CB}^{-} \rightarrow Ln^{2+} \quad (4.6)$$

However, stabilities of Ln^{3+} ions may be disturbed in the reduced form (Ln^{2+}); specifically for La^{2+} ([Xe] $5d^1$,with an extra electron in 5d orbital) and Gd^{2+} (([Xe] $4f^7$ $5d^1$,with an extra electron in 5d orbital). For the other ions, extra electron increases the number of electrons in the 4f orbitals (Pr^{2+}: [Xe] $4f^3$, Nd^{2+}: [Xe] $4f^4$, Eu^{2+}: [Xe] $4f^7$, Dy^{2+}: [Xe] $4f^{10}$, Ho^{2+}: [Xe] $4f^{11}$). While Eu, Dy and Ho tend to stay in their reduced forms (since Eu^{2+}: [Xe] $4f^7$ has the most stable configuration with 7 electrons in 4f sub-shell, Dy^{2+} and

Ho^{2+} have more paired electrons in their 4f sub-shells), Pr^{2+} and Nd^{2+} tend to return in their +3 oxidation states.

Accordingly, La^{2+}, Gd^{2+}, Pr^{2+} and Nd^{2+} ions have a tendency to transfer the trapped electron to O_2 according to Equation (4.7):

$$Ln^{2+} + O_2 \rightarrow Ln^{3+} + O_2^{\bullet -} \qquad (4.7)$$

The produced superoxide radical ($O_2^{\bullet -}$) in Equations 4.8-4.10 plays a major role in the generation of $^{\bullet}OH$ radicals by the following reactions:

$$O_2^{\bullet -} + H^+ \rightarrow HO_2^{\bullet} \qquad (4.8)$$

$$2HO_2^{\bullet} \rightarrow H_2O_2 + O_2 \qquad (4.9)$$

$$H_2O_2 + e^- \rightarrow OH^- + \bullet OH \qquad (4.10)$$

Since, oxidative degradation of azo dyes occurs generally by the subsequent attacks of $^{\bullet}OH$ radicals as already mentioned in the postulated mechanism of MO degradation (section 3.1.2), loading of rare earth metal ions on the ZnO surface increase the formation possibility of $^{\bullet}OH$ radicals.

In the view of these electronic configurations, we also consider surface areas, surface morphologies and crystal sizes of rare earth metal ion loaded ZnO catalysts.

i) First comparison is done in between 1.0 La-ZnO and 1.0 Gd-ZnO catalysts. These catalysts resemble stable electron configurations. In XRD analysis, La_2O_3 and Gd_2O_3 crystals do not form at 400°C. Meanwhile, ZnO crystalline sizes are almost the same in both of these catalysts. Particle sizes measured in AFM analysis are also similar (55.8 nm for 1.0 La-ZnO and 52 nm for 1.0 Gd-ZnO). However, they possess completely different activities. Although 1.0 Gd-ZnO has a higher surface area (98 m^2/g) in comparison to 1.0 La-ZnO (61.78 m^2/g), it shows a lower performance. Hence, we understand that it is not obligatory that the large surface area to stimulate large adsorption ability and a faster destruction of the dye. When average surface roughness values is taken into consideration, it is observed that 1.0 La-ZnO has a higher Ra (6.398 nm) value compared to that of 1.0 Gd-ZnO (0.245 nm). The pronounced roughness of 1.0 La-ZnO probably contributes to higher sorption ability of the catalyst. Therefore, a relatively higher adsorption rate constant “K” (0.156 $mg^{-1}L$) and reaction rate constant “k_r” (0.634 mg/L min) are obtained for 1.0 La-ZnO in comparison to 1.0 Gd-ZnO (K=0.142 $mg^{-1}L$, k_r=0.512 mg/L min).

ii) Second comparison is done in between 1.0 Dy-ZnO and 1.0 Ho-ZnO catalysts. These catalysts prefer to have more paired electrons in their 4f-subshells. XRD results indicate that oxide forms of these metals do not form at 400°C. From AFM analysis, almost similar particle sizes are obtained as 42.2 nm and 35 nm for 1.0 Dy-ZnO and 1.0 Ho-ZnO, respectively. The surface area of 1.0 Dy-ZnO (66.96 m^2/g) is lower than that of 1.0 Ho-ZnO (76.04 m^2/g). However, surface roughness value for 1.0 Dy-ZnO (0.618 nm) is much higher than the roughness of 1.0 Ho-ZnO (0.138 nm). Similar adsorption rate constants “K” (0.146 $mg^{-1}L$ for 1.0 Dy-ZnO and 0.136 $mg^{-1}L$ for 1.0 Ho-ZnO) and reaction rate constants “k_r” (0.507 mg/L min for 1.0 Dy-ZnO and 0.718 mg/L min for 1.0 Ho-ZnO) are obtained. All these results conclude with the analogous photocatalytic activities of the catalysts; 1.0 Dy-ZnO and 1.0 Ho-ZnO.

iii) Third comparison is done in between 1.0 Pr-ZnO and 1.0 Nd-ZnO catalysts. These catalysts also exhibit similar electron configurations, dark adsorption percentages (13 per cent for 1.0 Pr-ZnO and 14 per cent for 1.0 Nd-ZnO), surface areas (72.2 m^2/g for 1.0 Pr-ZnO and 70.01 m^2/g for 1.0 Nd-ZnO) and similar adsorption rate constants “K” (0.129 $mg^{-1}L$ for 1.0 Pr-ZnO and 0.210 $mg^{-1}L$ for 1.0 Ho-ZnO) and reaction rate constants “k_r” (0.438 mg/L min for 1.0 Dy-ZnO and 0.441 mg/L min for 1.0 Ho-ZnO). According to AFM results, particle sizes (34 nm for 1.0 Pr-ZnO and 60.44 nm for 1.0 Nd-ZnO) and roughness values (6.688 nm for 1.0 Pr-ZnO and 1.140 nm for 1.0 Nd-ZnO) differ. This may be creating the small difference in their photocatalytic behaviours; 1.0 Pr-ZnO shows a little higher activity than 1.0 Nd-ZnO.

iv) The last catalyst in the list is 1.0 Eu-ZnO. It reveals the lowest performance among the other catalysts including pure ZnO. Although 1.0 Eu-ZnO stays with the stable electron configuration, possesses a similar surface area to the others (67.68 m^2/g) and an average roughness value (3.67 nm), it forms aggregates of 86 nm size. This induces a much lower adsorption rate constant 0.041 $mg^{-1}L$. However, the reaction rate constant 0.738 mg/L min seems to be higher, indicating that photocatalytic reaction does not occur on the catalyst surface instead it takes place in solution phase.

v) The pure ZnO is a kind of support in our catalyst system to host the rare earth ions or their oxide forms after calcination. The surface area of pure ZnO (59.46 m^2/g) is less in comparison to the other catalysts, and this may be another clue for distribution of metals on the ZnO surface. The sizes of aggregates in the presence of pure ZnO become smaller with the adsorption of rare earth metals, indicating a new force distribution on the surface. All these affect the photocatalytic activity, while pure form shows a lower performance, rare earth loaded forms demonstrate an enhanced performance.

A closer inspection clarifies blue shifts in the DRS spectra of the rare earth loaded ZnO catalysts depending on the content of the metal ion. This indicates an increase in the band gap energies of the corresponding catalysts, contributing to the inhibition of electron-hole recombination reaction. However, performances of the catalysts decrease as the amount of loading increases.

The optimum concentration of the rare earth loading (1 wt. per cent) is due to the fact that there exists an optimum level for the content of rare earth ions on ZnO particles for the most efficient separation of photoinduced electron-hole pairs. As the concentration of rare earth ions increases, the space charge region becomes very narrow and the penetration depth of light into ZnO greatly exceeds the space charge layer, therefore the recombination of electron-hole pairs in the semiconductor become easier. In general, 1 wt. per cent loading of rare earth ions is enough to make the thickness of space charge layer substantially equal to the light penetration depth. Moreover, the band gap energies of the rare earth oxides used in the experiments are not sufficient for initiating photocatalytic reactions after UV irradiation [56]. Accordingly, excess amounts of rare earth oxide covering the surface of ZnO would increase the number of recombination centers and result in low photoactivity. So it is not a surprise that rare earth ions loaded with more than 1 wt. percent show poor activity.

Table 4.25 summarizes the optimized conditions of the photocatalytic degradation experiments performed in the presence of as-prepared catalysts.

Table 4.25. Optimum Conditions

Catalyst Amount	0.1 g
Metal-ion Content	1.0 per cent
Initial MO Concentration	8.17 mg/L
pH	8.0

5. CONCLUSION

In this study, pure ZnO and rare-earth metal loaded ZnO catalysts were synthesized, characterized and evaluated for photodecolorization of model compound (MO) under UV illumination.

Characterizations of the catalysts were done by using XRD, BET, SEM-EDX, AFM and DRS techniques. XRD patterns supplied information about the diffractions of parent ZnO and metal oxides. Crystalline sizes of particles were also calculated by using XRD data before and after metal ion loadings. In addition, surface areas and pore sizes of as-prepared catalysts were measured. Morphological variations were detected both in SEM and AFM images. EDX analysis provided certain peaks of Zn, O and the rare earth metal ion, indicating existence of metals on the surface of the corresponding catalyst. DRS plots showed blue shifts in the absorption band of ZnO owing to the adsorption of metals and their increasing percentages.

Photocatalytic performances of the catalysts for the probe molecule MO were controlled under the effects of initial MO concentration, metal ion content, catalyst loading, and pH of the medium. Pseudo-first order kinetics was followed at the natural pH of MO solution and for the lowest metal ion content. Langmuir-Hinshelwood model was also rationalized in our catalyst systems. A mechanism was postulated in the decolorization process of MO.

On the basis of our results, we propose that rare earth metal ion loading on ZnO presents a successful catalyst model which can be well used not only for the decolorization of MO but also for the further research in photocatalytic processes leading to the development of water treatment.

REFERENCES

1. Akyol, A., H. Yatmaz and M. Bayramoğlu, “ Photocatalytic Decolorization of Remazol Red RR in Aqueous ZnO Suspensions”, *Applied Catalysis B: Environmental*, Vol. 54, pp. 19-24, 2004.

2. Parsons, S. and M. Williams. 2004. *Advanced Oxidation Processes for Water and Wastewater Treatment.* Parsons, S. (ed). IWA Publishing, London, UK.

3. Ellmer, K., A. Klein and B. Rech, “*Transparent Conductive Zinc Oxide Basics and Applications in Thin Film Solar Cells”*, first edition, Springer, Heidelberg, 2008.

4. Klingshirn, C., "ZnO: Material, Physics and Applications", *A European Journal of Chemical Physics and Physical Chemistry,* Vol. 8, pp. 782, 2007.

5. Mahmud, S., "Nanostructure of ZnO fabricated via French Process and Its Correlation to Electrical Properties of Semiconducting Varistors", *Synthesis and Reactivity in Inorganic, Metal-Organic, and Nano-Metal Chemistry,* Vol. 36, pp. 155, 2006.

6. Porter, F., " *Zinc Handbook: Properties, Processing, and Use in Design*", Marcel Dekker, New York, 1991.

7. Cheung, J., “*History and Fundementals of Pulsed Laser Deposition, In: Pulsed Laser Deposition of Thin Films”*, first edition, Wiley- Interscience, New York, 1994.

8. Bauerle, D., “*Laser Chemical Processing”,* Springer, Berlin, 2004**.**

9. Martin, G., L.A. Doyle, A. Al-Khateeb, I. Weaver, D. Riley, M.J. Lamb, T. Morrow and C.L.S. Lewis, “ Three-Dimensional Number Density Mapping in the Plume of a Low Temperature Laser-Ablated Magnesium Plasma”, *Applied Surface Science*, Vol. 127-129, pp. 710-715, 1998.

10. Yu, P. and M. Cardona, "Fundamentals of Semiconductors", *Physics and Materials Properties*, 2nd ed., Springer, Newyork, 1999.

11. Anpo, M., M. Takeuchi, K. Ikeue and S. Dohshi, "Design and Development of Titanium Oxide Photocatalysts Operating Under Visible and UV Light Irradiation.: The Applications of Metal Ion-Implantation Techniques to Semiconducting TiO_2 and Ti/zeolite Catalysts", *Current Opinion in Solid State and Material Science*, Vol. 6, pp. 381-388, 2002.

12. Carp, O., C. L. Huisman and A. Reller, "Photoinduced Reactivity of Titanium Dioxide", *Progress in Solid State Chemistry*, Vol. 32, pp.33-177, 2004.

13. Legrini, O., E. Olivers and A.M. Braun, "Photochemical Processes for Water Treatment", *Chemical Reviews,* Vol. 93, pp. 671, 1993.

14. Mathews, R. and S.R. McEvoy, " Photocatalytic degradation of phenol in the presence of near-UV illuminated titanium dioxide", *Journal of Photochemistry and Photobiology A: Chemistry,* Vol. 64, pp. 231-246, 1992.

15. Li, X. and F. B. Li, "Study of Au-Au^{+3}- TiO_2 Photocatalysts Toward Visible Photooxidation for Water and Wastewater Treatment", *Journal of Environmental Science and Technology,* Vol. 35, pp. 2381-2387, 2001.

16. Kamat, P., " Photo-induced Transformations in Semiconductor-metal Nanocomposite Assemblies", *Journal of Applied Chemistry,* Vol. 74, pp. 1693-1706, 2002.

17. Klosek, S. and D. Raftery, "Visible Light Driven V-doped TiO_2 Photocatalyst and Its Photo-oxidation of Ethanol", *Journal of Physical Chemistry B*, Vol. 105, pp. 2815-2819, 2001.

18. Dindar, B. and S. Icli, "Unusual Photoreactivity of Zinc Oxide Irradiated by Concentrated Sunlight", *Journal of Photochemistry and Photobiology A: Chemistry,* Vol. 140, pp. 263-268, 2001.

19. Carraway, E., A. J. Hoffman and M. Hoffman, “ Photocatalytic Oxidation of Organic Acids on Quantum-Sized Semiconductor Colloids”, *Environmental Science & Technology,* Vol. 28, pp. 786-793, 1994.

20. Poulios, I., D. Makri and X. Prohaska, “Photocatalytic Treatment of Olive Milling Waste Water, Oxidation of Protocatechuic Acid”, *International Journal*, Vol. 1, pp. 55-62, 1999.

21. Pall, B. and M. Sharon, “Enhanced Photocatalytic Activity of Highly Porous ZnO Thin Films Prepared by Sol-Gel Process”, *Materials Chemistry and Physics,* Vol. 76, pp. 82-87, 2002.

22. Carp, O., C.L. Huisman and A. Reller, “Photoinduced Reactivity of Titanium Dioxide”, *Progress in Solid State Chemistry,* Vol. 32, pp. 33-177, 2004.

23. Brunauer, S., P. H. Emmett and E. Teller, “Adsorption of Gases in Multimolecular Layers”, *Journal of The American Chemical Society*, Vol. 60, pp. 309-319, 1938.

24. Brunauer, S., P. H. Emmett and E. Teller, “Adsorption of Gases in Multimolecular Layers”, *Journal of American Chemical Society*, Vol. 60, pp. 309-319, 1938.

25. Atkins P., J. Paula, “*Atkin’s Physical Chemistry*”, 7th ed., New York, 2002.

26. Fouad, O., A. A. Ismail, Z. I. Zaki and R. M. Mohamed, “Zinc Oxide Thin Films Prepared by Thermal Evaporation Deposition and Its Photocatalytic Activity”, *Applied Catalysis B: Environmental,* Vol. 62, pp. 144-169, 2006.

27. Bach, U., Lupo D., Comte P., Moster J.E. and Weissortel F., “Solid-state Dye-Sensitized Mesoporous TiO_2 Solar Cells with High Photon-to-electron Conversion Efficiencies”, *Nature,* Vol. 395, pp. 583, 1998.

28. Schiavello, M., “*Heterogeneous Photocatalysis”,* Wiley, England, 1997.

29. Anandan, S., A. Vinu, K.L.P Sheeja Lovely, N. Gokulakrishnan, P. Srinivasu, T. Mori, V. Murugesan, V. Sivamurugan and K. Ariga, " Photocatalytic Activity of La-doped ZnO for the Degradation of Monocrotophos in Aqueous Suspension", *Journal of Molecular Catalysis A. Chemical*, Vol: 266, pp. 149-157, 2007.

30. Lizama, C., J. Freer, J. Baeza and H.D. Mansilla, "Optimized Photodegradation of Reactive Blue 19 On TiO_2 and ZnO Suspension", *Catalysis Today*, Vol. 76, pp. 235-246, 2002.

31. Pal, B. and M.Sharon, " Enhanced Photocatalytic Activiy of Highly Porous ZnO Thin Films Prepared by Sol-Gel Process", *Materials Chemistry and Physics*, Vol. 76, pp. 82-87, 2002.

32. Music, S., D. Dragcevic, M. Maljkovic and S. Popovic, " Influence of Chemical Synthesis on the Crystallization and Properties of Zinc Oxide", *Materials Chemistry and Physics*, Vol. 77, pp. 521-530, 2002.

33. Lima, S., F. A. Sigoli, M. R. Davolos and M. Jafelicci Jr., "Europium(III)-containing Zinc Oxide from Pechini Method", *Journal of Alloys and Compounds*, Vol. 344, pp. 280-284, 2002.

34. Daneshvar, N., D. Salari and A.R. Khataee, " Photocatalytic Degradation of Azo Dye Acid Red 14 in Water on ZnO as an Alternative Catalyst to TiO_2", *Journal of Photochemistry and Photobiology A: Chemistry*, Vol. 162, pp. 317-322, 2004.

35. Gu, F., S. F. Wang, M. K. Lü, G. J. Zhou, D. Xu and D. R. Yuan, "Structure Evaluation and Highly Enhanced Luminescence of Dy^{3+} Doped ZnO Nanocrystals by Li^{+} Doping via Combustion Method", *Langmuir*, Vol. 20, pp. 3528-3531, 2004.

36. Sato, Y., F. Oba, Y. Ikara, M. Yodogawa and T. Yamamoto, " Ggrain Boundary Dependency of Nonlinear Current-Voltage Characteristics in Pr and Co Doped ZnO Bicrystals", *Journal of Applied Physics*, Vol. 95, No. 3, pp.1258-1264, 2004.

37. Height, M., S. E. Pratsinis, O. Mekasuwandumrong and P. Praserthdam, “ Ag-ZnO Catalysts for UV-Photodegradation of Methylene Blue”, *Applied Catalysis B: Environmental*, Vol. 63, pp. 305-312, 2006.

38. Bhandari, S., J. Vardia, R. K. Malkani and S. C. Ameta, “ Effect of Transition Metal Ions on Photocatalytic Activity of ZnO in Bleaching of Some Dyes”, *Toxicological and Environmental Chemistry*, Vol. 88, pp. 35-44, 2006.

39. Anandan, S., A. Vinu, T. Mori, N. Gokulakrishnan, P. Srinivasu, V. Murugesan and K. Ariga, “ Photocatalytic Degradation of 2,4,6-trichlorophenol Using Lanthanum Doped ZnO in Aqueous Suspension”, *Catalysis Communications*, Vol. 8, pp. 1377-1382, 2007.

40. Sobana, N. and M. Swaminathan, “The Effect of Operational Parameters on the Photocatalytic Degradation of Acid Red 18 by ZnO”, *Separation and Purification Technology*, Vol. 56, pp. 101-107, 2007.

41. Ge, C., C. Xie, M. Hulin, Y. Gui, Z. Bai and D. Zeng, “Structural Characteristics and UV-light Enhanced Gas Sensitivity of La-doped ZnO Particles”, *Materials Science and Engineering B*, Vol. 141, pp. 43-48, 2007.

42. Che, P., J. Meng and L. Guo, “Oriented Growth and Luminescence of ZnO:Eu Films Prepared by Sol-Gel Process”, *Journal of Luminescence*, Vol. 122-123, pp. 168-171, 2007.

43. Chen, J., J. Wang, F. Zhang, G. A. Zhang, Z. G. Wu and P. X. Yan, “ The Effect of La Doping Concentration on the Properties of Zinc Oxide Films Prepared by Sol-Gel Method”, *Journal of Crystal Growth*, Vol. 310, pp. 2627-2632, 2008.

44. Ulah, R. and J. Dutta, “ Photocatalytic Degradation of Organic Dyes with Mangenese-Doped ZnO Nanoparticles”, Journal of Hazardous Materials, Vol. 156, pp. 194-200, 2008.

45. Chao, L., J. W. Huang and C. W. Chang, " Annealing Effects on the Properties of Nd Containing ZnO Nanoparticles Prepared by Sol-Gel Process", *Physic B*, Article in press.

46. Brown D., P. Laboureur, "Degradation of dyestuffs Part 2 Primary Biodegradation Under Anaerobic Conditions", *Chemosphere,* Vol. 12, pp. 394, 1983.

47. Kiriakidou, F., D. Kondarides and E. Verykios, "The Effect of Operational Parameters and TiO_2-Doping on the Photocatalytic Degradation of Azo-Dyes" *Catalysis Today*, Vol. 54, pp. 119-130, 1999.

48. Ozen, A. and V. Aviyente , "Experimental and Modeling Approach to Decolorization of Azo Dyes by Ultrasound: Degradation of the Hydrazone Tautomer", *Journal of Physical Chemistry A,* Vol. 109, pp. 3506-3516, 2005.

49. Joseph, J., H. Destaillat, H. Hung and M. R. Hoffmann "The Sonochemical Degradation of Azobenzene and Related Azo Dyes: Rate Enhancements via Fenton's Reactions", *Journal of Physical Chemistry. A*, Vol. 104, pp. 301-307, 2000.

50. Spadaro, J., L. Isabelle and V. Renganathan, "Hydroxyl Radical Mediated Degradation of Azo Dyes: Evidence for Benzene Generation" *Environmental Science Technology,* Vol. *28*, pp. 1389-1393, 1994.

51. Ioannis, K. and T. Albanis, "TiO_2-Assisted Photocatalytic Degradation of Azo Dyes in Aqueous Solution: Kinetic and Mechanistic Investigations", *Applied Catalysis B: Environmental,* Vol. 49, pp. 1–14, 2004.

52. Galindo, C., P. Jacques and A. Kalt, "Photodegradation of the Aminoazobenzene Acid Orange 52 by Three Advanced Oxidation Processes: UV/H_2O_2, UV/TiO_2 and VIS/TiO_2 Comparative Mechanistic and Kinetic Investigations", *Journal of Photochemistry and Photobiology A: Chemistry*, Vol.130, pp. 35–47, 2000.

53. Sayınsöz, E., "*Characterization and Photocatalytic Activity of Sepiolite- TiO_2 and Na Montmorillonite- TiO_2 catalyst*", M.S. Thesis, Boğaziçi University, 2006.

54. Yu, J., M. Zhou, H. Yu, Q. Zhang and Y. Yu, "Enhanced Photoinduced Super-Hydrophilicty of the Sol-Gel-Derived TiO_2 Thin Films by Fe-Doping", *Materials Chemistry and Physics*, Vol. 95, pp. 193-196, 2006.

55. Sreethawong, T., T. Puangpetch, S. Chavadej and S. Yoshikawa, "Quantifying Influence of Operational Parameters on the Photocatalytic H_2 Evolution Over Pt-Loaded Nanocrystalline Mesoporous TiO_2 Prepared by Single-Step Sol-Gel Process with Surfactant Template", *Journal of Power Sources*, Vol. 165, pp. 861-869, 2007.

56. Xu, A., Y. Gao and H. Liu, "The Preparation, Characterization and Their Photocatalytic Activities of Rare-Earth-Doped TiO_2 Nanoparticles", *Journal of Catalysis*, Vol. 207, pp. 151-157, 2002.